Evaluation of speed of sound aberration and correction for ultrasound guided radiation therapy

Evaluation of speed of sound aberration and correction for ultrasound guided radiation therapy

Davide Fontanarosa

Cover

Morgana, a mythological figure to whom a type of mirage is associated. Legend has it that a barbarian king invading Italy reached Reggio Calabria, on one side of the Strait of Messina. There he found a beautiful fairy (Morgana) who made the other side of the Strait appear so close that the king decided to swim across it to invade Sicily. He drowned and missed the target. In the same way, speed of sound aberration can make internal anatomical structures look much closer (or farther) than they are. This way, as the fooled king, radiotherapy treatment can miss its target.

Production

Printing: Datawyse | Universitaire Pers Maastricht

ISBN 978 94 6159 321 4

Evaluation of speed of sound aberration and correction for ultrasound guided radiation therapy

Proefschrift

ter verkrijging van de graad van doctor aan de Universiteit Maastricht,
op gezag van de Rector Magnificus Prof. Dr. L.L.G. Soete,
volgens het besluit van het College van Decanen,
in het openbaar te verdedigen
op woensdag 26 maart 2014 om 10.00 uur

door

Davide Fontanarosa

UNIVERSITAIRE PERS MAASTRICHT

Promotor

Prof. ir. F. Verhaegen

Beoordelingscommissie

Prof. dr. P. Lambin, voorzitter
Prof. dr. J. Bamber
Dr. W. Backes
Prof. dr. K. Nicolay
Prof. dr. H. Wijkstra

Contents

Introduction

Chapter 1

Introduction and outline of the thesis

1.1 Radiotherapy treatment

Cancer is becoming the first cause of mortality in western countries. It is a very complex disease, typically requiring local control and systemic treatment. Surgeons can remove the visible, palpable or detectable tumoral tissues. But only when it is in a body area which is somehow reachable. Chemotherapy provides the systemic coverage. Radiotherapy (RT) can target tissues which cannot be reached by the surgeon and can sterilize areas where tumor is not visible but possibly present. And it is, most of the time, not invasive. Instead of a scalpel, high energy beams of ionizing radiation of photons, electrons or ions, are used. The three modalities combine in modern oncology to provide the best treatment option for cancer. The aim of RT is therefore to deliver a precisely controlled radiation dose to the target, while sparing the normal tissue and possible nearby organs at risk.

1.2 Patient positioning

A treatment plan is usually prepared based on a computerized tomography (CT) scan taken one or two weeks before the start of the treatment course. A dose distribution is calculated which should optimally achieve cancer destruction and healthy tissues sparing. It is typically delivered in multiple fractions, to allow healthy tissues to recover. This dose must be delivered by maintaining with high accuracy the conditions in which the plan was calculated, corresponding to the initial CT scan. For modern highly conformal plans, an error above 2-3 mm can produce important negative consequences. Correct positioning of the patient prior to each treatment fraction is therefore of the utmost importance. Different strategies include: lasers, masks, body positioning devices, etc. The most traditional techniques use external reference points on the patient, such as tattoos or markers on the skin. If positioning devices are used, the reference marks are on the device. Other systems (films, electronic portal imaging – EPID, fluoroscopy, etc.) allow re-positioning of the patient based on internal structures. Presently, only fluoroscopy allows tracking of structures during treatment. All these systems need X-ray based imaging, with consequent extra unwanted dose to the patient. A magnetic resonance (MR) – LINAC combined system is under development which should perform tracking without irradiation. The device needs intense magnetic fields, though, which limit its use to patients without magnetic sensitive implanted devices. Recently, cone beam CT (CBCT) has increasingly become more available to RT departments and it is now generally considered the reference system for image guided RT (IGRT).

1.3 Ultrasound imaging

Ultrasound (US) imaging is an established diagnostic tool in radiology. Its introduction for RT applications is relatively recent. US has some peculiar characteristics which differentiate it from the other imaging modalities used for IGRT. US imaging can have much higher resolution, which can be in principle decided by the final user. It does not deliver any extra dose to the patient, therefore it can be repeated multiple times if necessary. US has excellent contrast for soft tissues, allowing identification of tissues invisible to CT or CBCT. US present a flaw, though: aberrations. In RT, aberrations which deteriorate the quantitative reliability of the imaging system can be a major cause of under- or over-dosage of the patient. Some of these aberrations can be recognized and corrected. Speed of sound (SOS) aberration is not among these and must be addressed specifically. Throughout this work, the term “aberration” is used to indicate an error in image creation due to the difference between the SOS values in tissues and the (fixed) value assumed by US systems, at 1540 m/s. The term “aberration” has a different meaning outside of this field of research, in acoustics and ultrasound literature, where it refers typically to wave aberration.

1.4 US guided RT

Clinically, US has been used in RT for treatment guidance (USgRT) comparing a scan of the patient before each treatment fraction with a reference image dataset, typically the CT scan used for planning (CTsim) or a co-registered US scan taken at the same time of CTsim. Particular care is taken that all the datasets have the exact same coordinate system, therefore a direct position comparison can be performed. With these systems, internal soft tissue structures are used to setup the patient, as opposed to, e.g., CBCT where mainly bony anatomy or metal implanted markers are used. This means that the treatment target is positioned, and that the procedure is virtually insensitive to changes in the internal distribution of the tissues. Recently, a 4D US tracking system (AutoScan by Clarity) was introduced, which allows real time monitoring of target position (only prostate, at the time this thesis is written). It is the first time that a real time 3D imaging system is used for this purpose, previously only fluoroscopic 2D projections were used, for example real time RT (RTRT) and CyberKnife.

1.5 Objectives and outline of the thesis

The main objectives of this thesis were:

i) To study the impact of SOS aberration on US-aided positioning in RT.
ii) To compare the errors due to the aberration with the discrepancies reported in literature for clinical quantitative use of US.
iii) To introduce a general correction algorithm for this type of applications in RT.
iv) To assess the robustness of the algorithm with respect to the possible treatment workflows and changes occurred in the patient during the treatment.
v) To introduce a fully automated cross-modality segmentation algorithm on CT and US, as an application specific to RT of US imaging, only possible after quantitative reliability of US is restored.

In this **Chapter 1**, a general introduction is given on the background and importance of US applications in RT. A more detailed description of US technology is presented in **Chapter 2**. This is part of an invited review for the journal *Physics in Medicine and Biology*. The aim is to make the reader more familiar with the concepts used in the rest of the thesis and to provide a convenient framing in the field of RT. With **Chapter 3**, the first part with original research of the thesis begins, named "Physical density to drive speed of sound aberration correction". In this part the SOS aberration correction based on the physical density provided by the co-registered CT scan is presented. In the first chapter, the idea based on the observation that in RT a CT scan is always available, which can be used as source for physical density is introduced. The algorithm created for the correction is described in detail. Validation on phantoms was performed and a first simplified application on a prostate and a breast case are shown. In **Chapter 4** a systematic study of the SOS aberration correction effect on different clinical scenarios is reported. Five prostate, five breast and five liver cancer cases were examined. On each of them, the correction was applied and the magnitudes of the shifts produced by the algorithm were considered indications of the impact of the aberration. The results show that for liver the aberration is unpredictable for the effects on both structures' depth and shape. So, in our dataset, a correction was always necessary, since errors up to more than 7 mm in positions of the regions of interest (ROI) were measured. Also for the prostates, an average error of about 3 mm in the position of the centers of mass was sufficient to suggest a correction for SOS aberration. The magnitude and direction of these shifts were in good agreement with the discrepancies reported in literature, which made us hypothesize that SOS aberration might be an explanation for a large fraction of them. For breasts, small shifts were measured, typically around 1 mm. We did not exclude that the limited dataset with possibly small breasts might have biased these results. But from our experience, it does not seem that for these organs a correction is strictly required. In **Chapter 5** the sensitivity of the procedure to workflow and changes in the patients was examined. All the possible combinations of the clinical workflows and changes that can occur in the patient or to the scanning protocol were addressed. We extensively tested the robustness with extreme parameter variations in phantoms, even slightly outside clinical

conditions. At the end, it was possible to claim that if no major changes happen, where by major we mean changes that would require re-planning of the treatment, the algorithm produces correct results. In particular, it produces better results than each of the other workflows considered, and always with discrepancies below the clinically detectable threshold. Once the algorithm was validated on phantoms, tested on patients and proven robust, we extended in **Chapter 6** its range of application. From the initial parallelepipedal volumes produced by linear probes, we re-coded it to a more general case of a generic 3D US volume produced by a curvilinear probe, which includes the previous shape but allows also any volume with non-parallel paired sides. The new algorithm was validated on a pelvic phantom. Then it was applied to 15 prostate cancer patients. The results confirmed the conclusions of Chapter 4, showing the same direction and average magnitude for the SOS aberration. With **Chapter 7** the second part with original research of the thesis begins, entitled "Quantitative ultrasound imaging applied to segmentation". This Chapter is based on the observation that, as reported in literature, CT and US visualize the tissues differently. In particular, to some extent they provide complementary information, because US can image soft tissues with high contrast and resolution, typically on limited spatial volumes. CT instead produces larger images with well-defined bony structures, invisible to US. The segmentation algorithm presented makes for the first time a simultaneous use of the information from both modalities; for the first time it is natively in 3D space, and again for the first time it is completely automatic. It is intelligent, meaning that it can be trained on a specific dataset representing the characteristics of a patients' population. We asked an experienced physician to contour the prostates on the fusion of 16 co-registered CT and US scans. The algorithm was able to reproduce independently the contours to an excellent degree. In **Chapter 8** the work experience of these PhD years is summarized from a personal perspective. In particular, the key results are re-interpreted in view of what the future developments might be.

Chapter 2

Review of Ultrasound in External Beam Radiotherapy

Davide Fontanarosa
Skadi van der Meer
Jeffrey Bamber
Tuathan O'Shea
Emma Harris
Frank Verhaegen

This review is part of a more extensive invited review in two parts for Physics in Medicine and Biology

2.1 Introduction

Need

Radiotherapy (RT) treatments aim at destroying tumor tissues while at the same time sparing as much as possible healthy tissues. To this end, a therapy plan must be prepared, based on the information on patient anatomy and physical density provided by a simulation (SIM) image scan. Typically this is a computerized tomography (CT), although recently other imaging modalities are being considered [1]. At the planning stage, the regions of interest (ROI) of the patient are contoured. This way, the target (or targets) and the organs at risk (OAR) are properly identified. This step requires as much information as possible about the tissues' nature or status of the involved ROIs, in order to outline and differentiate correctly the tumor from the OARs. Different imaging modalities are becoming increasingly necessary to integrate complementary anatomical, biological and functional information. In particular for soft tissues, which are visualized with a rather poor contrast in CT scans. Once the contours are identified, they are usually expanded with a margin to take into account all the uncertainties which might be involved in the RT process [2]: setup errors, organ motion, and organ volume and shape changes. These margins should also be selected to minimize the dose to surrounding OARs [3]. The dose distribution to be delivered to the patient is then calculated, usually with the help of a treatment planning system (TPS). This dose is finally delivered to the patient at the treatment stage (TX) in a certain number of fractions (FX). At TX, it is paramount to reposition the patient as accurately as possible in the same position as at SIM, reproducing the conditions in which the plan was prepared. Reducing patient positioning errors allows to decrease margins around structures and consequently to keep radiation toxicity in OARs low. To this end, imaging systems must be used which guarantee quantitative reliability in recognizing the exact position, volume and shape of structures. Among these, film or electronic portal imaging [4] [5] are well established techniques. At TX, bony structures are recognized and, if not aligned with the position at SIM, a correction is applied to the patient's position. But this correction strategy is not very effective when targets are made of or are surrounded only by soft tissues, e.g. the prostate, which may move with respect to the bones. The image contrast levels provided might not be sufficient to align tissue structures with the radiation beams. Other positioning techniques have thus been introduced such as, for example, markers implanted in tissue, cone beam CT (CBCT), global positioning system (GPS) for the body localization and ultrasound (US) imaging.

Advantages and disadvantages of Ultrasound

US imaging has been widely used for diagnosis of cancer [6]. It is relatively inexpensive and easy to use, and it has a diagnostic value comparable to MRI or CT. With US, contouring accuracy of soft tissue structures improves [7-9] as it can provide comple-

mentary information to other imaging systems [10]. At TX, patient setup can be performed based not only on bony structures (as e.g. with Mega Voltage (MV) CBCT) or implanted fiducial markers, but on the real shape and position of the internal organs. Moreover, monitoring interfraction organ motion is a prerequisite for adaptive applications [11,12]. US imaging does not add extra unwanted radiation dose to the patient, similar to MR imaging. In fact, US imaging does not rely on an external source of radiation, but rather it stimulates the material to scan with mechanical waves. Then reflections (and scattered signal) generated during the wave propagation are read by the system. It is therefore the material itself that, by responding to this stimulus, provides the examiner with information about its structure, composition, nature etc. A large amount of information is in principle available, typically not yet used in clinical practice. Therefore, there is much room for future improvements. US is generally a non-invasive imaging modality but, due to the physical incapability of US wave propagation through bones and air, some body regions cannot be imaged. With external and intracavitary US probes a wide range of body regions can be imaged: pelvis, abdomen, breast, neck etc. [13].

US is inherently a real time imaging technology as images are reconstructed and visualized immediately during the scan. Recently, real time US imaging in three dimensions (3D) became possible [14,15]. With continuous scanning over time with the harmless US waves, 4D monitoring of tissues during RT treatment is possible. This opens new scenarios where real time automated segmentation and motion compensation during treatment can enable adaptive correction of treatment.

Until recently, US was prevalently used in Radiology, as a qualitative diagnostic tool (except for some applications as fetal measurements in Obstetrics [16]). This application relies heavily on the user ability to visualize the internal structures. As a consequence, US imaging was considered a user dependent imaging modality, and inter-observer variability was shown [17,18]. US was also seen as responsible for important tissues displacement [19]. Moreover, traditionally US scanning requires specific skills and training, which are typically not part of the education of the average radiation oncologist, technologist or clinical physicist. Specific scan protocols aimed at minimizing user dependence and excessive pressure on the skin were introduced. Together with technological advances (new probes, thick coupling gels, optimal scan directions calculated by computers etc.), they made US quantitatively comparable to other positioning systems in RT [20]. A comprehensive comparative table between different imaging systems for treatment guidance (image guided RT (IGRT) [21]) is presented in [22]. In Table 1 is shown a comparison between advantages and disadvantages of CT and US imaging systems.

	Imaging method			
	CT		US	
	Advantages	Disadvantages	Advantages	Disadvantages
Acquisition time (including setup/preparation)	~2 min			3-4 min
Visualization capabilities	kVCT: soft tissue in the whole body. Whole body imaging	MVCT: bone contrast only	Soft tissues; high contrast	Difficult to image through air or bones (no lungs/head). Limited section imaging
Invasiveness	NO	YES with markers or contrast	NO	YES for special application (intracavitary) or with contrast
Dose delivered		1-3 cGy (kV); 1-15 cGy (MV)	None	
Attenuation information	YES			NO
Operator dependence	NO			YES
Intrafraction monitoring	Offline for MV (Tomotherapy)	NO	YES	
Image distortion	NO	CBCT: scatter distortion		YES (probe pressure)
Imaging artifacts		Streaking, beam hardening		Aberrations
Functional/biological information	YES		YES (elastography, tissue typing, contrast,...)	
Motion tracking	YES (4D-CBCT online not real time)	Poor soft tissue contrast, needs implanted markers	YES	
Scan setup/preparation	NO	Contrast CT requires setup		YES
ART	YES		YES	
Dose calculation	YES			NO

Table 1: Advantages and disadvantages of CT and US imaging systems. For both methods, if a feature can be considered advantageous is listed in the Advantages column. Otherwise in the Disadvantages column. For CT, two cases are distinguished: when the beam is in the kV range (standard CT and kV cone beam CT (kVCBCT)) and when it is in the MV range (MVCBCT and Tomotherapy). ART refers to Adaptive RT [23], while DGRT refers to Dose Guided RT [24].

US in the Radiation treatment work-flow

Initially, only two-dimensional (2D) US systems were used, which allow the visualization of two perpendicular scans of the target. These first applications were focused only on prostate cancer treatment and showed many limitations [18,25,26]. Then 3D systems started to gather consensus, because they can provide a real 3D volume of the target in absolute coordinates. This allows an easier and more accurate setup of the patient. Other sites were investigated, besides prostate: breast, liver, neck and cervix/uterus. The major sources of errors were studied and solutions were proposed. The current status of the art comprises four-dimensional (4D) real time tracking of targets (at the time of writing, only for prostate). In the RT workflow US in its current implementations gives input in two phases. During contour outlining, its superior soft tissue contrast capabilities allow a better delineation of target and OARs. During setup of the patient, US guidance (USgRT) helps identifying the position of the target and of the OARs. The new position of the target can be used to recalculate dose and, if necessary, re-plan the patient, in adaptive applications. Other applications can be envisioned using advanced US imaging modalities. At treatment planning, functional (elastography, contrast enhanced US (CEUS)) and molecular CEUS information (part II Section 3) might help treatment design, although they are not yet part of the standard clinical practice. These imaging modalities can also be used to assess tumour or normal tissue response after treatment [27-29]. It must be noted that, differently from FDG-based positron emission tomography (PET), this assessment can be operated immediately, as inflammatory effects do not affect US visualization capabilities. A summary of the steps in the RT workflow which can benefit from US is plotted in Fig. 1.

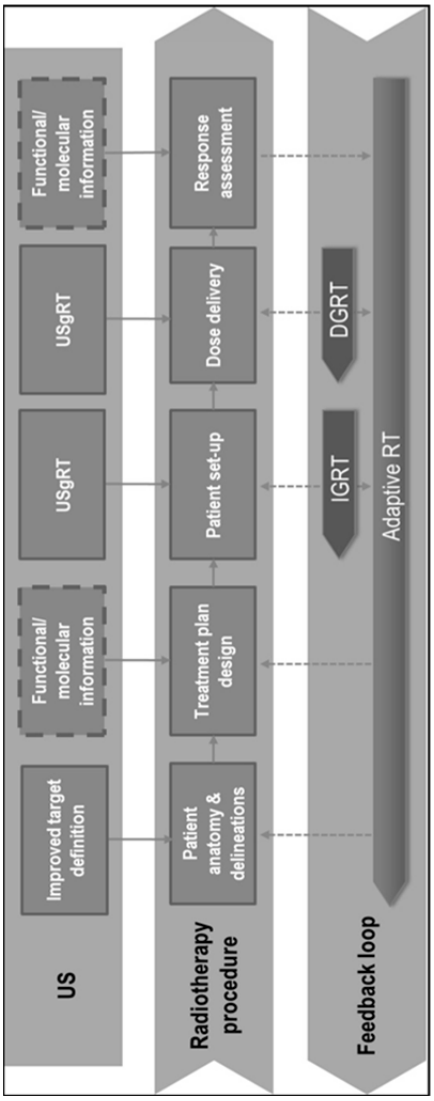

Fig 1: US in the RT workflow. In the first row is reported the type of input which can be provided by US. Contoured with dashed lines are the applications not yet clinically available. In the second row, the steps involved in the RT treatment. The arrow indicates the temporal direction. In the third row are shown the feedback loops which can be generated by the US images.

2.2 Technologies

Many references are available in literature about US physics theory and technology. Among these, [29-35] offer an overview at different technical levels of complexity.

Transducers

A transducer is essentially a dielectric element which converts electrical signals into acoustic waves and vice-versa. Transducers are formed by one or more piezoelectric crystals. Natural piezoelectric materials are for example quartz, tourmaline and Rochelle salt. But also man-made ceramic materials show the same properties. The most common are: lead zirconate titanate (PZT), barium titanate, lead metaniobate and polyvinylidene difluoride (PVF_2) [37]. These ceramics become piezoelectric when heated in a strong electrical field; they are less expensive, more durable and more efficient. In combination with particular polymers they can also offer lower impedance (reducing the mismatch with tissues) and improved bandwidth, sensitivity and resolution [38].

The operating frequency is typically the "resonant" or "natural" frequency, which is inversely related to its thickness, and directly to the propagation speed.
In particular:

$$d_{cry} = \frac{1}{2}\lambda_{res} \tag{2.1}$$

where d_{cry} is the thickness of the crystal and λ_{res} is the wavelength of the US wave at resonance.

For the propagation speed instead:

$$c_{cry}\left[\frac{mm}{\mu s}\right] = 2d_{cry}[mm] \cdot f[MHz] \tag{2.2}$$

where c_{cry} is the speed of sound inside the crystal.

A transducer is normally formed by one or more piezoelectric crystals, the active elements of the system. These elements can be positioned in linear, curved or annular arrays. Together with the damping material, the matching layer, wiring and an insulating case form the probe (which is also commonly referred to as the transducer) (Fig. 2a). The elements can be activated in different ways: subsets of the array can be fired simultaneously to create an acoustic aperture (line of view); then multiple sequential apertures create the field of view. Or the elements are activated at different times to steer the beam (phased mode).

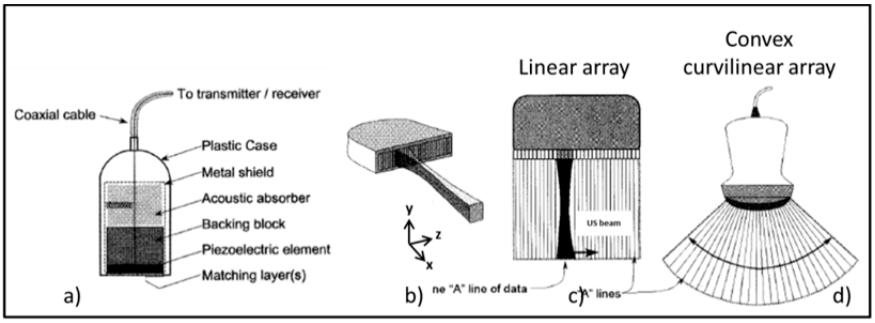

Fig. 2. a): A single element US probe with its components. **b)** A linear array transducer with plotted a line of view and the three directions corresponding to axial (X), elevational (Y) and lateral (Z) US dimensions. **c)** The field of view of a linear probe; a single line of view (A-mode) is highlighted and the scanning direction is indicated by an arrow. **d)** A curvilinear probe with the field of view separated in its lines of view. (Images courtesy of: [33])

The damping material (typically epoxy resin impregnated with tungsten) is bonded to the back of the active elements to limit ringing in the crystal and to absorb energy emitted backwards. Its rear surface is slanted to prevent reflection back into the crystal. The matching layer reduces the difference in Z value between the crystal and the surface of the scanned tissue (as the skin), allowing a better transmission. Its thickness d_{ML} is usually:

$$d_{ML} = \frac{1}{4}\lambda_{res} \tag{2.3}$$

where λ_{res} is the resonating frequency of the crystal.
An indication of the type of applications fitted for a specific probe is its quality factor QF:

$$QF = \frac{f_{res}}{bandwidth} \tag{2.4}$$

If the QF is high, the bandwidth is narrow and the crystal rings for a long time (continuous wave (CW) transducer). Some applications benefit from this operating modality, like CW Doppler. If the QF is low, the transducer is working in pulsed wave mode (PW) and a good axial resolution can be achieved.

Transducers are designed in such a way that each wavelet produced by every point on the surface of the emitting crystal combines with the others, according to Huygens' principle. The wave interference results in an hourglass-shaped sound beam in the forward direction where most of the energy is transmitted along the central axis. The beam has three distinct zones: the one closest to the transducer is the Fresnel zone. As an example, for a transducer shaped as a simple piston, in the Fresnel zone the beam has initially the dimensions of the crystal, and then it converges to approximately half of its diameter. This is the focal zone, with at the center the focal spot. Then the beam

starts diverging in the Fraunhofer zone, with the divergence being inversely proportional to crystal diameter.

The image resolution has three aspects: temporal, contrast and spatial. The temporal resolution depends on the equipment's frame rate. The contrast depends on how well the US device can distinguish between echoes of slightly different intensities. The spatial resolution can be further divided into three types: longitudinal (or axial) which is the ability to distinguish objects spatially close along the direction of propagation of the beam; elevational, in the direction perpendicular to the scan plane; and lateral, along the direction of the beam propagation plane (X, Y and Z directions respectively in Fig. 2b). If the distance between two subsequent interfaces is larger than half the pulse length, the reflection from the first overlaps with the reflection from the second.

Image formation

In general, above the human hearing range (i.e. above approximately 20 kHz) sound pressure waves can be defined as US. In US imaging, though, the frequencies used are typically (2 - 8)MHz. Modern US transducers for medical applications work in pulse-echo mode: the transducer both emits and receives the US waves. A very brief US pulse is emitted inside the material or tissue to be scanned and then the device switches to listening mode. If in the scanned volume there is a change in the physical properties of the material or tissues (for example density or elasticity), then the acoustic impedance changes. Acoustic impedance is defined as:

$$Z = \rho c \tag{2.1}$$

where ρ is the physical density and c is the speed of sound (SOS). Whenever the ultrasound burst traverses an interface between materials or tissues with different Z, part of the pulse is reflected back. The reflections travelling back towards the transducer are recorded as echoes and used to create the US image. If a single line of view is visualized, the device is working in amplitude mode (A-mode). Echo times (also called times of flight (TOF)) and amplitudes are recorded. Then the TOFs are transformed to depths assuming a fixed value for the SOS (typically 1540 m/s [39]). Finally the echo amplitudes are plotted on a screen as function of depth. If multiple lines of view in a plane are sequentially recorded, by an array of transducers, the plane scanned can be viewed as a 2D image on a screen. This is the brightness mode (B-mode), generally considered the standard 2D US modality. When a quick series of pulses are emitted and echo amplitudes along one line of sight as a function of time are displayed, the device is working in motion mode (M-mode). The movement of structures can thus be followed, e.g. a heart valve, which is the typical application of this modality.

The US probe can be swept through a volume, thereby creating multiple 2D images of different planes. If these planes can be localized in space, for example using a position and direction detection system attached to the probe, a 3D US volume can be reconstructed and visualized. In RT, typically a 3D US scan is performed before the treatment and compared to either the SIM CT scan or another SIM 3D US scan. This allows a direct comparison of the anatomy, as described in the Introduction.

In RT we require quantitative measurements of position, volume and shape or structures. Therefore minimize or compensate image aberrations is of extreme importance. Different causes can generate aberrations. They can be related to the US device used, the operator scan technique or can be due to US physics. Most of the time, they are noticeable, have a transient appearance, or produce obvious distortions or unexpected/periodic symmetries. In these cases, correction strategies can be applied. But sometimes they can be very difficult to detect, because the effect produced has none of the characteristics previously described. For example, SOS aberration produces errors in distance measurements which are difficult to recognize unless some reference alternative measurement is available.

1. Refraction

Every time the US beam traverses an interface between tissues, it is subject to Snell's laws of refraction:

$$\frac{\sin \vartheta_1}{\sin \vartheta_2} = \frac{c_1}{c_2} \tag{2.6}$$

where θ_1 and θ_2 are the angles with the surface normal before and after the interface, and c_1 and c_2 are the SOS values of the two tissues. Thus, if the beam is not perpendicular to the interface, the propagation is along a different direction after the interface. If the beam encounters a structure after the refraction, the US device will assume it was in the original direction and therefore misplace it in the image.

2. Reverberation

When an US beam traverses an interface between tissues with different acoustic impedances, part of it is reflected and part is transmitted; for a perpendicular incidence, the ratio between the reflected pressure and the incident pressure, for normal incidence, is:

$$R = \frac{Z_2 - Z_1}{Z_2 + Z_1} \tag{2.7}$$

where Z_1 and Z_2 are the acoustic impedance values of the proximal and distal tissues.
If multiple close reflecting surfaces are present along the beam, the US beam can be reflected back and forth between them generating multiple equally spaced fake boundaries in the image.

3. Mirror imaging

When a strong reflective surface is in the beam path, it can produce false distal mirror images of the object.

4. Shadowing and enhancement

If a high attenuation object is present along the beam, it can induce low-intensity streaks in the image beyond the object, along the lines of view intersecting it. The opposite effect occurs when a low echogenic material is traversed: the attenuation is much lower than in the surrounding tissues, resulting in hyperintense streaks distal to those structures.

5. Probe pressure displacements

To visualize internal structures, often the operator needs to sweep the US probe on the patient's skin. In particular for radiological applications, no strict scanning protocols are required. It is rather the operator who decides on the probe position, the scanning angle and the scanned volume. In these cases, it might happen that the pressure produced by the probe on the skin displaces underlying tissues and consequently also the scanned structures themselves. For quantitative applications, especially when absolute localization of the scanned volumes is required, this may result in a serious misplacement of the target and a subsequent incorrect irradiation.

6. Side and grating lobes

Piezoelectric elements, when the voltage pulse is applied, expand in all directions, although the main excursion is along the longer axis. The minor expansion in the orthogonal directions produces side lobes: if structures are present along these directions, they are recorded in the image as if they were along the main beam. If the piezoelectric elements are organized in an array transducer, this effect can produce grating lobe artifacts.

7. Speed of sound aberration and correction

SOS in clinical US applications is a property of tissues, not of the wave. If high degrees of precision in its measurement are necessary, its dependence on the frequency, its nonlinear behavior and other higher level dependencies must be taken into account. But for biological tissues, the precision of clinical methods is rarely good enough to observe, e.g., velocity dispersion. SOS depends on physical density and on compressibility of the traversed medium. In human soft tissues, SOS values range from 1450 m/s (fat) to 1700 m/s (tendons) [35,40]. This variability depends on density and compressibility ranges in the tissues. The practical assumption made by US devices of a constant value is the reason for SOS aberrations. In fact, since SOS maps of the scanned tissues are not available prior to the scans, the US device assumes the SOS in the traversed tissues is at an average value usually set at 1540 m/s. If the real SOS values are signifi-

cantly different from the assumed one, the calculated distances will be incorrect. As an example, if the traversed tissue is fat and the imaged structure is at a depth of 12 cm, the US device will instead report its depth at:

$$D = \frac{1540}{1450} \cdot 12.0cm = 12.74cm \tag{2.8}$$

This introduces an error in the position measurement of 7.4 mm which, in quantitative imaging for RT applications, is often relevant. Such a discrepancy between the position from the US scan and the position as reported by the SIM CT scan usually is above the action level threshold at TX. So it would induce an unnecessary corrective shift in the opposite direction of the patient, likely resulting in target underdosage and/or OAR overdosage. This problem is explicitly reported in the literature (e.g. [41]) but there is strong indication [42-44] that reported discrepancies between US and other imaging modalities [45-48] can at least partially be explained due to this aberration. Some partial solutions were proposed [26,49,50]. Unfortunately, it is difficult to extract information useful for this correction from the US scans alone. Multiple entrance portals (as in US tomography [51]) might allow for correction strategies as the ones applied for refraction [52]. These technologies, though, are rarely clinically available. And most of the US devices work in pulse-echo mode, and not in transmission (although some attempts were made in this direction [49,53,54]).

Recently, a correction strategy in the RT workflow, based on the physical density provided by co-registered CT scans, was presented [42]. Using a previously published relation between density and SOS values in human soft tissues [40] the density maps can be transformed in SOS maps. Then the latter can be used to correct along each line of view the US scans. The algorithm was applied to clinical cases of breast, liver and prostate cancer patients. It was shown that in some situations the SOS aberration can produce rather important corrections requiring shifts of more than 7 mm [43,44,55].

3DUS imaging

Conventional 2DUS images are scanned at arbitrary angles through the body. Multiple images are then combined by the operator to form a mental image of the 3D anatomy. This process depends heavily on the operator's skills and experience, and is inherently qualitative. For quantitative applications, such as estimation of organ shapes or volumes, this is far from optimal [56,57]. For these applications the limitations of 2DUS can be overcome with 3DUS [58]. From the first attempts in diagnostic imaging [59-61] many technological advances led to the development of the modern 3DUS systems, which nowadays some manufacturers offer. Currently, two major approaches are followed: mechanical scanning and free-hand scanning with position sensing.

In the first category are those devices where a motorized mechanism inside the probe case translates, tilts or rotates a conventional 2D transducer, while an acquisition system records the images. Then these images are used to reconstruct 3D vol-

umes using the information on their relative positions provided by the mechanical encoder. The sampling angle can usually be adjusted in order to balance image quality with scanning time [62]. In the second, tracking sensors are mounted on conventional 2D US scanners which allow the measurement of the transducer's position and orientation while it is scanning the volume. This information is then coupled with the images to reconstruct a 3D volume [63]. As tracking systems, robotic arms [64], acoustic sensors [65], optic sensors [66], magnetic fields and speckle decorrelation [67,68] are currently the most used [57].

Visualizing the acquired volumes is a key point in these techniques as effects like shadowing and speckle are present in US images and might make their interpretation difficult. The most frequently used visualization techniques are multi-planar reformatting (MPR) and surface rendering. In MPR, it is possible to browse through the volumes selecting e.g. a couple of intersecting cross planes [69] (Fig. 3a). Surface rendering is based on ray-casting techniques. It is used when a high contrast is present between different tissues, allowing surface reconstruction of e.g. fetal images [70] (Fig. 3b) or cardiac images [71]. Also volumetric rendering (VR) was introduced using techniques such as Maximum Intensity Projection [72].

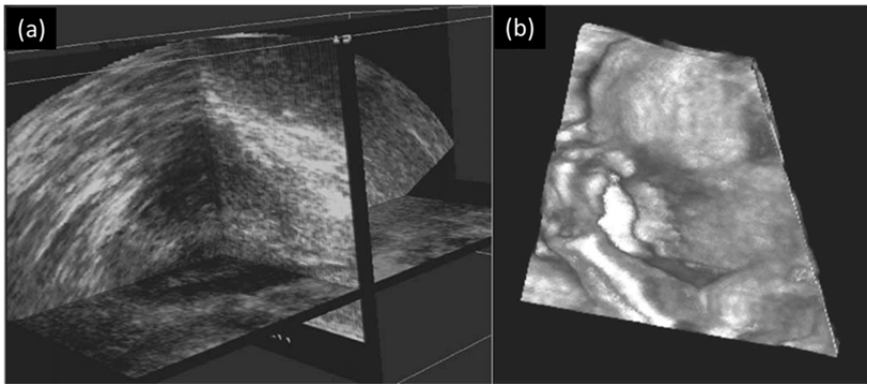

Fig. 3. a) Example of MPR view of a prostate, showing intersecting extracted planes. **b)** Example of 3DUS VR of the face of a fetus. (Images courtesy of: [71])

References

1. Jonsson JH, Karlsson MG, Karlsson M Nyholm T. Treatment planning using MRI data: an analysis of the dose calculation accuracy for different treatment regions. Radiat Oncol 2010;5:62.
2. Urie MM, Goitein M, Doppke K, et al. The role of uncertainty analysis in treatment planning. Int J Radiat Oncol Biol Phys 1991;21:91-107.
3. Schwarz M, Giske K, Stoll A, et al. IGRT versus non-IGRT for postoperative head-and-neck IMRT patients: dosimetric consequences arising from a PTV margin reduction. Radiat Oncol 2012;7:133.
4. Bel A, Vos PH, Rodrigus PT, et al. High-precision prostate cancer irradiation by clinical application of an offline patient setup verification procedure, using portal imaging. Int J Radiat Oncol Biol Phys 1996;35:321-332.
5. Schewe JE, Balter JM, Lam KL ten Haken RK. Measurement of patient setup errors using port films and a computer-aided graphical alignment tool. Med Dosim 1996;21:97-104.
6. Rose RJ S.Allwin. Computerized Cancer Detection and Classification Using Ultrasound Images: A Survey. International Journal of Engineering Research and Development 2013;5:36-47.
7. Huang YL Chen DR. Automatic contouring for breast tumors in 2-d sonography. Conf Proc IEEE Eng Med Biol Soc 2005;3:3225-3228.
8. Huang YL, Jiang YR, Chen DR Moon WK. Level set contouring for breast tumor in sonography. J Digit Imaging 2007;20:238-247.
9. Molloy JA, Srivastava S Schneider BF. A method to compare supra-pubic ultrasound and CT images of the prostate: technique and early clinical results. Med Phys 2004;31:433-442.
10. Smith WL, Lewis C, Bauman G, et al. Prostate volume contouring: a 3D analysis of segmentation using 3DTRUS, CT, and MR. Int J Radiat Oncol Biol Phys 2007;67:1238-1247.
11. Harris EJ, Donovan EM, Coles CE, et al. How does imaging frequency and soft tissue motion affect the PTV margin size in partial breast and boost radiotherapy? Radiother Oncol 2012;103:166-171.
12. Juan-Senabre XJ, Lopez-Tarjuelo J, Conde-Moreno A, et al. Uncertainties and CTV to PTV margins quantitative assessment using cone-beam CT technique in clinical application for prostate, and head and neck irradiation tumours. Clin Transl Oncol 2011;13:819-825.
13. Block B. Color Atlas of Ultrasound Anatomy, ed. 2nd. Stuttgart, Germany: Thieme, 2012.
14. Dietz HP. Ultrasound imaging of the pelvic floor. Part II: three-dimensional or volume imaging. Ultrasound Obstet Gynecol 2004;23:615-625.
15. Majida M, Braekken IH, Umek W, Bo K, Saltyte Benth J Ellstrom Engh M. Interobserver repeatability of three- and four-dimensional transperineal ultrasound assessment of pelvic floor muscle anatomy and function. Ultrasound Obstet Gynecol 2009;33:567-573.
16. Issel EP, Prenzlau P, Bayer H, et al. The measurement of fetal growth during pregnancy by ultra-sound (B-scan). J Perinat Med 1975;3:269-275.
17. Enke C, Ayyangar K, Saw CB, Zhen W, Thompson RB Raman NV. Inter-observer variation in prostate localization utilizing BAT. International journal of radiation oncology, biology, physics 2002;54:269.
18. Langen KM, Pouliot J, Anezinos C, et al. Evaluation of ultrasound-based prostate localization for image-guided radiotherapy. Int J Radiat Oncol Biol Phys 2003;57:635-644.
19. Artignan X, Smitsmans MH, Lebesque JV, Jaffray DA, van Her M Bartelink H. Online ultrasound image guidance for radiotherapy of prostate cancer: impact of image acquisition on prostate displacement. Int J Radiat Oncol Biol Phys 2004;59:595-601.
20. van der Meer S, Bloemen-van Gurp E, Hermans J, et al. Critical assessment of intramodality 3D ultrasound imaging for prostate IGRT compared to fiducial markers. Med Phys 2013;40:071707.
21. Xing L, Thorndyke B, Schreibmann E, et al. Overview of image-guided radiation therapy. Med Dosim 2006;31:91-112.
22. Evans PM. Anatomical imaging for radiotherapy. Phys Med Biol 2008;53:R151-R191.
23. Yan D, Ziaja E, Jaffray D, et al. The use of adaptive radiation therapy to reduce setup error: a prospective clinical study. Int J Radiat Oncol Biol Phys 1998;41:715-720.

24. Chen J, Morin O, Aubin M, Bucci MK, Chuang CF Pouliot J. Dose-guided radiation therapy with megavoltage cone-beam CT. Br J Radiol 2006;79 Spec No 1:S87-98.
25. Lattanzi J, McNeeley S, Pinover W, et al. A comparison of daily CT localization to a daily ultrasound-based system in prostate cancer. International journal of radiation oncology, biology, physics 1999;43:719-725.
26. Van den Heuvel F, Powell T, Seppi E, et al. Independent verification of ultrasound based image-guided radiation treatment, using electronic portal imaging and implanted gold markers. Med Phys 2003;30:2878-2887.
27. Vlad RM, Kolios MC Czarnota GJ. Ultrasound imaging of apoptosis: spectroscopic detection of DNA-damage effects at high and low frequencies. Methods Mol Biol 2011;682:165-187.
28. Vlad RM, Brand S, Giles A, Kolios MC Czarnota GJ. Quantitative ultrasound characterization of responses to radiotherapy in cancer mouse models. Clin Cancer Res 2009;15:2067-2075.
29. Sadeghi-Naini A, Falou O, Tadayyon H, et al. Conventional frequency ultrasonic biomarkers of cancer treatment response in vivo. Transl Oncol 2013;6:234-243.
30. Hill CR Dunn F. Physical Principles of Medical Ultrasound edited by C. R. Hill. The Journal of the Acoustical Society of America 1987;82:721.
31. Carson PL. Biomedical ultrasonics. By P.N.T. Wells, Ph.D., Academic Press, Inc. London, Copyright 1977. 635 pages. Journal of Clinical Ultrasound 1978;6:126-127.
32. Wild JJ. The use of ultrasonic pulses for the measurement of biological tissues and the detection of tissue density changes. Surgery 1950;27:183-199.
33. Beranek LL America Aso. Acoustics. [S. L.]: American institute of physics for the Acoustical society of America, 1990.
34. Bushberg JT. The essential physics of medical imaging. Philadelphia: Wolters Kluwer Health/Lippincott Williams & Wilkins, 2012.
35. Hill CR, Bamber JC Haar Gt. Physical principles of medical ultrasonics. Chichester ; Hoboken, N.J.: John Wiley & Sons, 2004.
36. Duck FA, Baker AC Starritt HC. Ultrasound in medicine. Bristol ; Philadelphia, Pa.: Institute of Physics Pub., 1998.
37. Shung KK, Cannata JM Zhou QF. Piezoelectric materials for high frequency medical imaging applications: A review. J Electroceram 2007;19:141-147.
38. Ritter T, Geng X, Kirk Shung K, Lopath PD, Park SE Shrout TR. Single crystal PZN/PT-polymer composites for ultrasound transducer applications. IEEE Trans Ultrason Ferroelectr Freq Control 2000;47:792-800.
39. Wells PNT. Biomedical Ultrasonics. London: Academic, 1977.
40. Mast TD. Empirical relationships between acoustic parameters in human soft tissues. Acoustics Research Letters Online 2000;1:37-42.
41. Salter BJ, Wang B, Szegedi MW, et al. Evaluation of alignment error due to a speed artifact in stereotactic ultrasound image guidance. Physics in Medicine and Biology 2008;53:N437-N445.
42. Fontanarosa D, van der Meer S, Harris E Verhaegen F. A CT based correction method for speed of sound aberration for ultrasound based image guided radiotherapy. Med Phys 2011;38:2665-2673.
43. Fontanarosa D, van der Meer S, Bloemen-van Gurp E, Stroian G Verhaegen F. Magnitude of speed of sound aberration corrections for ultrasound image guided radiotherapy for prostate and other anatomical sites. Med Phys 2012;39:5286-5292.
44. Fontanarosa D, Pesente S, Pascoli F, Ermacora D, Rumeileh IA Verhaegen F. A speed of sound aberration correction algorithm for curvilinear ultrasound transducers in ultrasound-based image-guided radiotherapy. Phys Med Biol 2013;58:1341-1360.
45. McNair HA, Mangar SA, Coffey J, et al. A comparison of CT- and ultrasound-based imaging to localize the prostate for external beam radiotherapy. Int J Radiat Oncol Biol Phys 2006;65:678-687.
46. Peng C, Kainz K, Lawton C Li XA. A Comparison of daily megavoltage CT and ultrasound image guided radiation therapy for prostate cancer. Medical Physics 2008;35:5619.

47. Scarbrough TJ, Golden NM, Ting JY, et al. Comparison of ultrasound and implanted seed marker prostate localization methods: Implications for image-guided radiotherapy. Int J Radiat Oncol Biol Phys 2006;65:378-387.
48. Little D. Use of portal images and BAT ultrasonography to measure setup error and organ motion for prostate IMRT: implications for treatment margins. International Journal of Radiation Oncology*Biology*Physics 2003;56:1218-1224.
49. Napolitano D, Chou C-H, McLaughlin G, et al. Sound speed correction in ultrasound imaging. Ultrasonics 2006;44:e43-e46.
50. Robinson DE, Ophir J, Wilson LS Chen CF. Pulse-echo ultrasound speed measurements: progress and prospects. Ultrasound Med Biol 1991;17:633-646.
51. J. F. Greenleaf SAJ, W. F. Wamoya, and F. A. Duck. Algebraic reconstruction of spatial distributions of acoustic velocities in tissue from their time-of-flight profiles. Acoustical Holography. New York: H. Booth, 1975; 71-90.
52. S. A. Johnson JFG, W. F. Samayoa, F. A. Duck, and J. D. Sjostrand. Reconstruction of three-dimensional velocity fields and other parameters by acoustic ray tracing. Proc. 1975 Ultrasonic Symposium. 197546-51.
53. Norton SJ Linzer M. Ultrasonic reflectivity imaging in three dimensions: reconstruction with spherical transducer arrays. Ultrason Imaging 1979;1:210-231.
54. Norton SJ Linzer M. Ultrasonic reflectivity tomography: reconstruction with circular transducer arrays. Ultrason Imaging 1979;1:154-184.
55. Fontanarosa D, van der Meer S Verhaegen F. On the significance of density-induced speed of sound variations on US-guided radiotherapy. Med Phys 2012;39:6316-6323.
56. Fenster A, Downey DB Cardinal HN. Three-dimensional ultrasound imaging. Phys Med Biol 2001;46:R67-99.
57. Fenster A, Parraga G Bax J. Three-dimensional ultrasound scanning. Interface Focus 2011;1:503-519.
58. Fenster A Downey DB. Three-dimensional ultrasound imaging and its use in quantifying organ and pathology volumes. Anal Bioanal Chem 2003;377:982-989.
59. Brinkley JF, Muramatsu SK, McCallum WD Popp RL. In vitro evaluation of an ultrasonic three-dimensional imaging and volume system. Ultrason Imaging 1982;4:126-139.
60. Greenleaf JF, Belohlavek M, Gerber TC, Foley DA Seward JB. Multidimensional visualization in echocardiography: an introduction. Mayo Clin Proc 1993;68:213-220.
61. Rankin RN, Fenster A, Downey DB, Munk PL, Levin MF Vellet AD. Three-dimensional sonographic reconstruction: techniques and diagnostic applications. AJR Am J Roentgenol 1993;161:695-702.
62. Smith WL Fenster A. Optimum scan spacing for three-dimensional ultrasound by speckle statistics. Ultrasound Med Biol 2000;26:551-562.
63. Pagoulatos N, Haynor DR Kim Y. A fast calibration method for 3-D tracking of ultrasound images using a spatial localizer. Ultrasound Med Biol 2001;27:1219-1229.
64. Geiser EA, Christie LG, Jr., Conetta DA, Conti CR Gossman GS. A mechanical arm for spatial registration of two-dimensional echocardiographic sections. Cathet Cardiovasc Diagn 1982;8:89-101.
65. Brinkley JF, McCallum WD, Muramatsu SK Liu DY. Fetal weight estimation from lengths and volumes found by three-dimensional ultrasonic measurements. J Ultrasound Med 1984;3:163-168.
66. Detmer PR, Bashein G, Hodges T, et al. 3D ultrasonic image feature localization based on magnetic scanhead tracking: in vitro calibration and validation. Ultrasound Med Biol 1994;20:923-936.
67. Housden RJ, Gee AH, Treece GM Prager RW. Sensorless reconstruction of unconstrained freehand 3D ultrasound data. Ultrasound Med Biol 2007;33:408-419.
68. Chen J-F, Fowlkes JB, Carson PL Rubin JM. Determination of scan-plane motion using speckle decorrelation: Theoretical considerations and initial test. International Journal of Imaging Systems and Technology 1997;8:38-44.
69. Nelson TR, Pretorius DH, Sklansky M Hagen-Ansert S. Three-dimensional echocardiographic evaluation of fetal heart anatomy and function: acquisition, analysis, and display. J Ultrasound Med 1996;15:1-9 quiz 11-12.

70. Lee W. 3D fetal ultrasonography. Clin Obstet Gynecol 2003;46:850-867.
71. Deng J Rodeck CH. Current applications of fetal cardiac imaging technology. Curr Opin Obstet Gynecol 2006;18:177-184.
72. Bamber JC, Eckersley RJ, Hubregtse P, Bush NL, Bell DS Crawford DC. Data-Processing for 3-D Ultrasound Visualization of Tumor Anatomy and Blood-Flow Visualization in Biomedical Computing, 1992, vol. 1808: SPIE, 1992; 651-663.
73. Fenster A, Surry K, Smith W, Gill J Downey DB. 3D ultrasound imaging: applications in image-guided therapy and biopsy. Computers & Graphics 2002;26:557-568.

Physical density to drive speed of sound aberration correction

Chapter 3

A CT based correction method for speed of sound aberration for ultrasound based image guided radiotherapy

Davide Fontanarosa
Skadi van der Meer
Emma Harris
Frank Verhaegen

Published in: Medical Physics 38(5):2665-2673, 2011.

Abstract

Purpose

To introduce a correction for speed of sound (SOS) aberrations in three dimensional (3D) ultrasound (US) imaging systems for small but systematic positioning errors in image guided radiotherapy (IGRT) applications. US waves travel at different speeds in different human tissues. Conventional US-based imaging systems assume that SOS is constant in all tissues at 1540 m/s which is an accepted average value for soft tissues. This assumption leads to errors of up to a few millimeters when converting echo times into distances and is a source of systematic errors and image distortion in quantitative US imaging.

Materials & Methods

At simulation, US applications for IGRT provide a computed tomography (CT) image co-registered to a US volume. The CT scan provides the physical density which can be used in an empirical relationship with SOS. This can be used to correct for different SOS in different tissues within the patient. For each US scan line each voxel's axial dimension is rescaled according to the SOS associated to it. This SOS correction method was applied to US scans of a PMMA container filled with either water, a 20% saline water solution or sunflower oil, and the results were compared to the CT. The correction was also applied to an US quality assurance (QA) phantom containing rods with high ultrasound contrast. This phantom was scanned with US through a container filled with the same three liquids. Finally, the algorithm was applied to two clinical cases: a prostate cancer patient and a breast cancer patient.

Results

After the correction was applied to the phantom images, spatial registration between the bottom of the phantom in the US scan and in the CT scan was improved; the difference was reduced from a few millimeters to less than one millimeter for all three different liquids. Reference structures in the QA phantom appeared at more closely corresponding depths in the three cases after the correction, within 0.5 mm. Both clinical cases showed small shifts, up to 3 mm, in the positions of anatomical structures after correction.

Conclusions

The SOS correction presented increases quantitative accuracy in US imaging which may lead to small but systematic improvements in patient positioning.

3.1 Introduction

Ultrasound (US) imaging is an important cross-sectional imaging modality in diagnostic radiology and is proving to be a useful quantitative tool also in the field of radiotherapy treatment verification (1-9). Organ motion and changes in shape and volume, and setup errors are issues of increasing importance for Intensity Modulated Radiation Therapy (IMRT) treatments (10-12). Accurate patient positioning is now a major requirement, as shown by the increasing interest in Image Guided Radiation Therapy (IGRT). US scanning may provide a fast, reliable, cost-effective IGRT technique. In addition, modern US imaging systems provide sufficient soft tissue contrast to allow reliable organ segmentation (13-16).

Most US devices use a pulse-echo technique (17) in which the transducer emits a very short pulse then listens for the echoes reflected from the scanned volume. The time of flight (TOF) of these echoes is then used to establish the distance from the transducer to the reflecting medium. The TOF depends on the speed of sound (SOS) in the tissues traversed by the beam; sound travels at different speeds in different media. The range of sound speed in average soft human tissues at body temperature (37°C) is 1450 m/s in fat to 1613 m/s in connective tissue (19). Standard practice in US imaging is to assume a fixed value for the SOS of 1540 m/s (20) which can lead to errors in SOS of up to 6% and, therefore, errors in distances estimated using US. The assumption of constant SOS has been made because real time correction of SOS aberrations for individual tissue types was not practical and because, until recently, US techniques were mainly used in qualitative diagnostic imaging (20) rather than quantitative distance and volume measurements. For quantitative measurements, this assumption may lead to errors in measurements of organ boundary positions of several millimeters, especially in cases where the organ is deeply seated and where the path of US waves is through tissues with a SOS significantly different from 1540 m/s. For example, for a region of interest situated at 10 cm depth in tissue with SOS in the 1450-1613 m/s range, SOS aberration could result in a maximum error of 6 mm in the measured position. For tissues with SOS outside this range the error is larger. The deeper the region of interest, the longer the path and, therefore, the larger the aberration. If along the US path tissues are present with SOS that are both higher and lower than 1540 m/s, their effect might partially cancel out and the final error may not be evident. An example of this situation is prostate imaging in which both fat and muscle tissues may overlay the prostate, which are on the opposite sides of the SOS range. Several cases of small measured differences between organ positions in the prostate determined by US and CT imaging was reported in the literature (21-24). These differences may be partially explained by the SOS aberration in US imaging.

The effect of the SOS aberration is expected to be more evident in cases like gynaecological or breast cancer patients, where in some cases mostly fat tissue is overlying the region of interest and therefore the aberration is only in one direction.

SOS in fat tissue was reported to be 1475 m/s (19), which is 4% lower than the standard 1540 m/s: so distances in a US scan will appear longer by a few millimeters (Table 1). Also, for liver applications (where the SOS was reported to be 1595 m/s (19), but depends on the fat content of the liver) small but significant distance errors may occur.

In this work, a method was proposed to implement a SOS aberration correction in 3D US scans in those cases where a spatially registered CT scan is also available. A CT scanner calibrated in terms of Hounsfield Unit (HU) versus physical density by means of a standard density calibration phantom was used to establish a HU-density relationship. This relationship was used to create a SOS map of every pixel in US images of ultrasound phantoms which had been co-registered with CT images. The map was then used to rescale voxels' axial dimensions along each line of view of the US volume, thus correcting SOS induced image distortions. This method was applied to two patient image datasets to demonstrate its clinical application.

Table 1: SOS values for different human soft tissues at 37°C: the data were taken from: Mast T.D., "Empirical relationship between acoustic parameters in human soft tissues", ARLO. 2000; 1, Issue 2: pp. 37-42. (19).

Tissue type	Density (g/cm^3)	Speed of sound (m/s)
Connective	1.120	1613
Muscle	1.050	1547
Fat	0.950	1478
Adipose	0.950	1450
Blood	1.060	1584
Brain	1.040	1560
Breast	1.020	1510
Kidney	1.050	1560
Liver	1.060	1595
Muscle, cardiac	1.060	1576
Muscle, skeletal	1.050	1580
Skin	1.090	1615
Average soft tissue: Fatty	0.985	1465
Average soft tissue: Non-fatty	1.055	1575
Blood cells	1.093	1627
Blood plasma	1.027	1543
Spinal cord	1.038	1542
Spleen	1.054	1567
Testis	1.044	1595
Mean	1.042	1557
Standard deviation	0.043	50

3.2 Materials & Methods

Clarity™ 3DUS System

All US scans were performed using a Clarity 3DUS System (Resonant Medical Inc., Montreal, Quebec, Canada). The system consists of a set of diagnostic US probes, each for a different anatomical region. Probes are fitted with an array of infrared reflectors and a ceiling-mounted optical tracking system and software components are used to acquire and rebuild 3DUS images data for patient positioning and soft tissue anatomy assessment. The ClarityTM system consists of two 3DUS devices: one located in the CT simulation room and the other located in the treatment room. A registration algorithm is used to compare the 3DUS images acquired in the simulation room with those acquired in the treatment room prior to every treatment session. Both US image datasets are referenced to the same coordinate system. In this way, the patient's position before every treatment can be compared to their position at simulation to determine whether shifts or re-planning are required to irradiate the radiotherapy target volume accurately whilst at the same time sparing organs at risk. CT images are also acquired at simulation therefore enabling calculation of the true delivered fractional dose in conjunction with a treatment planning system (7). In this work two probes were used to acquire US image data. All phantom data were acquired using a linear US probe provided with the system (linear probe: type L14 – 5/38, center frequency 7.2 MHz, Sonix Series, Ultrasonix Medical Corporation, Richmond, BC, Canada) and patient data were acquired using the linear probe and a curvilinear probe(curvilinear probe: type C5 – 2/60, center frequency 3.5 MHz, Sonix Series, Ultrasonix Medical Corporation, Richmond, BC, Canada).

Density to SOS relationship

The Clarity™ System can be used to perform a CT–US fusion, where the CT image can provide information about the physical densities of the tissues traversed by the US waves. SOS in a medium is inversely proportional to the square root of the density ρ of the medium; it is also inversely proportional to the square root of its compressibility K or directly proportional to the square root of its bulk modulus β (for materials which do not exhibit any time dependent response) (25):

$$SOS = \frac{1}{\sqrt{\rho K}} = \sqrt{\frac{\beta}{\rho}}. \qquad (3.1)$$

Compressibility K indicates the fractional decrease in volume when pressure is applied to the material.

Often in soft human tissues a change in density is coupled with a larger and opposing change in compressibility that varies more rapidly than density and therefore is the

dominant factor in the determination of SOS. The overall empirical effect is that as density increases the velocity of US in soft tissue also increases, and the relationship can be approximated as a linear dependence (19). For the soft tissue used in this work (Table 1) we obtained the following relationship using linear regression:

$$SOS = (1.09 \cdot \rho + 0.419) \cdot 10^3 m/s \pm 3.5 m/s. \quad (3.2)$$

There was a strong correlation between SOS and physical density for soft human tissues: the Pearson correlation coefficient was 0.92, and the p-value = 2.03 x 10^{-9} (Fig. 1).

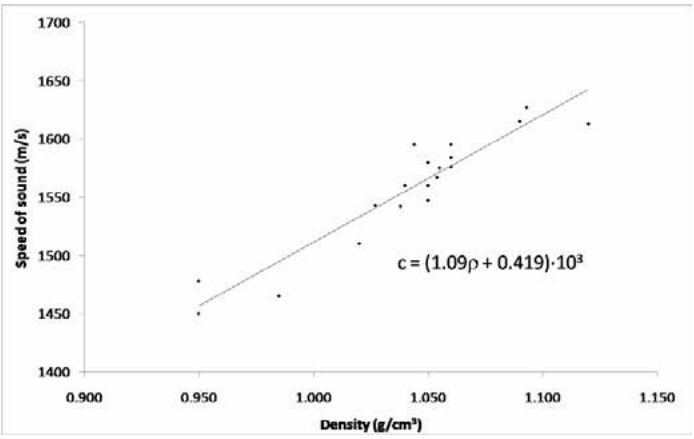

Fig. 1:. SOS versus density linear relationship for human soft tissues at 37°C: the data were taken from: Mast T.D., "Empirical relationship between acoustic parameters in human soft tissues", ARLO. 2000; 1, Issue 2: pp. 37-42. (19).

SOS aberration correction

The following is a description of the algorithm that was used to correct for SOS aberration. The method was applied to the DICOM CT dataset exported from the Clarity™ System with its native resolution (512 by 512 pixels), and to the B-mode US dataset with its resolution matched to the CT scan. The linear dependence of SOS on tissue density is used to correct SOS aberrations: from the multimodality CT-US image fusion, density values is associated with corresponding regions in the US scan and used to obtain the proper SOS in those regions. The first step consists of transforming the HU of the CT scan in physical densities through the CT scanner HU-to-density relation. Then, the density map is converted to a SOS map using EQ. 3.2. At this point, the SOS matrix volume is re-sliced along the US imaging planes, such that they are aligned in 3D, and re-sampled on the US spacing grid so that CT and US volume images have spatially matching voxels. Finally, they are re-sized to have equal dimensions. The

depth, d, of structures reflecting or scattering US pulses are calculated by the US system along each line of view using the TOF of the pulse assuming SOS equal to 1540 m/s throughout the scanned volume:

$$d = \frac{TOF}{2} SOS_{ref} \tag{3.3}$$

where SOS_{ref} is the assumed value for SOS, 1540 m/s. However, SOS is not constant inside the volume, so the actual depth, d_{corr}, is:

$$d_{corr} = \frac{1}{2} \sum_{j=1}^{n} SOS_j (TOF_j - TOF_{j-1}) \tag{3.4}$$

where j is an index which increases each time the US pulse traverses an interface between tissues with different acoustic impedance Z (a reflection of the US beam occurs every time Z changes), SOS_j is the local SOS in the tissue j and TOF_j is the time of flight of the pulse to the j^{th} interface and back to the US probe. Minor changes in Z occur on a very small scale, smaller than the US wavelength, and these can produce scatter (this is why standard US systems are optimized to display scattered signal and not reflected signal, in order to see also minimal changes in tissues). The smallest dimension available in an US scan is the voxel dimension and therefore tissue variations reported in EQ. 3.4 can be considered on a voxel-by-voxel basis, with the index j as the number of the voxels along the axial direction, i.e. in the direction of ultrasound propagation. Every voxel along every column must be resized in the axial direction from the dimension d_i in the original US scan to the dimension $d_{i,corr}$:

$$d_i = \frac{1}{2} SOS_{ref} \cdot (TOF_i - TOF_{i-1}) \tag{3.5}$$

$$d_{i,corr} = \frac{1}{2} SOS_i \cdot (TOF_i - TOF_{i-1}) . \tag{3.6}$$

From the previous two equations, it follows that the original US scan voxels' axial dimensions can be corrected using the local SOS variation value, ΔSOS_i, defined as the ratio between the local SOS as provided by the SOS map (SOS_i) and the reference value SOS_{ref} = 1540 m/s:

$$d_{i,corr} = \frac{SOS_i}{SOS_{ref}} d_i = \Delta SOS_i \cdot d_i . \tag{3.7}$$

From an operational point of view, the correction needs to be discretized and, since these corrections are expected to be a few percent for each voxel (similar to the change in SOS values in the range of soft human tissues with respect to the reference value of 1540 m/s), the correction algorithm first creates a ΔSOS matrix dividing the

SOS matrix by the reference value of 1540 m/s and then rescales it with a scaling factor which was chosen to be 100 to work only with integer numbers:

$$\Delta SOS_{100} = 100 \cdot \Delta SOS. \tag{3.8}$$

After this, another matrix $\Delta SOS'_{100}$ is created by replicating every voxel along every column of this matrix 100 times. Then a matrix US_{corr} is created where every column j is constructed from the top adding $\Delta SOS'_{100}(1,j)$ voxels with the value $w_1 = UI(1,j)$, where UI is the original US matrix.Next the algorithm adds $\Delta SOS'_{100}(\Delta SOS_{100}(1,j)+1,j)$ voxels with the value $w_2 = UI(2,j)$. Then $\Delta SOS'_{100}(\Delta SOS_{100}(1,j)+\Delta SOS_{100}(2,j)+1,j)$ voxels with the value $w_3 = UI(3,j)$, and so on, adding at the n^{th} step $\Delta SOS'_{100}(\sum^{n}\Delta SOS_{100}(n-1,j)+1,j)$ voxels with the value $w_n = UI(n,j)$ (Fig. 2a). This way the algorithm automatically selects the best spatially matching SOS voxel to apply the correction since after each contraction or expansion of US scan voxels, due to different SOS values, US and SOS matrices may no longer be equal length. Finally, the matrix needs to be re-sampled to the original resolution; a weighted average is implemented to lose as little information as possible:

$$US^{C}_{f,j,i} = \frac{\sum_{k=ni+1}^{n(i+1)} US^{corr}_{f,j,k}}{n}. \tag{3.9}$$

where US^{C} is the final corrected matrix, n is the scaling factor (in this case n = 100), f is the frame index, j is the column index and i is the row index (Fig. 2b).

It should be pointed out that in its current form the algorithm should only be applied to US scans performed using a linear probe, where the B-mode scan lines correspond to a very good approximation to the lines of view of the probe. For other types of probes, the correction should be applied along the lines of view, which can be extracted from the US raw data which has not been scan converted for the purpose of image display. Alternatively, the correction may be considered valid for the central portion of the scan in which the lines of view are approximately aligned with vertical image lines and which, if imaging is performed correctly, should contain the target volume.

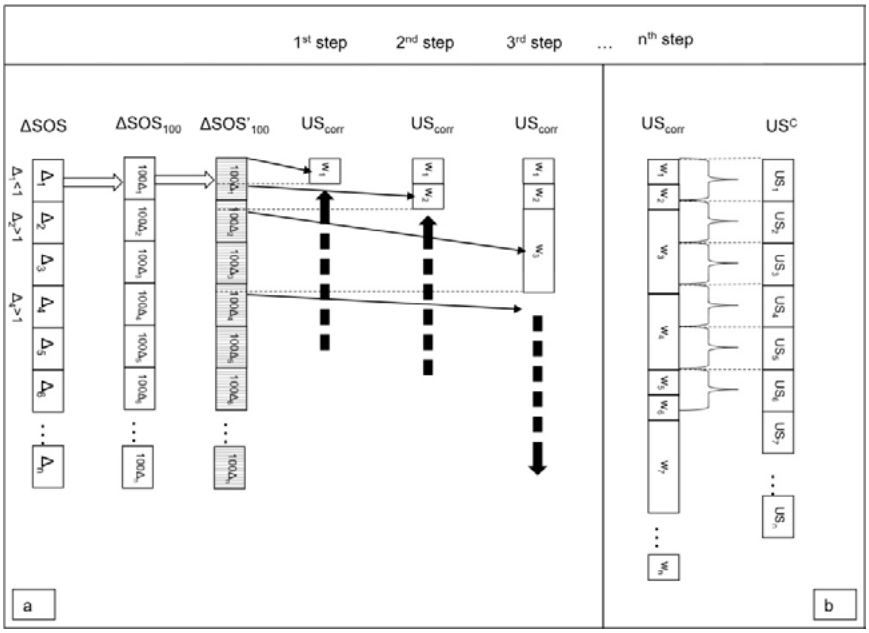

Fig. 2. a) The corrected US scan is created sequentially adding along each column a number of voxels corresponding to the value of SOS variation in the physically matching SOS variation map voxel. **b)** The final matrix is obtained by resampling the corrected US matrix to the original US scan resolution and assigning to each voxel sequentially the value averaged every 100 voxels of the corrected US matrix (100 is the rescaling factor chosen in order to lose as little information as possible considering that expected SOS variations are in the order of a few percents).

Measurements

The algorithm was first applied to a standard cubic 1000 cm^3 PMMA container, filled with liquids with different SOSs: a 20% saline solution, sunflower oil and water. The liquids were at a temperature of 20°C, so it was necessary to obtain a density versus SOS relationship at the same temperature in order to test the algorithm. Table 2 gives reported the values of SOS and density used, and the linear relationship derived was:

$$SOS = (0.64 \cdot \rho + 0.85) \cdot 10^3 m/s . \quad (3.10)$$

Table 2: The values of SOS and density at 20°C for the three liquids used to obtain the SOS versus density relationship to test the algorithm applied to the PMMA container.

Liquid [20 °C]	Density (g/cm^3)	Speed of sound (m/s)
20% saline solution	1.158	1600
Water	0.998	1480
Sunflower oil	0.917	1450
Mean	1.024	1510
Standard deviation	0.123	79

The probe was held in a vertical position using a plastic support and care was taken to position the probe surface in direct contact with the liquids ensuring that no air was trapped in between the probe and the liquid (Fig. 3a). CT and US scans were performed sequentially, and Implicit Registration™ software provided the matching of their frames of reference (Fig. 4). Matching of the CT and US DICOM datasets, exported from Clarity™, was reproduced using software written in the MATLAB® programming environment (MathWorks, Natick, Massachusetts) and using the coordinate transformation provided by Clarity™.

A second set of measurements was performed on the Clarity™ Calibration Phantom: this was provided by the manufacturer for routine quality assurance (QA) procedures on the system. It contained six high-contrast rods of 12 mm diameter, four high-contrast rods of 5 mm diameter, one high-contrast top sphere of 15 mm diameter and one high-contrast bottom sphere of 30 mm diameter. The measurements were taken by immersing the probe, held in place by a support, in a container filled with the same liquids as in the first set of measurements (Fig. 3b). This allowed the structures in the QA phantom to be imaged through layers of liquids with SOS differing from the reference value of 1540m/s. The known SOS of the liquids were used for correction in the US image of the container. This was done because the shift was expected to be small as the path of US in the liquid which generates the shift was short and the CT scan was insufficient to resolve the shift (CT resolution was ~1 mm in the antero-posterior direction and shifts were less than half the diameter of the reference structures, ~ 2 mm). The shift was clearly visible in the US scan which offers a higher resolution in the same direction (0.33 mm).

Finally, the correction algorithm was applied to a clinical prostate cancer case and a breast cancer case with a seroma-filled post-operative cavity to assess the magnitude of shifts in real clinical situations.

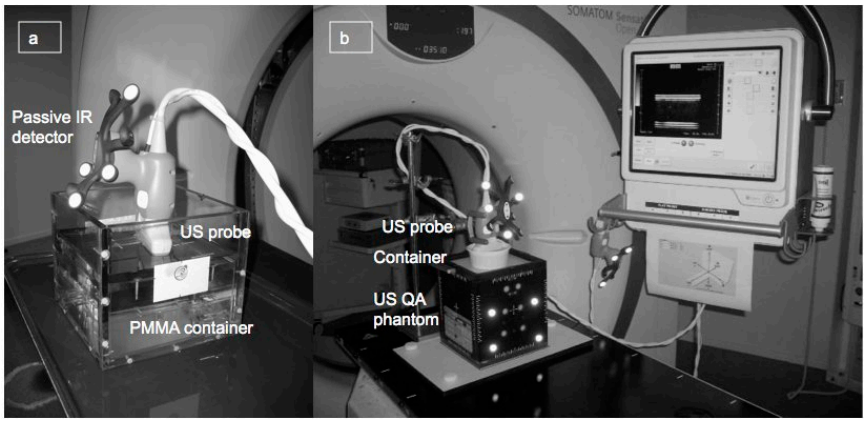

Fig. 3. a) Setup for the measurements with the PMMA phantom. **b)** Setup for the measurements with the ClarityTM Calibration phantom.

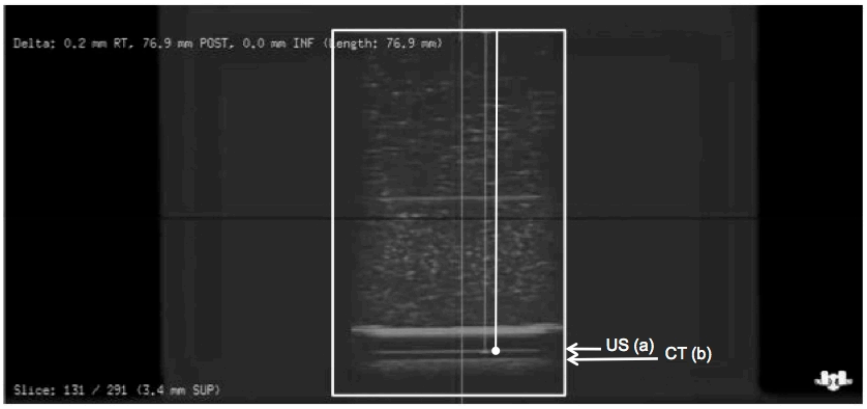

Fig. 4: CT and US scan superposition with Implicit Registration™ in the Clarity™ system: the bottom of the container filled with a 20% saline solution is indicated with arrows according to the US scan (a) and to the CT scan (b). Its depth is measured as 76.9 mm in the US scan, while it is at 80 mm in reality as can also be seen from the CT scan.

3.3 Results

Comparisons between CT and US scans of the PMMA phantom filled with different liquids showed a difference in the position of the bottom surface in all three cases (Fig 5). The position of the inferior edge is ~3 mm shallower in the US scan than in the CT scan in the case of the 20% saline solution (top row) and a ~3 mm deeper in the other two cases (two bottom rows). After the application of the algorithm the differences are negligible, being less than the intrinsic resolution of the CT scan (1 mm) (Fig. 5). This demonstrates that the SOS correction algorithm can effectively re-establish good agreement with measured depths on a CT scan.

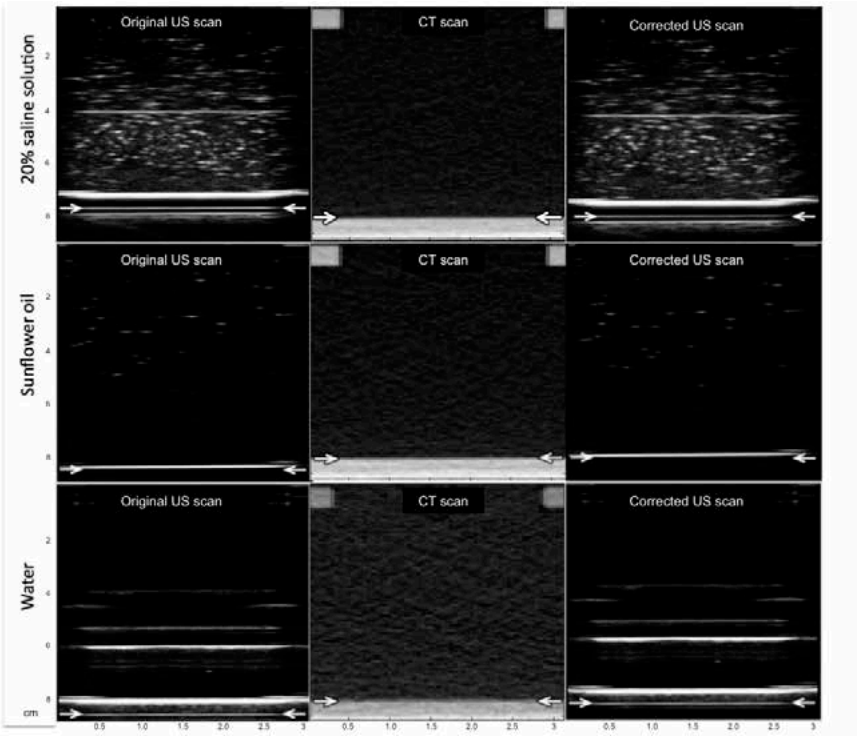

Fig. 5: Comparisons between the positions of the bottom surface of the PMMA phantom in the CT scans and in the US scans, before and after the application of the SOS aberration correction algorithm. The lines are indicated by arrows in order to distinguish them from other image artefacts.

In Fig. 6 the US images of the Clarity^{TM} calibration phantom scanned through liquid-filled containers (top row of Fig. 6) also show different positions of the 5 mm diameter high contrast rods situated at 3 cm depth. Their position was dependant on the liquid through which the phantom was imaged. Difference in position is ~2.5 mm (rod radii are also 2.5 mm) between the rod position imaged through 20% saline solution and the other two liquids. In the middle row of Fig.6 the images are split in two halves and the rod positions are visually compared. Visual comparison of rod positions post SOS aberration correction is given in the bottom row of Fig. 6 and in all cases the difference becomes negligible. Table 3 shows a quantitative comparison of the positions of reference structures in the PMMA phantom and in the QA phantom. The centers of the rods post correction were much closer to their known depth: their depth was within 0.5 millimeters from 3 centimeters. This showed that in complex setups differences in measured US depths vanish after correction with the SOS algorithm.

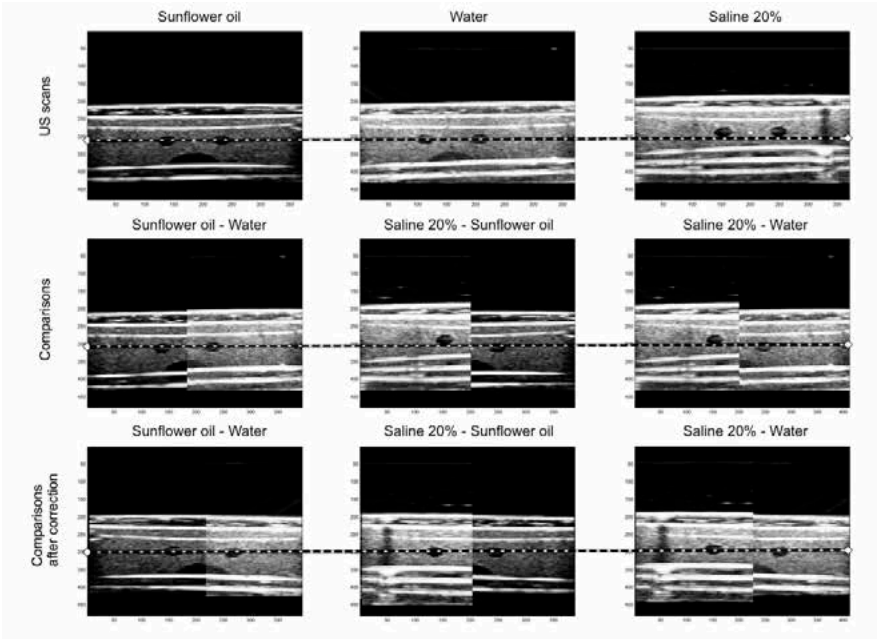

Fig. 6: Comparisons between the US scans of the Clarity^{TM} Calibration phantom as seen through three liquids with different SOS's: 1450 m/s for water, 1480 m/s for sunflower oil and 1600 m/s for 20% saline solution. In the second line the images were split in two halves to show visually the difference between the positions of the top rods in the different cases. In the third line the same comparison is shown after the SOS aberration correction was applied. The rods result at a much more similar depth after the application of the SOS correction. The horizontal white lines, instead, are image artefacts which have an erratic behaviour and do not represent any physical object, so they are not supposed to align after the correction has been applied.

Table 3: Quantitative comparison between the position of reference structures in phantoms before and after SOS aberration correction with errors in distances: in the PMMA phantom the reference structure is the bottom of the phantom and is at 8 cm depth; in the QA phantom, the reference structures are the most shallow rods and their centers are at 3 cm depth with respect to the surface of the phantom but at 6 cm depth with respect to the position of the probe at the surface of the liquids container on top of the phantom.

	Reference structure depth (real: 80 mm)			
	Before correction [mm]	Error [mm]	After correction [mm]	Error [mm]
PMMA phantom—20% saline	77.0	−3.0	79.5	−0.5
PMMA phantom—water	83.2	3.2	80.0	0.0
PMMA phantom—sunflower oil	84.8	4.8	80.5	0.5
Reference structure depth (real: 60 mm)				
QA phantom—20% saline	58.9	−1.1	60.0	0.0
QA phantom—water	61.2	1.2	59.5	−0.5
QA phantom—sunflower oil	61.8	1.8	60.0	0.0

Finally, the two clinical cases, a prostate cancer and a breast seroma, for which CT scans and US co-registered scans were available, showed that after the SOS correction was applied to the US scan anatomical structures shifted in the axial direction. In Fig. 7 the original US scans, the SOS variation maps and superpositions of the original and the corrected US scans are shown, where the differences are evident. A map of the distribution of voxel shifts after application of the SOS aberration correction is also given. Shifts of ~1 mm result for the breast case, always towards the surface of the patient as expected considering that mostly fat tissue is present and so the correction is in one direction. These shifts were small because the thickness of traversed tissue is small, the position of the distal wall of the seroma is at a depth of less than 3 centimeters; for larger breasts greater shifts could be obtained. The prostate cancer case shows shifts of up to 3 mm. These were both positive and negative since tissues with SOS higher and lower than the reference value are present. As previously explained, the algorithm is suitable for the breast case, which was scanned using a linear probe that produces B-mode images where vertical lines are correspondent to the effective lines of view. For the prostate cancer case, which was scanned using a curvilinear probe, only in the central portion of the image where the approximation with lines of view is acceptable do the shifts have reliable values. In Fig. 7 arrows indicate the actual approximate lines of view and a rectangle delineates the area where the algorithm can be considered applicable.

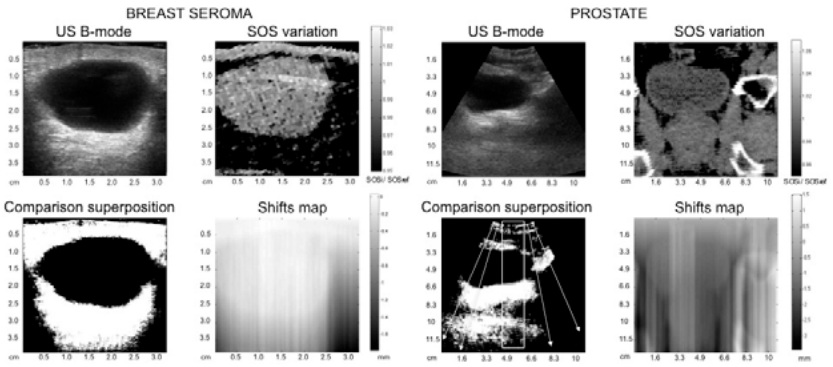

Fig. 7: Clinical cases: a breast seroma and a prostate. The US scan and the correspondent CT scan transformed in SOS variation map are shown on the top line. A superposition image of original and corrected US scans, with different contrast values in order to distinguish them, is shown in the inferior left part of the image. The prostate case was scanned with the curved probe so the algorithm is strictly applicable only in the central part of the figure (indicated). On the other parts, lines of view should be extracted from the RF data and the algorithm needs to be adapted to follow them, to have a reliable correction. In the inferior right part, instead, a map of the cumulative shifts is plotted, calculated as the total amount of shift applied to the tissue in that specific voxel. Shifts of up to 1.5 mm and 3.0 mm are evident in the breast and prostate cases respectively.

3.4 Discussion

SOS aberration in US imaging, leading to small but noticeable errors in depth assessments, is a phenomenon that has been reported before (26). Until now, only partial solutions have been proposed (27-30) due to the intrinsic difficulty in correcting the aberration using only the information provided by the US image. Also, individual SOS variations in tissues have not been considered previously. Moreover, the vast majority of applications of US imaging in radiology are qualitative, not quantitative. In the field of radiotherapy, the use of US imaging for treatment verification of patient positioning (possibly combined with dose recalculation) is a quantitative application where tissue structures must be aligned in an absolute spatial coordinate system. In some US verification systems the US images are coupled to a reference CT scan. This is the case for the Clarity™ 3DUS system which was used in this study. This system relies on a CT scan and a 3DUS scan recorded consecutively in the CT simulator room. CT images provide information about the physical densities of the tissues traversed by the US waves. The relationship between physical density and SOS can be used to transform the CT scan into a SOS map which can be used for a correction of the aberration based on voxel-by-voxel knowledge of the error introduced by a system assuming a fixed SOS of 1540 m/s. Measurements on homogeneous and heterogeneous phantoms demon-

strated the proposed correction method to be effective, and its application to clinical cases showed the magnitude of the error in the position of structures when the SOS aberration is not accounted for.

There are two possible strategies for the use of US imaging in radiotherapy: (1) an intramodality approach, and (2) an intermodality approach. In the former, US images acquired at treatment is compared to a US reference acquired at simulation, as for the Clarity™ system. In the latter, a CT scan is used as reference image and a US scan taken at the treatment is compared to it; this is the approach used by the BATCAM Multi-Probe system (Best Nomos, One Best Drive, Pittsburgh, PA 15202 USA): at the treatment stage 3DUS scans of the patient can be registered, in the ImageSync module, to the 3D regions of interest (ROI) created during the planning stage on the CT scan. If an intramodality approach is used the SOS aberration is expected to be present in both image sets (simulation and treatment) and the regions of interest will be, with a very good approximation, at the same positions if no real shifts or rotations occurred in between the two scans. If any differences are present in the position of the patient or in the tissue distribution at the treatment stage with respect to the simulation stage, the SOS distribution will consequently also change. This may create an SOS aberration artifact between simulation and treatment stages and a SOS aberration correction might prove to be necessary in those cases where a significant change in the patient is present between simulation and treatment. Moreover, the intramodality approach relies on semi-automated contouring of structures during simulation: the contouring process (especially if automated) may be sensitive to SOS aberrations which, being a source of distortion, blurring and lateral defocusing (27), decreases the precision in defining the boundaries of the structures. If the US scan is used as a secondary dataset to aid the planning process and to delineate the Planning Target Volume (PTV), small shifts of the target due to the SOS aberration could potentially introduce dose calculation errors.

For positioning systems using an intermodality approach the algorithm could be particularly useful. In this case, the correction would allow a more coherent comparison between organ positions in US and CT scans. Other US systems, 2D or 3D, which do not have a co-registered CT scan available, could also profit from the presented algorithm for a first order correction if the scans are always performed under the same conditions and the same tissues are imaged: a “standard” indicative SOS map can be implemented for all the scans with the known tissues’ values for certain organs, and a coarse correction can be performed.

The application of the algorithm to US images acquired with non-linear probes, or in general when lines of view are not parallel from the probe, will require the use of raw US data, since it must be applied along the lines of view which do not correspond to image columns any more. So it must be performed before the lines of view are converted into an image, since recreating the sound wave paths a posteriori from the image could introduce errors. On the other hand, it might not be always trivial to

retrieve this data from the US imaging system and therefore a correction of the image based on the presumed direction of lines of view according to the type of US scan device could be appropriate.

Application of the algorithm to anatomical sites other than breast or prostate may result in larger corrections, especially when tissue which all deviate from the reference SOS value in the same direction are present, i.e. the errors would be cumulative. This may be the case for female patients with pelvic cancers, where less muscle and typically more fat tissue is present and structures are deeper than breast case. Another case where the presented correction could significantly improve imaging quality is the liver cancer patient. The liver's very high SOS value (1595 m/s (19)), its homogeneous texture and possibly deeply seated tumors may result in SOS errors exceeding 5 mm for structures at a depth of 15 cm with standard US systems.

Reported cases of positioning discrepancies using US systems with respect to other imaging methods (21-25) might be partially explained by the presence of small but systematic SOS aberrations, so the implementation of the proposed correction could potentially introduce the need for a re-evaluation of these cases to assess its impact.

3.5 Conclusions

In the field of radiology US imaging systems are mostly used for qualitative applications, such as obstetric and vascular evaluations or as biopsy guidance. In contrast, in radiotherapy, US systems are used quantitatively to measure the absolute position of structures to ensure correct alignment with radiation beams. Aberrations limiting the accuracy should be corrected for. One source of small systematic errors is deviation of the SOS from a fixed reference value. The availability of a co-registered CT scan in some 3DUS systems for radiotherapy positioning applications allows the creation of an SOS map from the density distribution of the imaged materials through an empirical relationship. This map can be used to correct SOS aberrations on a voxel-by-voxel basis using an algorithm that was presented in this study. Phantom tests showed that after correction the US and CT images matched more closely. Contour outlining is sensitive to SOS aberrations since it increases blurring and lateral defocusing especially if some kind of automated segmentation is employed and therefore the correction may also improve segmentation of targets or organs at risk, thereby reducing the influence of small but systematic positional errors.

Aknowledgements

The authors wish to thank for their constant support Dr M. Lachaine, Dr S. Koptenko, Mr R. Lopes, Mr P. Fortier and Dr T. Falco of Resonant Medical Inc (incorporated in Elekta). We also wish to thank Prof J. Bamber of the Institute of Cancer Research in

London, UK for discussion. Dr A. Shaw of the National Physical Laboratory, Teddington, UK is thanked for the discussion on sound speed.

3.6 References

1. J. Lattanzi, S. McNeeley, W. Pinover, E. Horwitz, I. Das, T.E. Schultheiss, and G.E. Hanks, "A comparison of daily CT localization to daily ultrasound-based system in prostate cancer," Int. J. Radiat. Oncol., Biol., Phys. 43, 719–725 (1999).
2. J. Lattanzi, S. McNeeley, S. Donnelly, E. Palacio, A. Hanlon, T.E. Schultheiss, and T.E. Hanks, "Ultrasound-based stereotactic guidance in prostate cancer—quantification of organ motion and set-up errors in external beam radiation therapy," Comput. Aided Surg. 5, 289–295 (2000).
3. F. Trichter and R.D. Ennis, "Prostate localization using transabdominal ultrasound imaging," Int. J. Radiat. Oncol., Biol., Phys. 56(Suppl. 5), 1225–1233 (2003).
4. C.F. Serago, S.J. Chungbin, S.J Buskirk, G.A. Ezzell, A.C. Collie and S.A. Vora, "Initial experience with ultrasound localization for positioning prostate cancer patients for external beam radiotherapy," Int. J. Radiat. Oncol., Biol., Phys. 53, 1130–1138 (2002).
5. W. Wein, B. Roeper and N. Navab, "Integrating diagnostic B-mode ultrasonography into CT-based radiation treatment planning," IEEE Trans. Med. Imaging 26(6), 866-79 (2007).
6. T.S. Berrang, P.T. Truong, C. Popescu, L. Drever, H.A. Kader, M.L. Hilts, T. Mitchell, S.Y. Soh, L. Sands, S. Silver and I.A. Olivotto, "3D Ultrasound Can Contribute to Planning CT to Define the Target for Partial Breast Radiotherapy," Int. J. Radiat. Oncol., Biol., Phys. 73(Issue 2), 375-383 (2009).
7. D. Fraser, Y. Chen, E. Poon, F. Cury, T. Falco and F. Verhaegen, "Dosimetric consequences of misalignment and realignment in prostate 3D CRT using intramodality ultrasound image guidance," Med. Phys. 37, 2787-95 (2010).
8. D. Fraser, P. Wong, K. Sultanem, and F. Verhaegen, "Dosimetric evolution of the breast electron boost target using 3D ultrasound imaging," Radiother. Oncol. 96, 185-91, (2010).
9. D. Fraser, P. Fava, F. Cury, T. Vuong, T. Falco and F. Verhaegen, "Evaluation of a prototype 3D ultrasound system for multimodality imaging of cervical nodes for adaptive radiation therapy," Proceedings – SPIE The International Society for Optical Engineering 6509:65090Y.1-65090Y.8 (2007).
10. L. Xing, B. Thorndyke, E. Schreibmann, Y. Yang, T.F. Li, G.Y. Kim, G. Luxton and A. Koong, "Overview of image-guided radiation therapy," Med. Dos. 31(2), 91–112 (2006).
11. C.C. Ling, E. Yorke and Z. Fuks, "From IMRT to IGRT: frontierland or neverland?," Radiother. Oncol. 78, 119–122 (2006).
12. J. Purdy, "Current ICRU definitions of volumes: limitations and future directions," Seminars in Radiation Oncology 14(1), 27-40 (2004).
13. W.L. Smith, C. Lewis, G. Baumann, G. Rodrigues, D. D'Souza, R. Ash, D. Ho, V. Venkatesan, D. Downey and A. Fenster, "Prostate volume contouring: a 3D analysis of segmentation using 3DTRUS, CT, and MR," Int. J. Radiat. Oncol., Biol., Phys. 67(4), 1238-1247, (2007).
14. Y.L. Huang and D.R. Chen, "Automatic contouring for breast tumors in 2-d sonography," Conf. Proc. IEEE Eng. Med. Biol. Soc. 3, 3225-3228 (2005).
15. J.A. Molloy, S. Srivastava and B.F. Schneider, "A method to compare supra-pubic ultrasound and CT images of the prostate: technique and early clinical results," Med. Phys. 31(3), 433-442 (2004).
16. Y.L. Huang, Y.R. Jiang, D.R. Chen and W.K. Moon, "Level set contouring for breast tumor in sonography," J. Digit. Imaging 20(3), 238-247 (2007).
17. J.J. Wild, "The use of ultrasonic pulses for the measurement of biological tissues and the detection of tissue density changes," Surgery 27, 183-199 (1950).
18. J.C. Bamber, "Speed of sound," in *Physical Principles of Medical Ultrasonics* edited by C.R. Hill, J.C. Bamber, G.R. ter Haar, (Chichester, West Sussex PO19 8SQ, England: John Wiley & Sons, Ltd.; 2004), p. 178.
19. T.D. Mast, "Empirical relationship between acoustic parameters in human soft tissues," ARLO 1, Issue 2, 37-42 (2001).
20. P.N.T Wells, "Biomedical ultrasonics" (Academic Press, London, 1977).

21. H.A. McNair, S.A. Mangar, J. Coffey, B. Shoulders, V.N. Hansen, A. Norman, J. Staffurth, S.A. Sohaib, A.P. Warrington and D.P. Dearnaley, “A comparison of CT- and ultrasound-based imaging to localize the prostate for external beam radiotherapy,” Int. J. Radiat. Oncol., Biol., Phys. 65, 678–687 (2006).
22. C. Peng, K. Kainz, C. Lawton and X.A. Li, “A Comparison of daily megavoltage CT and ultrasound image guided radiation therapy for prostate cancer,” Med Phys. 35(12), 5619-5628 (2008).
23. T.J. Scarbrough, N.M. Golden, J.Y. Ting, C.D. Fuller, A. Wong, P.A. Kupelian and C.R. Jr. Thomas, “Comparison of ultrasound and implanted seed marker prostate localization methods: Implications for image-guided radiotherapy,” Int. J. Radiat. Oncol., Biol., Phys. 65, 378–387 (2006).
24. D.J. Little, L. Dong, L.B. Levy, A. Chandra and D.A. Kuban, “Use of portal images and BAT ultrasonography to measure setup error and organ motion for prostate imrt: implications for treatment margins,” Int. J. Radiat. Oncol., Biol., Phys. 56(5), 1218-24 (2003).
25. L.L. Beranek, “Acoustics,” New York: AIP; 1986.
26. D.B.J. Salter, B. Wang, M.W. Szegedi, P. Rassiah-Szegedi, D.C. Shrieve, R. Cheng and M. Fuss, “Evaluation of alignment error due to a speed artifact in stereotactic ultrasound image guidance,” Phys. Med. Biol. 53(23), N437-N445 (2008).
27. D. Napolitano, C.H. Chou, G. McLaughlin, T.L. Ji, L. Mo, D. DeBusschere and R. Steins, “Sound speed correction in ultrasound imaging,” Ultrasonics 44(Suppl 1), e43-e46 (2006).
28. R. M. Arthur, "Representation of Tissue for Pulse-Echo Estimation of Speed of Ultrasound," Donald L. Snyder Workshop, Washington University in St. Louis, Springer-Verlag (2000).
29. D.E. Robinson, J. Ophir, L.S. Wilson and C.F. Chen, “Pulse-echo ultrasound speed measurements: progress and prospects,” Ultrasound Med. Biol. 17(6), 633-646 (1991).
30. T.M. Powell, F. Van den Heuvel, M. Kahn, and J.D. Forman, “Independent prostate motion as measured by daily BAT ultrasound and electronic portal imaging,” Int. J. Radiat. Oncol., Biol., Phys. 51(Suppl. 1), 215–215 (2001).

Chapter 4

Magnitude of speed of sound aberration corrections for ultrasound image guided radiotherapy for prostate and other anatomical sites

Davide Fontanarosa
Skadi van der Meer
Esther Bloemen-van Gurp
Gabriela Stroian
Frank Verhaegen

Published in: Medical Physics 39(8):5286-5292, 2012.

Abstract

Purpose

The purpose of this work is to assess the magnitude of speed of sound (SOS) aberrations in three dimensional (3D) ultrasound (US) imaging systems in image guided radiotherapy (IGRT). The discrepancy between the fixed SOS value of 1540 m/s assumed by US systems in human soft tissues and its actual non homogeneous distribution in patients produces small but systematic errors of up to a few millimeters in the positions of scanned structures.

Materials & Methods

A correction, provided by a previously published density-based algorithm, was applied to a set of five prostate, five liver and five breast cancer patients. The shifts of the centroids of target structures and the change in shape were evaluated.

Results

After the correction the prostate cases showed shifts up to 3.6 mm towards the US probe, which may explain largely the reported positioning discrepancies in the literature on US systems versus other imaging modalities. Liver cases showed the largest changes in volume of the organ, up to almost 9%, and shifts of the centroids up to more than 6 mm either away or towards the US probe. Breast images showed systematic small shifts of the centroids towards the US probe with a maximum magnitude of 1.3 millimeters.

Conclusions

The applied correction in prostate and liver cancer patients shows positioning errors of several mm due to SOS aberration; the errors are smaller in breast cancer cases, but possibly becoming more important when breast tissue thickness increases.

4.1 Introduction

Ultrasound (US) imaging is gaining interest as a quantitative tool for soft tissue imaging for radiotherapy treatment guidance, particularly when conformal or more demanding treatments in terms of patient positioning accuracy are delivered[1, 2]. US imaging is applied in two different flavours: intermodality imaging[3], where at treatment stage US images are compared to the computerized tomography (CT) scans performed at simulation; and intramodality imaging[4-7], where treatment US images are compared to simulation US images. To this end, some form of Image Guided Radiation Therapy (IGRT)[8] is needed: US scanning systems provide a high resolution imaging technique for patient positioning without radiation dose.

Most diagnostic US devices use the time of flight (TOF) of reflecting US waves to establish distances inside the scanned tissues and thus create B-mode US images. The TOF depends on the speed of sound (SOS) in the specific tissues traversed by the beam, and sound waves travel at different speeds in different media. These differences can be rather important, ranging in human soft tissues at body temperature from 1450 m/s in fat to 1613 m/s in connective tissue[9]. The standard practice in US imaging is, however, to assume a fixed value for the SOS of 1540 m/s for all tissues[10], which leads to errors of up to 7% in SOS and, therefore, distance. This assumption may lead to errors in measurements of organ boundary positions of several millimeters.

In this work, a SOS correction algorithm previously published[11] was applied to US images of fifteen patients with different pathologies such as prostate cancer, liver cancer and breast cancer. The purpose was to assess the magnitudes of the effective US shifts of the structures of interest in the patient and of deformations of organ shapes. Prostate cancer patients were the primary focus of this work, since this is currently one of the most important applications of US in radiotherapy as well as a source of controversial results and discussions on positioning accuracy (see e.g. ref [12], as an example for the intermodality workflow). In the present work the focus is on the simulation stage where a CT image is fused with a reference US image. We will assume presently that a correction based on the simulation CT scan is also applicable to the subsequent treatment fractions, even if changes have occurred in the patient or in his position. US guidance workflow issues are a complex matter but they are outside the scope of this work and will be reported separately elsewhere.

US images sometimes result in higher imaging contrast than CT images for certain anatomical structures. For these cases contouring of structures may sometimes be beneficial in US images. The fused US/CT images may then lead to improved treatment planning. For the present study it is important to note that a SOS correction at the simulation stage alone would be required for this. An SOS correction may also lead to improved patient setup at the treatment stage.

4.2 Materials & Methods

Study cases

According to our previous work[11], the CT scans, coregistered in absolute coordinates to the simulation US scans, were used to create the SOS maps of the patients and then the latter were used to apply the correction on the original US images. This was performed by calculating the SOS value from the empirical relationship with physical density (EQ. 4.1) and then using the ratios between calculated and assumed SOS in each voxel; the latter were used to infer local differences in time of flight of US echoes, and hence distances, and finally these shifts were accumulated along the lines of view. More details are given in[11].

$$SOS = (1.09 \cdot \rho + 0.419) \cdot 10^3 m/s \pm 3.5 m/s \quad (4.1)$$

The prostate and liver patients were scanned at the MAASTRO Clinic (Maastricht, the Netherlands), while the breast patients were scanned at the Jewish General Hospital (Montréal, Canada), on identical 3DUS imaging systems. These pathologies are particularly indicated to take advantage of US imaging: prostate cancer patients, with a full bladder at the time of scan, can be transabdominally imaged with good results in terms of tissue contrast and target delineation, and represent currently the major application of US in IGRT. US scanning of liver is a very well established imaging modality in radiology and is particularly effective at recognizing internal structures and vein patterns which may be used as reference points for patient positioning in radiotherapy, where this imaging modality still needs to be established[13]. In breast cancer patients, who have an additional boost prescribed to the tumor bed following lumpectomy and adjuvant radiotherapy or are treated with partial breast irradiation (PBI), the seroma cavity, due to its very low echogenicity, is clearly visible on US scans as a uniform structure[6]. The specific pathologies used were selected to have a broad range of possible target localizations, organ shapes and scanning paths.

Image acquisition and processing

All US scans were performed using a Clarity 3D US System (Resonant Medical Inc., an Elekta division, Elekta, Crawley, United Kingdom). All the measurements performed on prostate and liver cancer patients were acquired using curvilinear probes (type C5 – 2/60, Center Frequency 3.5 MHz, Sonix Series, Ultrasonix Medical Corporation), while the scans on breasts were acquired using a linear US probe (type L14 – 5/38, Center Frequency 7.2 MHz, Sonix Series, Ultrasonix Medical Corporation, Richmond, BC, Canada).

The 3D US and CT coregistered datasets were exported from Clarity and imported in Osirix (Pixmeo SARL, 266 Rue de Bernex, CH-1233 Bernex, Switzerland). Using the

software tools, the fused 3D volumes were re-sliced along planes parallel to one of the original spatial frames of the US dataset, selected accordingly to the specific cancer site, as described in the following sections (Fig. 1). Then both the CT and the US images along the US plane were exported as DICOM files. The software also provides pixel dimensions for the images along these planes, which are different from the pixel dimensions of the exported CT scan from Clarity, due to the angle of the plane slicing through the image voxels.

Fig. 1: US and coregistered CT scans imported in Osirix as 3D volumes, fused using the registration shifts provided by the Clarity system and visualized in "3D Multi Planar Reconstruction (MPR)" mode, for a prostate patient. The coordinate system was tilted to have one of the projection planes aligned with the LOV of the US probe (white line in the figure in the upper left panel). In the lower left panel the oblique projection corresponding to a plane perpendicular to the LOV (grey line in the upper left panel) is shown. In the right panel is plotted the superposition of the CT and the US oblique planes along the LOV. The latter images were then exported to MATLAB.

Prostate cancer patients are scanned with a specific protocol: the probe is positioned approximately in correspondence to the prostate on the abdomen, then it is slid cranio-caudally towards the head until the top of the bladder is visible; next it is pivoted around the contact point until the whole prostate is encompassed. So all the 3D US volumes are approximately in the same position inside the patient and show the same distribution of tissues and organs: from the probe downwards along its line of view typically beyond the skin there are muscle and fat layers, the full bladder, the prostate and the rectum. Unlike the breast case, the target in these patients is deep-seated, at depths sometimes exceeding 10 cm. The images to be exported from Osirix were selected along the line of view of the probe corresponding to the maximum diameter of the prostate.

For liver cancer patients the scanning path is not fixed. For all the patients, the curvilinear probe is positioned between two ribs and a fan scan is performed orienting

the line of view according to the position of the target. In Osirix, the image to be exported was chosen as the central one in the fan shaped US dataset. This was done for reproducibility reasons since there was no clearly observable structure that could be used as a reference in all the datasets. The depths of targets can be very different ranging from a few cm to more than 20 cm if they are close to the distal edge of a large liver.

The scanning procedure for breast cancer patients consists in sliding the linear probe over the seroma region producing an approximately parallelepiped imaged volume. The imaged tissues mostly consist of adipose tissue with a rather shallow target, filled with seroma liquid (the patients in this study did not undergo mammoplasty), and a clear plane defined by the chest wall. Overall, the whole tissue layer imaged was just a few centimeter thick in all patients. The image selected was along the direction perpendicular to the probe scanning direction and corresponding to the largest diameter of the seroma cavity.

SOS aberration algorithm application

The 3D US and CT images were imported in a routine written in the MATLAB® programming environment (MathWorks, Natick, MA), which performed the following operations:

i. Selection of the overlapping area of the US and CT oblique images and cropping (Fig. 2a).
ii. Outline a region of interest (ROI) (typically the target or a structure of interest) (Fig. 2b).
iii. Creation of a mask corresponding to the internal area of the contour outlined and definition of the centroid of this mask (Fig. 2c).
iv. Application of the SOS correction algorithm to the image with the mask along the vertical columns according to the procedure described in [11] and consequent creation of a physical density map, a SOS map, a SOS variation map and a map of cumulative shifts (Fig. 3).
V. Creation of a new mask corresponding to the deformed mask shape with an edge detection algorithm, and definition of its centroid (Fig. 4).
Vi. Quantitative comparison between the position of the centroid of the original mask and the centroid of the one created after the application of the algorithm (Fig. 5a).
Vii. Qualitative comparisons between the shape and position of the original mask and the corrected one (subtraction image) (Fig. 5b).

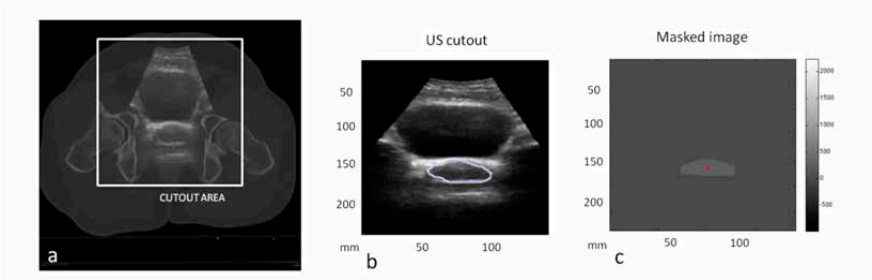

Fig. 2. a) Fused oblique CT and US scan planes of a prostate patient: the rectangle indicates the cropping area corresponding to the overlapping area of the two image modalities. The remaining part of the work was performed on the cropped images. **b)** An ROI is outlined by hand with a free hand drawing tool implemented in the MATLAB code. In the image, the prostate is contoured. **c)** The contour is transformed in a binary mask by setting the internal gray values to 255 and the external to 0. The software detects the centroid of the internal part of the mask (crossed dot).

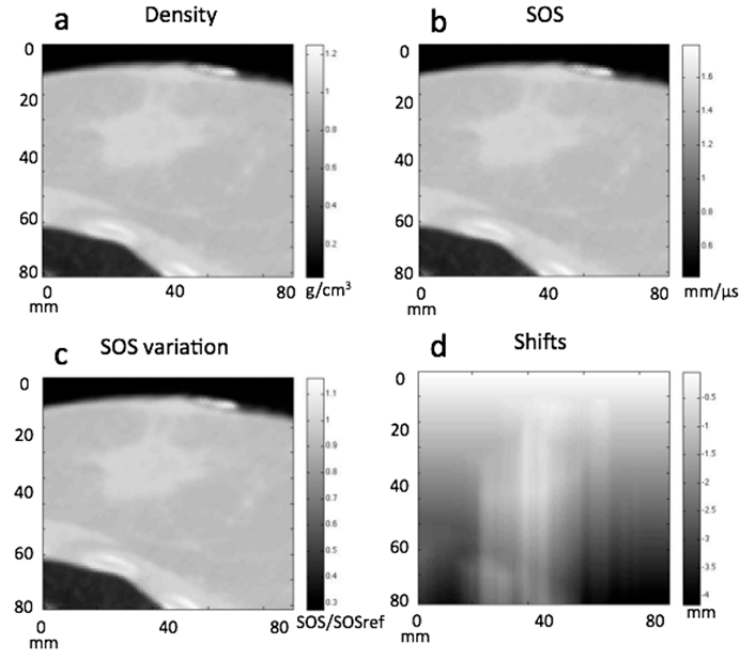

Fig. 3: Images created from the original CT scan of a breast cancer patient as an example of the procedure followed by the algorithm: a) physical mass density map; b) SOS map; c) SOS variation map; d) cumulative shifts map. The procedure to create these maps is described in detail in (11).

ROI definition

The ROIs outlined in step ii. of section II.C. were defined differently according to the type of pathology, with the purpose of assessing the effect of the SOS aberration correction algorithm in clinical situations:

i. Prostate*:* the contours correspond to the prostate.
ii. Liver: three different types of regions were contoured: the whole organ; a small circular dummy structure, approximately one centimeter in diameter, as close as possible to the upper edge of the liver, in order to simulate a very shallow target (Fig. 6a); and a similar structure as deep as possible inside the organ (Fig. 6b). The objective of this procedure was to assess the impact of the aberration correction on the liver as a whole but also on the shifts undergone by internal targets in extreme positions inside the organ. Due to the extension of the organ, an evaluation of its deformation was also performed estimating the relative shifts of proximal and distal walls (Fig. 6c).
iii. Breast: the contours correspond to the visible seroma.

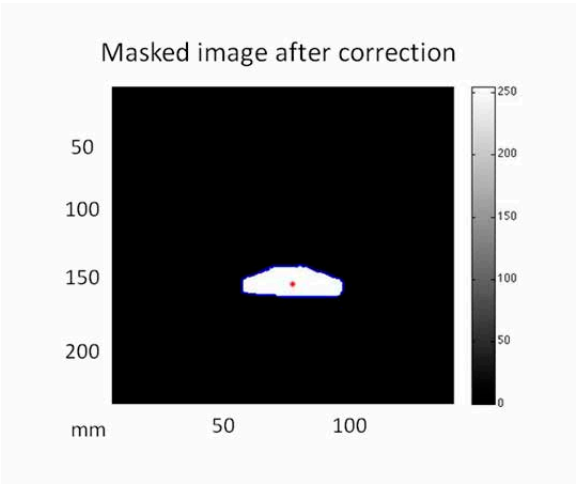

Fig. 4: After the application of the algorithm to the original mask image, a corrected image is created where the mask, corresponding to the position of the target (the prostate in this case), is shifted to the correct position. Using a basic edge detection algorithm the curve corresponding to the contour of the mask (in grey) is determined, allowing the calculation of the position of the centroid.

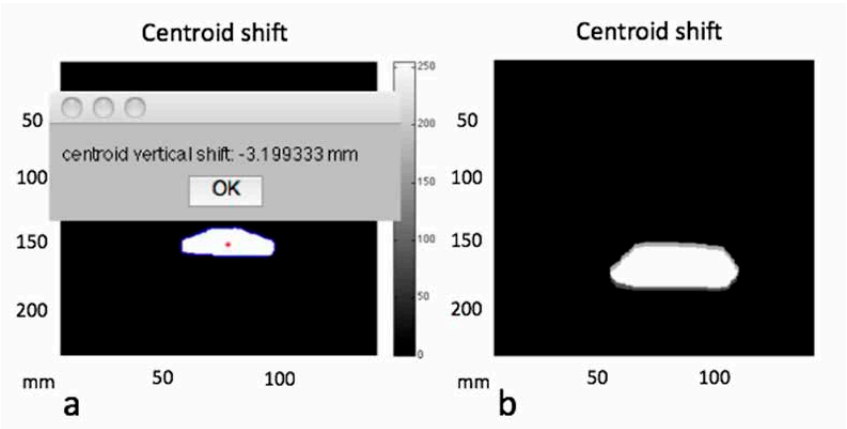

Fig. 5. a) The software calculates the position of the centroid of a prostate after the application of the correction, and provides the shift between the position of the centroid before and after the correction. **b)** A superposition image of a second prostate case, deeper situated and of a larger size to show this effect on the patient with the most significant SOS aberration present, where the two mask images before and after the application of the SOS aberration correction are clearly distinguishable: the white area is the common surface, the grey areas show the extent of the shift.

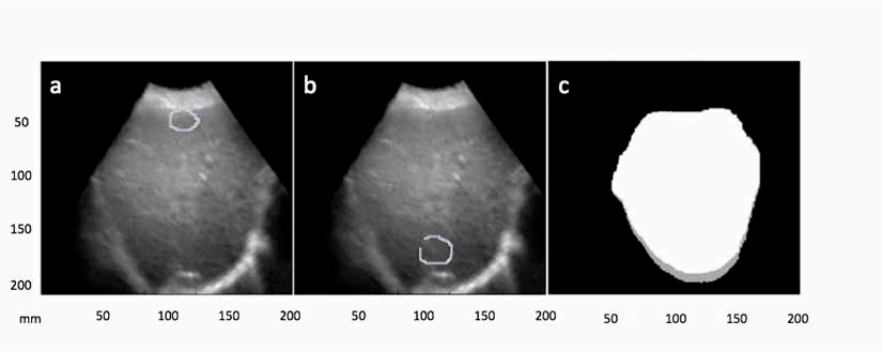

Fig. 6. a) Contour of a dummy shallow circular ROI inside the liver. **b)** Contour of a dummy deep circular structure inside the liver. **c)** Difference image between the non-corrected and the corrected mask images: in this specific patient (patient 3l) almost no shift is present for the proximal wall while the distal wall is shifted by more than 7 mm.

4.3 Results and Discussion

The algorithm was applied to five cases each of prostate, liver and breast cancer.

For the prostate cases the SOS aberration caused a maximum upward shift of 3.6 mm of the prostate (Table 1).

An evaluation of the prostate shape change revealed that the path length inside the organ is insufficient to create a significant difference in the correction of the position of the distal and proximal boundaries. Therefore, no significant prostate deformations due to the SOS aberration were noted. For these patients, reported positioning discrepancies using intermodality US systems compared to other imaging modalities[12, 14, 15] can be largely explained by SOS aberrations. The shifts reported here agree in direction and magnitude with the literature. The prostate errors reported here are along the line of view of the US probe, which is a composition of the cranio-caudal (CC) and the anterior-posterior (AP) directions. The recent literature (ref[16], Table X, intramodality workflow) reports the differences between shifts measured using US and other IGRT techniques. The average error is 1.3 mm (AP) and 2.3 mm (CC); with US images showing an apparent position for the prostate more dorsal and caudal than other IGRT systems. The average value reported in our study, 2.8 mm (Table 1), can be decomposed in its AP and CC projections, respectively 1.6 mm and 2.3 mm, which compare very well with the published values. It is, therefore, likely that the

SOS aberration in US imaging causes a significant part of the reported discrepancies between IGRT with US imaging and other techniques. For these patients a larger apparent depth of the prostate is produced by the SOS aberration, with different magnitudes according to the relative importance of the amount of fat tissue and urine content in the bladder (1520 m/s[17]) with respect to muscle tissue (1580 m/s[9]) overlying the prostate.

Table 1: Shifts reported for the centroids of prostates, livers and breast seromas, after the SOS aberration correction. Negative values indicate that the real position is shallower than what is shown on the US image, and vice versa. For livers, shifts of dummy ROIs and an estimate of volume change due to SOS aberration are also reported.

Body location	Patient	Shift of centroid of target (mm)	Target centroid depth (mm)	Difference between proximal and distal edges shifts (mm)	Shift of shallow ROI (mm)	Shift of deep ROI (mm)	Organ volume change (estimate) (%)
	1p	−1.3 (−1, 0.13, −0.8)	105.3	–	–	–	–
	2p	−3.6 (−2.8,0, −2.3)	151.0	–	–	–	–
Prostate	3p	−3.1(−2.6, −0.18, −1.7)	183.6	–	–	–	–
	4p	−3.3(−2.5,0.17, −2.2)	188.8	–	–	–	–
	5p	−2.8(−2.5, −0.17, −1.3)	136.2	–	–	–	–
Average value		−2.8(−2.3,0, −1.6)	153.0	–	–	–	–
Standard deviation		0.9	34.6	–	–	–	–
	1l	−2.3(0, −2.1, −1)	45.1–122.1	−2.5	−2.6(0, −2.3, −1.1)	−0.7(0, −0.6, −0.3)	−3.8
	2l	2.8(1.9, −1.3,1.7)	32–192	6	1.3(0.9, −0.6,0.8)	7.1(4.8, −3.2,4.2)	8.8
Liver	3l	−2(-0.7, −1.1, −1.6)	39–205.9	−3	−2.8(−0.9, −1.5, −2.2)	−0.9(−0.3, −0.5, −0.7)	−4.1
	4l	1.4(0,1.2,0.8)	15 –138	3	−0.8(0, −0.7, −0.4)	0.6(0,0.5,0.3)	4.1
	5l	−1.6(0.5,1.3, −0.7)	15.2–140.8	−1	−1(0.3, −0.8, −0.5)	1(−0.3,0.8,0.5)	−1.4
Average value		−0.3(0.3, −0.9, −0.17)	94.5	0.5	−1.2(0.1, −1.2, −0.7)	1.4(0.8, −0.6,0.8)	1.9
Standard deviation		2.3	21.2	3.9	1.7	3.3	5.8
	1b	−0.8(−0.4, −0.6, −0.4)	27.5	–	–	–	–
	2b	−1.3(0, −1.3, −0.3)	23.9	–	–	–	–
Breast	3b	−1.1(0.4, −1, −0.3)	21.4	–	–	–	–
	4b	−1.3(0, −1.2, −0.5)	23.2	–	–	–	–
	5b	−0.13(0, 0, −0.13)	12.9	–	–	–	–
Average value		−0.9(0, −0.8, 0.3)	21.8	–	–	–	–
Standard deviation		0.5	5.4	–	–	–	–

Liver scans showed shifts in both directions away and towards the US probe for the whole organ ROI. The shift direction depends on the relative importance of overlying fat tissue with respect to liver parenchyma along the beam's path, since they have quite different SOS values and on the opposite sides of 1540 m/s. The shifts undergone by the small dummy structures in the shallow and deep positions inside the liver are as large as 7 mm, which may be significant for e.g. US-guided stereotactic radiotherapy of liver lesions, where small beam margins may be employed. Scanning paths were always through a fat layer whose thickness was the key element to determine the behaviour of the aberration inside the liver (high SOS value, 1595 m/s[9]). In the case of a thin fat layer overlying the liver, the deviation from the assumed SOS of 1540 m/s inside the liver dominates, resulting in a shallower apparent depth of the whole organ.

The correction moves structures in the liver to larger depths up to 2.8 cm. The opposite happens when a thick fat layer is present, since fat has a SOS value which is lower than the reference assumed value of 1540 m/s, while liver tissue is higher. For the same reason, a very shallow ROI when a thick fat tissue is present will appear deeper than it really is, and a deep ROI will exhibit little or no aberration due to compensation from liver tissue. When the fat layer is thin, the shallow ROI does not undergo a significant change in apparent depth, while the deep ROI will appear shallower according to the amount of liver tissue traversed by the US beam. After the correction, the shifts obtained are reported in Table 1. Another interesting effect of SOS aberration in liver is due to the different shifts undergone by the proximal and the distal boundaries, which can be in the same direction with different values or in opposite directions, that produce a deformation of the organ shape, with a corresponding variation of its apparent volume in the US scan of up to about 9% (Table 1).

The five breast cancer patients showed in the original US images an apparent depth of the seroma volumes larger than the real one due to a SOS in breast tissue below 1540 m/s (the reported mean value is 1510 m/s but can be much lower, down to 1450 m/s, according to fat content[9]). So after the application of the SOS correction, the centroids underwent a shift towards the skin of up to 1.3 millimeters (Table 1). The shifts are small because for all five cases the targets were shallow. No significant apparent volume changes were observed. In our limited study, a systematic correction based on co-registered CT scans does not seem necessary. But for larger breasts with deeper targets than the ones seen in our study, the difference between the real and the apparent position may be more significant. The presence of tissues with SOS lower than the assumed one between the probe and the target allows for simpler correction strategies, to find a better average SOS value or to partially take different SOS values into account (see for example[18] or[19]), approaches already implemented by some manufacturers (for example, Philips iU22 xMATRIX ultrasound system, Koninklijke Philips Electronics N.V. Amsterdam, The Netherlands).

This study was aimed at applying a previously described SOS aberration correction algorithm for 3D US images[11] to clinical cases. The better accuracy in structure position definition after correction was previously assessed comparing corrected US scans of phantoms with the co-registered CT scans[11]. A complete study of the impact of SOS aberration with respect to the different possible clinical workflows is outside the scope of this work and will be performed separately. Nevertheless it is important to note that when this correction is applied at the treatment stage, for the CT image that is used to base the SOS correction on to be valid, it should be representative for the patient geometry on the treatment day.

The purpose of this work was to show that the SOS aberration can be important and in principle unpredictable for some cases (like liver), and five patients per type were sufficient to find evidence for this. A solution was already proposed previously[11], so it was not the aim of this article to derive a class solution based on statistical data,

but to issue a warning to US operators in radiotherapy. Adding more patients would not change the results obtained substantially, in particular that the SOS aberration is a real effect noticeable in clinical practice. For prostate the SOS correction is always s the abdominal US probe while for liver the correction can go in both directions towards and away from the US probe.

4.4 Conclusion

In radiotherapy quantitative imaging is used to guide accurate treatments with narrow treatment margins. Aberrations in US imaging can produce potential errors in positioning of targets, contouring structures and dose planning accuracy. We presented here an evaluation of the magnitude of the SOS aberration in various anatomical sites where US imaging could be used as a guidance tool. Prostate and liver cases showed shifts up to several mm due to SOS aberrations, which cannot be corrected generically a priori because of the unpredictable overlying tissue layer thicknesses in individual cases, and would potentially benefit from the proposed SOS correction. Breast cases showed that a shallow target in a uniform tissue undergoes small shifts. The obtained shifts have to be put into perspective with regard to beam margins to assess their dosimetric importance. A detailed study on the impact of the SOS artefact on the clinical workflow of US-based image guidance in radiotherapy will be reported next.

Aknowledgements
The authors wish to thank all staff involved in collecting the 3D US datasets at MAASTRO Clinic and the Jewish General Hospital. Resonant Medical (Elekta) is thanked for support and discussion.

4.5 References

1. C. X. Yu, C. J. Amies and M. Svatos, "Planning and delivery of intensity-modulated radiation therapy," Med Phys **35**, 5233-5241 (2008).
2. C. C. Ling, E. Yorke and Z. Fuks, "From IMRT to IGRT: frontierland or neverland?," Radiother Oncol **78**, 119-122 (2006).
3. W. Wein, B. Roper and N. Navab, "Integrating diagnostic B-mode ultrasonography into CT-based radiation treatment planning," IEEE Trans Med Imaging **26**, 866-879 (2007).
4. D. J. Fraser, Y. Chen, E. Poon, F. L. Cury, T. Falco and F. Verhaegen, "Dosimetric consequences of misalignment and realignment in prostate 3DCRT using intramodality ultrasound image guidance," Med Phys **37**, 2787-2795 (2010).
5. T. S. Berrang, P. T. Truong, C. Popescu, L. Drever, H. A. Kader, M. L. Hilts, T. Mitchell, S. Y. Soh, L. Sands, S. Silver and I. A. Olivotto, "3D ultrasound can contribute to planning CT to define the target for partial breast radiotherapy," Int J Radiat Oncol Biol Phys **73**, 375-383 (2009).
6. D. J. Fraser, P. Wong, K. Sultanem and F. Verhaegen, "Dosimetric evolution of the breast electron boost target using 3D ultrasound imaging," Radiother Oncol **96**, 185-191 (2010).
7. D. Fraser, P. Fava, F. Cury, T. Vuong, T. Falco and F. Verhaegen, 2007 (unpublished).
8. L. Xing, B. Thorndyke, E. Schreibmann, Y. Yang, T. F. Li, G. Y. Kim, G. Luxton and A. Koong, "Overview of image-guided radiation therapy," Med Dosim **31**, 91-112 (2006).
9. T. D. Mast, "Empirical relationships between acoustic parameters in human soft tissues," Acoustics Research Letters Online **1**, 37-42 (2000).
10. P. L. Carson, "Biomedical ultrasonics. By P.N.T. Wells, Ph.D., Academic Press, Inc. London, Copyright 1977. 635 pages. $46.90," Journal of Clinical Ultrasound **6**, 126-127 (1978).
11. D. Fontanarosa, S. van der Meer, E. Harris and F. Verhaegen, "A CT based correction method for speed of sound aberration for ultrasound based image guided radiotherapy," Med Phys **38**, 2665-2673 (2011).
12. F. Van den Heuvel, T. Powell, E. Seppi, P. Littrupp, M. Khan, Y. Wang and J. D. Forman, "Independent verification of ultrasound based image-guided radiation treatment, using electronic portal imaging and implanted gold markers," Med Phys **30**, 2878-2887 (2003).
13. S. v. d. M. Esther Bloemen-van Gurp, Peter Visser et al. , presented at the AAPM meeting, Vancouver, 2011. (unpublished).
14. C. Peng, K. Kainz, C. Lawton and X. A. Li, "A Comparison of daily megavoltage CT and ultrasound image guided radiation therapy for prostate cancer," Medical Physics **35**, 5619 (2008).
15. T. J. Scarbrough, N. M. Golden, J. Y. Ting, C. D. Fuller, A. Wong, P. A. Kupelian and C. R. Thomas, Jr., "Comparison of ultrasound and implanted seed marker prostate localization methods: Implications for image-guided radiotherapy," Int J Radiat Oncol Biol Phys **65**, 378-387 (2006).
16. H. Johnston, M. Hilts, W. Beckham and E. Berthelet, "3D ultrasound for prostate localization in radiation therapy: a comparison with implanted fiducial markers," Med Phys **35**, 2403-2413 (2008).
17. P. K. Verma, V. F. Humphrey and F. A. Duck, "Broadband measurements of the frequency dependence of attenuation coefficient and velocity in amniotic fluid, urine and human serum albumin solutions," Ultrasound in Medicine & Biology **31**, 1375-1381 (2005).
18. D. Napolitano, C.-H. Chou, G. McLaughlin, T.-L. Ji, L. Mo, D. DeBusschere and R. Steins, "Sound speed correction in ultrasound imaging," Ultrasonics **44**, e43-e46 (2006).
19. J. F. Greenleaf, "Tissue Characterization With Ultrasound and its application," CRC Press (1986).

Chapter 5

On the significance of density-induced speed of sound variations on US-guided radiotherapy

Davide Fontanarosa
Skadi van der Meer
Frank Verhaegen

Published in: Medical Physics 39(10):6316-6323, 2012.

Abstract

Purpose

To show the effect of speed of sound (SOS) aberration on ultrasound guided radiotherapy (US-gRT) as a function of implemented workflow. US systems assume that SOS is constant in human soft tissues (at a value of 1540 m/s), while its actual non-uniform distribution produces small but systematic errors of up to a few millimeters in the positions of scanned structures. When a co-registered computerized tomography (CT) scan is available, the US image can be corrected for SOS aberration. Typically image guided radiotherapy (IGRT) workflows implementing US systems only provide a CT scan at the simulation (SIM) stage. If changes occur in geometry or density distribution between SIM and treatment (TX) stage, SOS aberration can change accordingly, with a final impact on the measured position of structures which is dependent on the workflow adopted.

Methods

Four basic scenarios were considered of possible changes between SIM and TX:

1) No changes.
2) Only patient position changes (rigid rotation-translation).
3) Only US transducer position changes (constrained on patient's surface).
4) Patient tissues thickness changes.

Different SOS aberrations may arise from the different scenarios, according to the specific US-gRT workflow used: inter-modality (INTER) where TX US scans are compared to SIM CT scans; intra-modality (INTRA) where TX US scans are compared to SIM US scans; and INTERc and INTRAc where all US images are corrected for SOS aberration (using density information provided by SIM CT). For an experimental proof of principle, the effect of tissues thickness change was simulated in the different workflows: a dual layered phantom was filled with layers of sunflower oil (SOS 1478 m/s), water (SOS 1482 m/s) and 20% saline solution (SOS 1700 m/s). The phantom was US scanned, the layer thicknesses were increased and the US scans were repeated. The errors resulting from the different workflows were compared.

Results

Theoretical considerations show that workflows implementing SOS correction based on SIM-CT scan (INTERc, INTRAc) give null errors in all scenarios except when tissues thickness changes, where an error proportional to the degree of change in SOS maps between SIM and TX (□SOS) occurs. An uncorrected workflow such as INTER produces in all scenarios a pure SOS error, while uncorrected INTRA produces a null error for rotation-translation of the patient, a □SOS error for changing tissues thickness and an error proportional to the degree of SOS distribution change along the different lines of view (LOVs) when shifting the transducer. The dual layered phantom demonstrated

experimentally that the effect of SOS change between SIM and TX is clinically non relevant, being less than the intrinsic resolution of imaging systems, even when a substantial change in thicknesses is applied, provided that a SIM-CT-based SOS aberration correction is applied. Non-corrected workflows produce errors up to 4 mm for INTER and to 3 mm for INTRA in the phantom test.

Conclusions

A SOS correction is advantageous for all US-gRT workflows and clinical cases, where the effect of SOS change can be considered a second order effect.

5.1 Introduction

Ultrasound (US) imaging, a traditionally qualitative diagnostic method, has recently also become an interesting tool in quantitative measurements and has gained importance in the field of radiotherapy (RT) (1-9). Its applications in Image Guided Radiation Therapy (IGRT) (10) and in organ segmentation (11-14) are growing as it potentially provides a reliable cost-effective imaging technique which, among other advantages, does not deliver unwanted radiation dose to the patient. The application of US imaging techniques to IGRT (US-gRT) can have two different approaches:

1) an intermodality (INTER) workflow where US images acquired at the time of treatment (TX) are compared to a reference simulation (SIM) CT image (15-17);

2) an intramodality (INTRA) workflow where TX US images are compared to a reference US image acquired at SIM and co-registered in absolute coordinates to it (18).

In both workflows there is a comparison between images acquired at different times, at SIM and at TX. The purpose is to assess if anything has changed in the patient geometry and, if needed, attempt to correct for it to irradiate the target in the same position at TX as it was at SIM. Changes may occur if e.g. the patient is in a different position, has lost weight, or has different organ fillings.

When these changes occur, it is necessary to take into account another effect: the tissue distribution in space has changed. A tissue property empirically related to the mass density is the speed of sound (SOS) (19), which implies that if something changes between SIM and TX, then also the SOS distribution changes. A well known aberration of US imaging is related to SOS (20): sound waves travel at different speeds in different media and these differences can be rather important, ranging in human soft tissues at body temperature (37°C) from 1475 m/s in fat to 1613 m/s in connective tissue (19). The standard practice in US imaging is to assume a fixed value for the SOS of 1540 m/s (21), which leads to errors of up to 6% in SOS and, therefore, distance. The assumption of a constant SOS was made since real-time correction of SOS aberrations for individual tissue types was not practically feasible and since, until recently, US techniques were mainly used in qualitative diagnostic imaging. The SOS aberration accumulates along the lines of view (LOV) of the US transducer and therefore depends on the SOS distribution. So, a change reported by the US system at TX can be due to the combination of a possible real shift and an apparent one due to the variation of SOS distributions with respect to SIM (Fig. 1). These shifts may combine to increase or decrease the final error depending on the specific change which occurred. In the example in Fig. 1 they reinforce each other in a worst case scenario where SOS errors occurred. Different workflows will lead to different apparent shifts, according to how the SOS aberrations combine at SIM and TX, and this might partially explain the discrepancies reported in the literature between INTER and INTRA (22).

An algorithm was introduced to correct for SOS aberration in RT applications (23), which uses the density distribution provided by the co-registered CT scan to create a SOS map of the patient at SIM. No US-gRT workflow provides co-registered CT scans (or equivalent sources of density distributions) at TX, at least not for each treatment fraction (this would nullify most of the benefits derived from US-gRT). The purpose of this work is to investigate how the patient changes which may occur between SIM and TX affect the SOS aberration and, in particular, if a correction based on a CT taken at SIM (SIM-CT) is valid also for US images taken at TX (TX-US) for the different workflows.

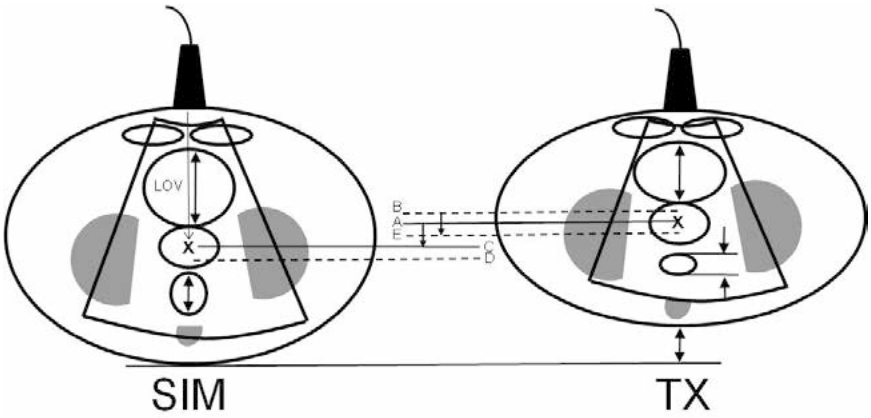

Fig. 1: A simulated worst case scenario of a SOS distribution variation between SIM and TX in a prostate cancer case: the variation (plotted as a change in tissue thicknesses, indicated by the arrows showing how the organs and the whole patient shrink between SIM and TX) changes the SOS average value along the LOV (thin arrow) to the target (indicated by the cross). The worst case scenario assumption is that this value switches from higher to lower than 1540 m/s. US-TX reports the position of the target (the prostate) at depth A. Due to SOS aberration at TX, the real position is B, shallower than A; but the shift applied to the patient is from A to C, which is the position of the prostate as seen by the reference image at SIM. Its real position at SIM was D (which we are trying to reproduce at TX), now deeper than C because of the change in SOS mean value along the LOV on the opposite side of 1540 m/s. So the real target will be after the shift at E, whose distance from the TX position A is the sum of the real shift (A to C) and the SOS aberration at TX (A to B), while it should be in D. So the final error would be the shift E to D. The arrow connecting line A-C shows the performed apparent shift; the arrow connecting line B-E shows the real shift.

5.2 Materials & Methods

Workflows

Two clinically available workflows were examined: INTER, implemented in systems like BAT (BAT system, Nomos, Sewickley, PA); and INTRA, implemented in the Clarity system (Elekta, Stockholm, Sweden). In the former, the TX-US is compared to the SIM-CT and the differences in structure positions are an indication of a possible need for a

patient position correction. In the latter, at SIM a SIM-CT and an US scan (SIM-US) are performed; at TX the TX-US is compared to the SIM-US and the differences in structure positions are translated into couch position shifts. The previously introduced SOS correction algorithm (23) is here applied to all US images using the density information provided by the SIM-CT. The two resulting workflows where the correction was so implemented will be named INTERc and INTRAc respectively. So in summary the four possible workflows considered were: INTER, INTRA, INTERc and INTRAc.

Scenarios

To investigate how a change in a patient can affect the final outcome of the comparison between SIM and TX, four basic scenarios were considered to decompose the problem in its simplest components which, combined, can account for most changes:

A) No changes: SIM and TX coincide. No corrections to patient setup needed
B) Only patient position changes (rigid rotation-translation): in this scenario, the patient only undergoes a rotation-translation but no internal organ motion relative to the transducer position. Nor do changes in structure thicknesses occur (Fig 2a).
C) Only US probe position changes (constrained on patient's surface): in this scenario, nothing changes with respect to the patient, but the US transducer scans the tissues from a different point on the patient's skin, so the LOVs are different (Fig 2b).
D) A change in tissues thickness and relative position of structures occurs, with the US transducer constrained on the skin but without any change in scanning angle, such that along each LOV the tissues traversed are the same but relative lengths change (Fig 2c).

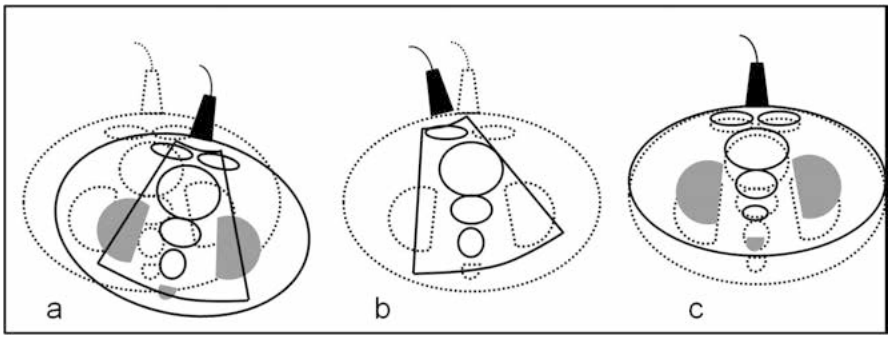

Fig. 2: The scenarios with possible changes between SIM and TX are plotted. The dashed line drawings refer to SIM, the solid ones to TX. In **Fig 2.a** the patient undergoes a rotation and a translation. In **Fig 2.b** the patient position does not change, but the transducer scans the tissues from a different entry angle on the skin. In **Fig 2.c** internal motion and changes in tissue thickness occur, so internal structures are not in the same relative position anymore.

Phantom measurements

To provide an experimental validation, US and CT images were acquired of a poly methyl methacrylate (PMMA) phantom (dimensions 15 cm length, 15 cm depth, 13.5 cm height) filled with two layers of liquids. The phantom was scanned in two configurations with different layer thicknesses to simulate a change in tissues between SIM and TX, and the position of the bottom surface was considered. The configurations used are reported in Table 1, and the experimental setup in Fig. 3.

Table 1: Measurements of thicknesses of the two liquid layers in the PMMA phantom according to CT and US scans. The phantom is initially filled with approximately 4 cm of sunflower oil on top and 1 cm of water or 20% saline solution below it to simulate the SIM situation; then the thicknesses are increased to approximately 5 cm and 2 cm respectively (TX1) to simulate a change in the patient between SIM and TX. Both measurements performed on co-registered CT scans and US scans are reported. The measured differences in depths between CT and US scans match the expected values according to the calculated distance error in US, where SOS aberration is present, proportional to the ratio between the assumed SOS value of 1540 and the real value (23). Also an extreme variation where the sunflower oil layer is increased to approximately 6 cm (TX2) was performed for the combination with water. On the right side is drawn a schematic plot of the layer thicknesses in the phantom.

		Depths (mm)		Depths (mm)		
		Sunflower oil	Water	Sunflower oil	20% saline solution	
SIM	CT	41	10	40	11	 4 1
	US	42	10	40	9	
TX1	CT	52	19	50	21	 5 2
	US	54	20	53	19	
TX2	CT	58	22			 6 2
	US	60	24			

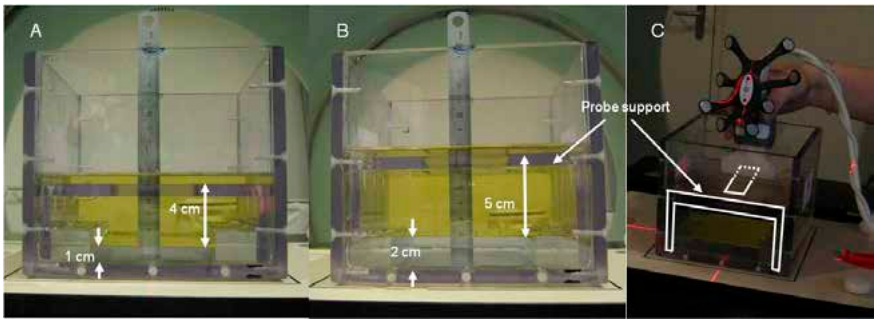

Fig. 3: Experimental setup: (A) the PMMA phantom filled with approximately 4 cm of sunflower oil overlying 1 cm of 20% saline solution; (B) the layer thicknesses are increased to approximately 5 cm and 2 cm respectively (the exact values are reported in Table 1); (C) the measurement is performed using a Clarity linear probe on the PMMA support: the transducer is positioned and rocked around the contact points to span the US volume. The shape of the support is drawn to show the aperture through which the probe, positioned on the support, scanned the liquids.

The US scans were performed using the linear US probe provided with the Clarity system (type L14–5/38, center frequency 7.2 MHz, Sonix Series, Ultrasonix Medical Corporation, Richmond, BC, Canada), and an in-house manufactured support in PMMA was used to ensure repositioning accuracy (Fig. 3C). The CT scans were performed with a Siemens Somatom scanner (SOMATOM Sensation Open, Syngo CT 2006A, Siemens, Germany). The liquids used were sunflower oil (SOS value at 20 °C: 1478 m/s (24)), 20% saline solution (SOS value at 20 °C: 1700 m/s (25)) and water (SOS value at 20C: 1482 m/s (26)). The top layer was always oil and the bottom layer was either water or a saline solution. Changing the liquid thicknesses simulates tissue thicknesses change. The latter from a SOS aberration point of view is identical to thickness change but it is not when a correction strategy needs to be devised, since the LOV for the first case does not change while in the second it does. In the latter case a simple 1D correction does not suffice, but a more complex correction taking angled LOV into account in a 3D space is required. This experiment also simulates internal organ motions, like prostate rotation, where no actual thickness changes occur but tissue replacements in the field of view (FOV) produce the same results in terms of SOS aberration. The four workflows corresponding to the scenario D) were simulated, where the variation in liquid levels simulate a change in thickness of layers of tissues with different SOS values. First we simulated the INTER approach, where a direct comparison between the TX-US and the SIM-CT was used to align the bottom surface of the phantom according to the two imaging modalities (Fig. 4.A); then the INTRA approach, where the TX-US scan was compared to the SIM-US scan (Fig. 4.B); then the corrected workflows, INTERc and INTRAc, where all US images were corrected for SOS aberrations.

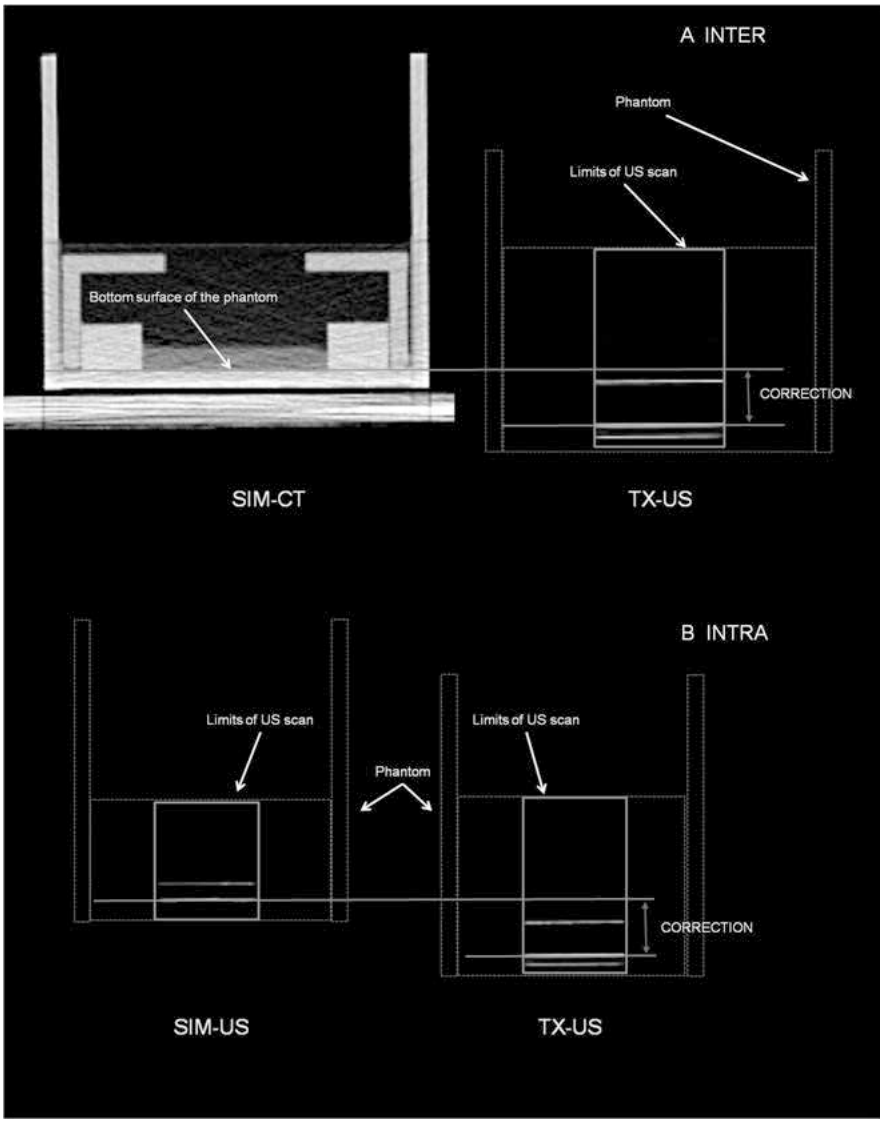

Fig. 4: INTER (A) and INTRA (B) approaches applied to PMMA phantom measurements. On the left are the SIM images to which the TX images, on the right, are compared. For INTER the comparison is performed by aligning the bottom surface of the phantom on TX-US and on SIM-CT. For INTRA the comparison is performed with the SIM-US. Apparent errors are exaggerated for clarity.

δSOS and ΔSOS

A key role is played in this study by the SOS distribution change between SIM and TX. At SIM the SOS aberration alters perceived distances according to the ratio between the reference SOS value of c_{REF} = 1540 m/s and the local true SOS value, so the depth of a voxel at $d_{US,SIM}$ according to the US system will in reality be at:

$$d_{SIM} = \frac{1}{c_{REF}} \int_{LOV_{SIM}}^{d_{US,SIM}} c_{SIM}(x)dx \tag{5.1}$$

where d_{SIM} is the real distance, c_{SIM} is the local SOS value at depth x and LOV_{SIM} is the LOV of the US system at SIM.
The same equation can be used at TX:

$$d_{TX} = \frac{1}{c_{REF}} \int_{LOV_{TX}}^{d_{US,TX}} c_{TX}(x)dx \tag{5.2}$$

where now the same quantities are referred to TX. If the same voxel on the US scans at SIM and TX is considered, $d_{US,SIM} = d_{US,TX} = d_{US}$ and from Eq. 5.1 and Eq. 5.2 the following relation can be derived:

$$d_{TX} = \frac{\int_{LOV_{TX}} c_{TX}(x)dx}{\int_{LOV_{SIM}} c_{SIM}(x)dx} d_{SIM} \equiv \delta SOS \cdot d_{SIM} \tag{5.3}$$

where δSOS is a factor quantifying the importance of SOS maps changing between SIM and TX, because the more this factor deviates from unity the larger will be the difference between the positions of the corrected distances at the two stages.
If the LOVs at the two stages coincide, Eq. 5.3 can be rewritten as follows:

$$d_{TX} = \int_{LOV} \frac{c_{TX}(x)}{c_{SIM}(x)} dx \cdot d_{SIM} \equiv \int_{LOV} \underline{\Delta}SOS(x)dx \cdot d_{SIM} \tag{5.4}$$

Discretizing the problem on a voxel by voxel basis, $\underline{\Delta}$SOS is a matrix very similar to ΔSOS (defined in (23) as the ratio between the local SOS value and the reference value), with the difference that ΔSOS is a ratio between a heterogeneous SOS distribution and a homogeneous one with constant value 1540 m/s, while for $\underline{\Delta}$SOS the variation is between two potentially highly heterogeneous matrices: ΔSOS at SIM, ΔSOS_{SIM}, and at TX, ΔSOS_{TX}. In principle, the $\underline{\Delta}$SOS map can have voxel values as high (and even higher) as ΔSOS, because when a tissue is replaced by one with a SOS value significant-

ly different the ratio between the voxel values at TX and SIM can be as large as the ratio between the voxel values at SIM and 1540 m/s. In extreme situations, when the tissue replacement occurs between tissues with SOS values where one has an SOS value above and the other one below the reference value of 1540 m/s, $\underline{\Delta}$SOS can have voxel values higher than ΔSOS_{SIM}, which means the effect of changes between SIM and TX can be worse than the pure SOS aberration effect on SIM images. This also means that potentially major changes between SIM and TX would invalidate the use of SIM-CT to correct TX-US.

5.3 Results

Clinical scenarios and workflows

Scenarios and workflows can be combined to show the results in terms of SOS aberrations. Also different scenarios can be combined together, but to investigate the outcome of such combinations is outside the scope of this work.
The following are the possible outcomes, where the letter A-D refers to the scenario (as described in paragraph II.B) and the number 1-4 refers to the workflow implemented (Table 2):

- **A-1**: At TX an apparent shift can be detected between the SIM-CT and the TX-US due to SOS aberration on TX-US image. Since this error is only due to SOS map at TX, in Table 2 it is named SOS_{TX}.
- **A-2**: The same SOS error is present twice, at SIM and TX, since in principle US images of the same patient are compared and exactly the same SOS aberrations will occur. So there is a null error.
- **A-3**: Null error: the SOS aberration is corrected using correct density information, since no changes occurred between SIM and TX.
- **A-4**: Null error, as A-3.
- **B-1**: The shift detected between structure positions at TX with respect to SIM is the combination of the real position change and of the SOS aberration along the LOV along which the US scan was performed at TX. So an overcorrection of magnitude equal to the SOS aberration will occur (in principle at TX, but here we assume no changes happen in the patient so the SOS aberrations at SIM and TX coincide). SOS_{TX} error.
- **B-2**: The patient is scanned along two LOVs at SIM and TX which are different in absolute coordinates, but are exactly the same with respect to the patient. So the SOS aberration will affect the US image exactly in the same way, and the final shift reported at TX is the correct shift the patient undergone. So after the repositioning, the outcome is as A-2: null error.

Table 2: For all the workflows considered, non corrected (INTER and INTRA) and corrected (INTERc and INTRAc), the effect of density change between SIM and TX in the different scenarios is reported with respect to SOS aberration: SOS_{TX} is a pure SOS aberration error due to the SOS distribution at TX; δSOS is the effect of SOS distribution change in its most general definition, in particular here it takes into account the change of LOV of the US transducer between SIM and TX; $\underline{\Delta}$SOS is as δSOS with the assumption that the LOV does not change. SOS_{TX}, δSOS and $\underline{\Delta}$SOS are the different types of errors and do not indicate their magnitude.

			Workflows			
			INTER	INTRA	INTERc	INTRAc
			1	2	3	4
Scenarios	No change	A	SOS_{TX}	0	0	0
	Roto-transl	B	SOS_{TX}	0	0	0
	Probe position	C	SOS_{TX}	δSOS	0	0
	Thickness	D	SOS_{TX}	$\underline{\Delta}$SOS	$\underline{\Delta}$SOS	$\underline{\Delta}$SOS

- **B-3**: The error in structure positions at TX is the sum of the real displacement and the SOS error. So if the matching between structures at SIM and TX is restored, there will be still an error equal to the SOS aberration. A possible correction strategy here would be to calculate the SOS aberration error using the correction algorithm (23) and subtract this value to the shift applied to the TX-US image. So the final outcome would be null error.
- **B-4**: SOS aberration correction is initially applied to SIM-US, so the final positions for structures will match the ones reported by SIM-CT. So the workflow will be as B-3 and the result again null error.
- **C-1**: In this case, only one FOV is present, the one seen by TX-US. So a pure SOS error accumulates along it, which results in an apparent positioning error leading to overcorrection: SOS_{TX} error.
- **C-2**: In this case, SIM-US and TX-US have different FOVs. So the SOS aberration will accumulate differently at SIM and TX. In this case the SOS map variation is strictly speaking null ($\underline{\Delta}$SOS = 1), because the density distribution in the patient does not change. But the patient is scanned through a different SOS distribution, at SIM and TX and the effect of this difference is the same as changing tissues along the LOVs. In this case the LOVs do not coincide so the error is due to δSOS (see EQ. 5.3).
- **C-3**: As in C-1, only one FOV and, provided the SIM-CT dataset can be used properly (which means along the new FOV in 3D space, thus using a 3D correction algorithm), the correction should restore the structures in their correct position. Null error.
- **C-4**: Since SIM-US can be properly corrected with SIM-CT, this case is as C-3. Null error.

- **D-1**: In this case, there is a real internal relative motion of structures, due to tissues thicknesses change and SOS aberration at TX. So after the shift, the SOS aberration due to tissue distribution at TX is still present. SOS_{TX} error.
- **D-2**: An error is introduced between SIM and TX because relative path lengths in tissues are different: thus also SOS aberration in principle will be different, creating a $\underline{\Delta}$SOS error.
- **D-3**: When correcting the TX-US, where there are the real shift and the SOS aberration at TX, with SIM-CT one introduces an error due to the change in SOS maps between SIM and TX, the $\underline{\Delta}$SOS error.
- **D-4**: Comparing the corrected SIM-US with the corrected (with SIM-CT) TX-US, also in this case a $\underline{\Delta}$SOS error is introduced, as in D-3.

Phantom measurements for scenario D

The third column of Table 3A reports the differences between the positions of the bottom surface of the phantom measured by the TX-US and the SIM-CT. The fourth column shows the real shifts due to the change in thickness (resulting from the comparison between TX-CT and SIM-CT). The fifth column lists the differences between the two, corresponding to the errors obtained when the workflow 1 (INTER) is applied. The errors are larger when both liquids have SOS values lower (or higher) than the assumed value of 1540 m/s, so in this case for the combination of sunflower oil and water errors up to 4 mm are obtained. When instead the SOS values for the two layers are on the opposite sides of 1540 m/s, like for the case of sunflower oil and 20% saline solution, the SOS aberration is partially compensated and the final error is limited to 1 mm.

Workflow 2 (INTRA) gives better results, reported in Table 3B. Here the apparent shifts result from the comparison between the position of the bottom surface of the phantom in the TX-US and the SIM-US. The real shifts as before are derived from the CT scans, and the errors are the differences between the two. When a correction was applied to the INTER approach (workflow 3, INTERc), the shifts reported in Table 3A were applied to the TX-US of the phantom producing an over-correction of the positioning error, since the shifts are the sum of the real shift plus the SOS aberration. The image was then corrected using the SIM-CT density information and the correction was subtracted from the original shifts to compensate for the initial overcorrection. The final shifts derived are reported in the first column of Table 3C, along with the real shifts and the errors produced.

A similar procedure was followed for INTRA (workflow 4, INTRAc): the main difference is that here the correction was first applied to the SIM-US, thus restoring a matching image with SIM-CT.

		Apparent shift	Real shift	Error	Calculated error
			INTER		
Oil/water	TX (5-2) -> SIM (4-1)	23	20	3	3.0
	TX (6-2) -> SIM (4-1)	33	29	4	3.5
Oil/20% sal sol	TX (5-2) -> SIM (4-1)	21	20	1	0.5
			INTRA		
Oil/water	TX (5-2) -> SIM (4-1)	22	20	2	2.0
	TX (6-2) -> SIM (4-1)	32	29	3	2.5
Oil/20% sal sol	TX (5-2) -> SIM (4-1)	23	20	3	2.5
			INTERc		
Oil/water	TX (5-2) -> SIM (4-1)	21	20	1	0.0
	TX (6-2) -> SIM (4-1)	31	29	2	1.0
Oil/20% sal sol	TX (5-2) -> SIM (4-1)	19	20	1	1.0
			INTRAc		
Oil/water	TX (5-2) -> SIM (4-1)	20	20	0	1.0
	TX (6-2) -> SIM (4-1)	30	29	1	1.5
Oil/20% sal sol	TX (5-2) -> SIM (4-1)	21	20	1	0.5

Table 3: In the third column of the table, "Apparent shift", the differences are presented between the positions of the bottom surface of the phantom from the TX-US and the positions according to the SIM-CT (for INTER) and to the SIM-US (for INTRA). The same differences are also shown for the corrected workflows, INTERc and INTRAc; in the fourth column the real shifts are given due to the change in layer thickness (resulting from the comparison between TX-CT and SIM-CT); in the fifth column the differences between real and apparent position are given; and in the sixth column the expected calculated errors according to the thickness of liquids and their SOS values are reported for a direct comparison: the values are always in good agreement and within the experimental error (the CT scan resolution of 1 mm).

5.4 Discussion

We recently published an algorithm (23) aimed at correcting SOS aberrations in US images during US-gRT. A concern related to the use of this algorithm is how a correction based on density information provided at SIM is affected by density changes occurring between SIM and TX, in particular as a function of the specific US-gRT workflow used. Our work indicates that, while the SOS correction itself may be significant (27), the effect of the change in the SOS map between SIM and TX is a second order effect in most clinical applications. This is because after the application of the correction based on SIM density information on TX images the residual error is smaller or comparable to the intrinsic resolution of the images (typically around 1 mm for co-registered US and CT scans in the axially projected plane). This is due to relative path length changes from SIM to TX, but in general tissues along the majority of the path do not change and only variations at interfaces occur, usually of small magnitude. In cases where this assumption is not valid or if particularly unlucky cases occur (like a tissue substitution with large change in SOS, which is very unlikely for large volumes) a re-planning of the patient is most probably required anyway because in the presence of such large changes the dose needs to be re-calculated before the plan can be delivered. It is nevertheless interesting to note that the spatial replacement of one tissue with another between SIM and TX produces a change in the apparent depths proportional to the ratio between the relative SOS values. In fact, as seen from (Eq. 5.4), the following equation can be applied (if only the region where the replacement has happened is considered):

$$d_{TX} = \frac{c_{SIM}}{c_{TX}} d_{SIM} = \underline{\Delta}\mathrm{SOS} \cdot d_{SIM} \tag{5.5}$$

So in principle a significant difference in apparent depths due to $\underline{\Delta}$SOS can occur, and this difference becomes increasingly more important the more the local SOS values differ between SIM and TX. When the spatial substitution of tissues implies a change of SOS values from higher to lower (or vice versa) than 1540 m/s, one particular case is created in which the apparent shifts produced are worse in the INTRA than the INTER workflow (Fig. 5). So, in general, errors due to $\underline{\Delta}$SOS might reach values comparable or larger than regular SOS aberrations, but will only very rarely result in shifts of entire structures.

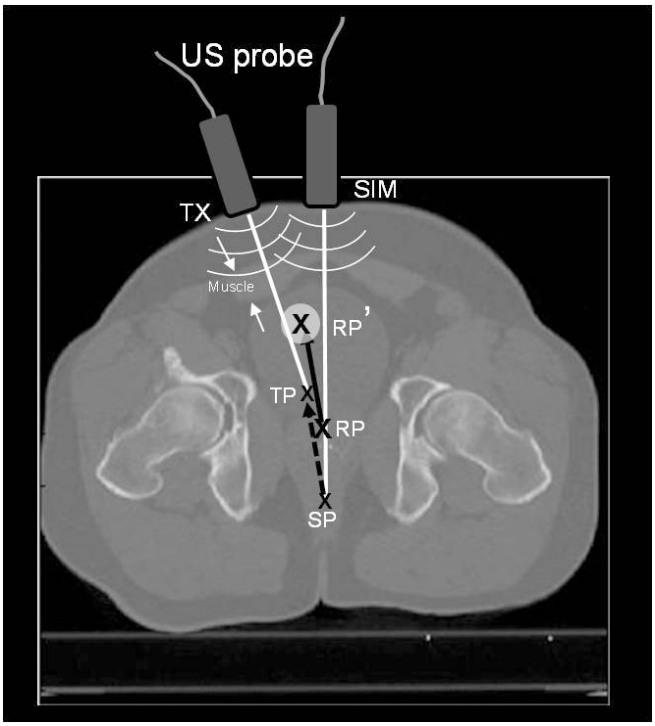

Fig. 5: An example of how a simulated extreme change in transducer position can result in a possible wrong patient shift, due to SOS corrections in opposite directions. The real position of the target is RP (15 cm along the SIM LOV), but at SIM it is shown at SP (15.46 cm, along SIM LOV) due to SOS aberration. At TX the SOS aberration is accumulated along a different LOV, because the probe is in a different location, so the target is at TP (14.93 cm along the TX LOV, shallower due to the increased amount of muscle tissue along the LOV) on the TX US scan. A shift of the structure between SP and TP seems then required (dashed arrow) to restore the SIM position, but this apparent shift in reality displaces the target by about 5 mm (indicated by the solid arrow) from RP to RP'. The shift is exaggerated for display purposes in the image.

In our phantom experiments, we tested the SOS algorithm robustness by introducing large changes in layer thicknesses. For the transducer it is very likely that a significant misplacement, resulting in scanning from a different skin position, is recognized when the scan is performed, and that a corrected rescan would be performed. We also used extreme SOS values (like 20% saline solution, with 1700 m/s, on the very upper limit of human soft tissues SOS values) to produce worst case scenarios to allow reasonable conclusions to be drawn on clinical cases where direct comparisons are more complex than with phantoms. In fact, besides of course the impossibility of making direct SOS aberration-free measurements of distances *in vivo*, also the comparison with other imaging modalities, e.g. CT scans, is not easy due to the intrinsic different nature of the CT and US images. For example, the urine and the bladder walls are nearly indistinguishable on a CT scan, because of their nearly identical electron densities. On the

other hand, the highly non-echogenic nature of liquids with respect to the scattering properties of solid tissues creates a clear contrast on US images. So in general it is not trivial which interfaces should be matched in the two imaging modalities. According to this, also the availability of multiple TX-CT scans (or CBCT scans) of many different patients would probably not allow for a direct comparison of SOS maps with sufficient accuracy for an identification of the $\underline{\Delta}$SOS error with respect to the pure SOS error.

If no correction is applied, INTER and INTRA workflows produce comparable errors in terms of SOS aberration for patient positioning if changes occur between SIM and TX, with results varying according to the specific type of change. If a replacement of tissues with very different SOS values, particularly on the opposite sides of the SOS range with respect to 1540 m/s, occurs, INTRA gives worse results (Fig 1, Fig 5, Table 3.A and 3.B), while it works better if the replacement happens between tissues with similar SOS values (Table 3.A and 3.B). Corrected workflows not only provide better results in terms of positioning accuracy (Table 3.C and 3.D), but also in terms of absolute localization of structures: if the SIM images are used to contour structures in fused CT/US images and these contours are then used for planning purposes, dose distributions will be more accurate if the correction has been applied.

5.5 Conclusions

The purpose of this study was to find how the possible approaches to patient positioning using US-gRT are sensitive to SOS aberration change between SIM and TX, and to provide worst case scenario quantitative estimates in a dual layer phantom. Four different scenarios of changes were considered for the two workflows examined, INTRA and INTER, with or without SOS aberration correction. A detailed analysis of possible outcomes was performed and tested in phantom measurements showing that for the cases studied the shift suggested at TX can be up to 4 mm different from the correct one, for INTER; and up to 3 mm for INTRA. In general, a SOS aberration correction provides better results, with errors smaller than INTRA and INTER and typically below the intrinsic resolution of imaging devices (1 mm), therefore negligible. This also implies that the effect of SOS distribution change between SIM and TX is a second order effect in clinical cases.

In particular, it was established that a SOS aberration correction based on the SIM-CT scan can be applied also on the subsequent TX-US scans with quantitative results exhibiting minor errors.

Aknowledgements

Resonant Medical (Elekta) is thanked for support and discussion, in particular Dr. Martin Lachaine. Silvia Pesente e Francesco Pascoli (Tecnologie Avanzate Srl) and Denis Ermacora (Datamind Srl) are thanked for the fruitful suggestions.

5.6 References

1. Lattanzi J, McNeeley S, Pinover W, Horwitz E, Das I, Schultheiss TE, et al. A comparison of daily CT localization to a daily ultrasound-based system in prostate cancer. International journal of radiation oncology, biology, physics. 1999;43(4):719-25.
2. Lattanzi J, McNeeley S, Donnelly S, Palacio E, Hanlon A, Schultheiss TE, et al. Ultrasound-based stereotactic guidance in prostate cancer--quantification of organ motion and set-up errors in external beam radiation therapy. Comput Aided Surg. 2000;5(4):289-95.
3. Trichter F. Prostate localization using transabdominal ultrasound imaging. International Journal of Radiation Oncology*Biology*Physics. 2003;56(5):1225-33.
4. Serago CF, Chungbin SJ, Buskirk SJ, Vora SA, McLaughlin MP, Ezzell GA. Initial experience with ultrasound localization for positioning prostate cancer patients for external beam radiation therapy. International journal of radiation oncology, biology, physics. 2001;51(3):94.
5. Wein W, Roper B, Navab N. Integrating diagnostic B-mode ultrasonography into CT-based radiation treatment planning. IEEE Trans Med Imaging. 2007 Jun;26(6):866-79.
6. Berrang TS, Truong PT, Popescu C, Drever L, Kader HA, Hilts ML, et al. 3D ultrasound can contribute to planning CT to define the target for partial breast radiotherapy. Int J Radiat Oncol Biol Phys. 2009 Feb 1;73(2):375-83.
7. Fraser D, Fava P, Cury F, Vuong T, Falco T, Verhaegen F, editors. Evaluation of a prototype 3D ultrasound system for multimodality imaging of cervical nodes for adaptive radiation therapy2007: SPIE.
8. Fraser DJ, Chen Y, Poon E, Cury FL, Falco T, Verhaegen F. Dosimetric consequences of misalignment and realignment in prostate 3DCRT using intramodality ultrasound image guidance. Med Phys. 2010 Jun;37(6):2787-95.
9. Fraser DJ, Wong P, Sultanem K, Verhaegen F. Dosimetric evolution of the breast electron boost target using 3D ultrasound imaging. Radiother Oncol. 2010 Aug;96(2):185-91.
10. Xing L, Thorndyke B, Schreibmann E, Yang Y, Li TF, Kim GY, et al. Overview of image-guided radiation therapy. Med Dosim. 2006 Summer;31(2):91-112.
11. Smith WL, Lewis C, Bauman G, Rodrigues G, D'Souza D, Ash R, et al. Prostate volume contouring: a 3D analysis of segmentation using 3DTRUS, CT, and MR. Int J Radiat Oncol Biol Phys. 2007;67(4):1238-47.
12. Huang YL, Chen DR. Automatic contouring for breast tumors in 2-d sonography. Conf Proc IEEE Eng Med Biol Soc. 2005;3:3225-8.
13. Huang YL, Jiang YR, Chen DR, Moon WK. Level set contouring for breast tumor in sonography. J Digit Imaging. 2007 Sep;20(3):238-47.
14. Molloy JA, Srivastava S, Schneider BF. A method to compare supra-pubic ultrasound and CT images of the prostate: technique and early clinical results. Med Phys. 2004 Mar;31(3):433-42.
15. Fung AY, Ayyangar KM, Djajaputra D, Nehru RM, Enke CA. Ultrasound-based guidance of intensity-modulated radiation therapy. Med Dosim. 2006 Spring;31(1):20-9.
16. Johnston H, Hilts M, Beckham W, Berthelet E. 3D ultrasound for prostate localization in radiation therapy: a comparison with implanted fiducial markers. Med Phys. 2008 Jun;35(6):2403-13.
17. Morr J, DiPetrillo T, Tsai JS, Engler M, Wazer DE. Implementation and utility of a daily ultrasound-based localization system with intensity-modulated radiotherapy for prostate cancer. Int J Radiat Oncol Biol Phys. 2002 Aug 1;53(5):1124-9.
18. Dube F, Sheldon T, editors. SU-GG-J-22: Accuracy of Implicit Registration Between CT and 3D US in the Radiotherapy Simulation Process2008: AAPM.
19. Mast TD. Empirical relationships between acoustic parameters in human soft tissues. Acoustics Research Letters Online. 2000;1(2):37-42.
20. Hill CR, Dunn F. Physical Principles of Medical Ultrasound edited by C. R. Hill. The Journal of the Acoustical Society of America. 1987;82(2):721.

21. Carson PL. Biomedical ultrasonics. By P.N.T. Wells, Ph.D., Academic Press, Inc. London, Copyright 1977. 635 pages. $46.90. Journal of Clinical Ultrasound. 1978;6(2):126-7.
22. Cury FL, Shenouda G, Souhami L, Duclos M, Faria SL, David M, et al. Ultrasound-based image guided radiotherapy for prostate cancer: comparison of cross-modality and intramodality methods for daily localization during external beam radiotherapy. Int J Radiat Oncol Biol Phys. 2006 Dec 1;66(5):1562-7.
23. Fontanarosa D, van der Meer S, Harris E, Verhaegen F. A CT based correction method for speed of sound aberration for ultrasound based image guided radiotherapy. Med Phys. 2011 May;38(5):2665-73.
24. Wang L, McCarthy KL, McCarthy MJ. Effect of temperature gradient on ultrasonic Doppler velocimetry measurement during pipe flow. Food Research International. 2004;37(6):633-42.
25. Kleis SJ, Sanchez LA. Dependence of sound velocity on salinity and temperature in saline solutions. Solar Energy. 1991;46(6):371-5.
26. Grosso VAD, Mader CW. Speed of Sound in Pure Water. The Journal of the Acoustical Society of America. 1972;52(5B):1442-6.
27. Fontanarosa D, van der Meer S, Bloemen-van Gurp E, Stroian G, Verhaegen F. Magnitude of speed of sound aberration corrections for ultrasound image guided radiotherapy for prostate and other anatomical sites. Med Phys. 2012 Aug;39(8):5286-92.

Chapter 6

A speed of sound aberration correction algorithm for curvilinear ultrasound transducers in ultrasound based image guided radiotherapy

Davide Fontanarosa
Silvia Pesente
Francesco Pascoli
Denis Ermacora
Imad Abu Rumeileh
Frank Verhaegen

Published in: Physics in Medicine and Biology, 58:1341-1360, 2013.

Abstract

Conventional ultrasound (US) devices use the time of flight (TOF) of reflected US pulses to calculate distances inside the scanned tissues and thus create images. The speed of sound (SOS) is assumed to be constant in all human soft tissues at a generally accepted average value of 1540 m/s. This assumption is a source of systematic errors up to several millimeters and of image distortion in quantitative US imaging. In this work an extension of a method recently published (Fontanarosa *et al.*, 2011) is presented: the aim is to correct SOS aberrations in three-dimensional (3D) US images in those cases where a spatially co-registered computerized tomography (CT) scan is also available; the algorithm is then applicable to a more general case where the lines of view (LOV) of the US device are not necessarily parallel and coplanar, thus allowing correction also for US transducers other than linear. The algorithm was applied on a multi-modality pelvic US phantom, scanned through three different liquid layers on top of the phantom with different SOS values; the results show that the correction restores a better match between the CT and the US images, reducing the differences to sub-millimeter agreement. Fifteen clinical cases of prostate cancer patients were also investigated: the SOS corrections of prostate centroids were on average +3.1 mm (max +4.9 mm – min +1.3 mm). This is in excellent agreement with reports in the literature on differences between measured prostate positions by US and other techniques, where often the discrepancy was attributed to other causes.

6.1 Introduction

Ultrasound (US) imaging is an important technique for soft tissues, used both for diagnostic (Brascho, 1977) and verification purposes (Kim *et al.*, 2011) in radiotherapy. The advantages of this modality are high resolution, acquisition speed, reliability, absence of side effects, cost and maintenance efficiency, and exciting novel developments (Freeman, 2011). This implies a wide range of applications as image guided radiotherapy (IGRT) (Xing *et al.*, 2006) technique in organ motion monitoring in Intensity Modulated Radiation Therapy (IMRT) (Ling *et al.*, 2006) and Volumetric Modulated Arc Therapy (VMAT) (Webb and McQuaid, 2009), in which patient positioning is of the utmost importance. US imaging is based on measuring the time lapse between the emission of a mechanical pressure wave by the transducer and the receiving of the returning echoes; the time of flight of the pulse (TOF) (Wild, 1950). The distance traveled by the wave is derived by assuming a constant US speed of sound (SOS) of 1540 m/s (Carson, 1978) in the body, while the actual SOS ranges from 1450 m/s in fat to 1613 m/s in connective tissue at body temperature (37°C) (Mast, 2000). This leads to systematic errors in calculated distances of up to $\pm 6\%$, which may correspond to several millimeters in the position of the reflecting or scattering interface, depending on its depth in the body.

As shown earlier (Fontanarosa *et al.*, 2011), the Hounsfield Units (HU) of a co-registered computerized tomography (CT) image can be used to create a SOS map of the scanned tissues and to correct for SOS aberration. The correction was presented for single two-dimensional (2D) US images produced by a linear transducer, where the approximation of lines of view (LOV) by vertical lines was acceptable. When curvilinear transducers are used or when a more general approach to arbitrary 3DUS volumes is needed, a geometry change from the native pixel format to 3D voxel matrices is required. In particular, when a curvilinear transducer is used, the field of view (FOV) of the US scan and the related beam path parameters must be determined before the correction can be applied. Because the correction is cumulative along any LOV, the latter must be known to a certain degree of accuracy to apply the correction. Some features, described in detail in the following section, have been developed specifically to overcome this issue and to perform a full 3D SOS aberration correction.

In this paper the correction strategy is described, and the algorithm is applied to phantom and patient geometries.

6.2 Materials & Methods

Datasets and instrumentation

The algorithm was developed and tested using both phantom and patients co-registered CT and 3DUS image datasets.

The US phantom used is a male anthropomorphic multi-modality pelvic phantom (Model 048, CIRS - Computerized Imaging Reference Systems Incorporated, Norfolk, VA, USA[1]), containing inserts mimicking pelvic bones, bladder, prostate, urethra, seminal vesicles and rectum, with certified volumes. All the internal structures and the background material have a reported SOS value of 1540 m/s at 22 °C and are made of Zerdine® material, whose SOS temperature dependence is similar to water's. All the measurements were acquired using Ultrasonix convex transducers (type C5-2/60, center frequency 3.5 MHz, Sonix Series, Ultrasonix Medical Corporation, Richmond, BC, Canada).

The patient images are from fifteen clinical prostate cancer cases from different hospitals: five from MAASTRO Clinic (Maastricht, the Netherlands), five from Azienda Ospedaliera "Maggiore della Carità" (Novara, Italy) and five from CRO Oncologic Referral Center (Aviano (PN), Italy). They were all scanned with Clarity™ 3DUS Systems (Elekta, Stockholm, Sweden). These systems contain US stations equipped with optically tracked US probes. Reflective markers are attached to the probes to track their 3D position and orientation during scanning using an infrared camera. The position tracking components are used to acquire and reconstruct a 3D US image, relative to the coordinate system of the room.

Algorithm description

The cumulative SOS aberration correction algorithm needs to be applied along the LOVs of the US system (Fontanarosa *et al.*, 2011). The original US raw data lie in space along the physical LOV of the US system, so they would be the most natural choice for this kind of application. In most of the cases, though, the US system manufacturers do not provide the radio frequency (RF) or raw data: often an expensive research license is necessary to access these data. So in order to make the algorithm as widely applicable as possible, it was decided to work with the clinical US volumes as they are produced by the Clarity software, which is re-sliced and re-sampled along the CT scan axial planes (Fig. 1a). The image acquisitions of curvilinear probes are performed by rocking the probe around the contact point with the patient or the phantom; this produces a FOV with a trapezoid shape both in the lateral direction and the elevational direction, as is shown in Fig. 1b.

[1] http://www.cirsinc.com/products/all/62/multi-modality-pelvic-phantom/

Considering the CT and US volumes as 3D matrices, each matrix element has four values associated to it: three spatial coordinates x, y, z and a HU value (CT image); or a brightness value (US image). A HU to density table should be available for all the CT scans performed for radiotherapy purposes which rely on density to calculate the dose. With this, the CT matrix can be transformed in a physical density matrix and the latter, applying a published linear relation (Mast, 2000), can then be converted in a SOS map of the scanned volume. Corresponding voxels allow for an exact mapping of the real SOS inside the volume. The correction is cumulative though, meaning that for each voxel it depends on the integral of the SOS values along the LOV of the system from the transducer to the voxel. This means that a voxel by voxel knowledge of SOS values is not sufficient, and the LOV must be properly spatially identified. The real LOV cannot be derived from the post-processed US images, since the US volume is composed of slices aligned with the CT scan and no information about LOV directions in 3D space is provided; consequently, the LOVs must be spatially reconstructed in reverse from the final US volume. LOVs are approximated as straight lines in our algorithm.

After the LOVs are determined, the algorithm can take into account the length of the path along each traversed voxel with relative SOS. This information is then used to calculate the corrected distance for all the following voxels and the image is remapped, assigning to each voxel the correct brightness value. All these steps are described in detail in the following subsections.

Image pre-processing

Co-registered CT and US images were exported from the Clarity system via DICOM protocol. Since the algorithm requires 3D volumes while the exported data are organized in axial slices, a procedure was developed to obtain a 3D matrix from the original planes. This operation is performed by creating a 3D volume and assigning to each voxel a HU or brightness value obtained from interpolating between the values of the two pixels in the slices nearest to the voxel center along the cranio-caudal direction.

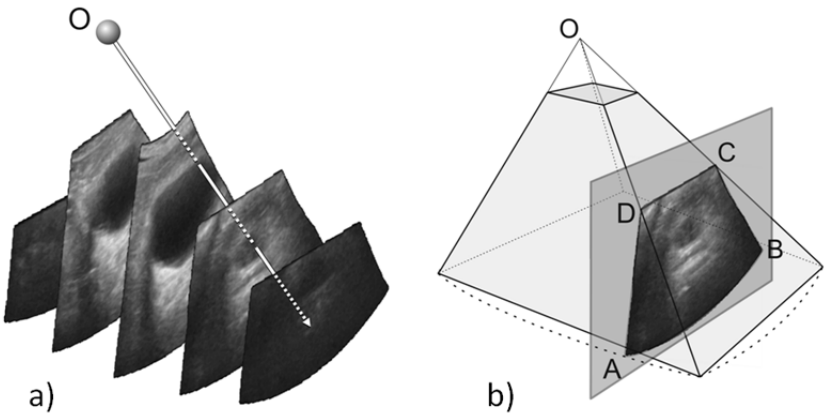

Fig. 1: a) US planes re-sliced and re-sampled along the CT scan axial planes; a LOV is plotted as an example as the white arrow starting from the origin O of the US volume. This origin is intended to be the top of the pyramid used to approximate the US volume. **b)** A graphic representation of the spatial dependence of the FOV of the US volume (pyramid, light gray). A single axial CT slice is shown in the patient frame of reference (vertical dark gray plane) and their intersection (US image), delimited by vertices A-D.

Determination of the FOV

The FOV of the US imaging device was modeled as a "truncated pyramid", as shown in Fig. 1b, where the apex O is assumed to be the origin of the US scan lines. The origin is used to determine the direction (represented by the LOV) on which the correction will be performed; the value of the correction for each voxel is given by the accumulation of the ratios of the local SOS values with the reference value of 1540 m/s (SOS_{ref}) along the LOV on which the voxel lies. This point is further analyzed in the section **SOS correction procedure**.

In order to define in space the US FOV, side and base edges of the pyramid must be determined. Fig. 1b shows the FOV of the US volume and one of the axial CT slices in the patient frame of reference: the intersection of the two, represented in Fig. 1b by the dark gray area, defines a subset of the US scanned volume (hereafter referred to as *US image*). The vertices of each US image (points A-D in Fig. 1b), whose absolute coordinates are provided by the Clarity system, are used to reconstruct the base edges of the pyramid (A and B), and the side edges (C and D).

The apex of the pyramid is then determined as follows:

- For all the US images the position of all the vertices is determined, obtaining a collection of points A_i, B_i, C_i and D_i (section **Determination of the vertices of the FOV**).
- From this collection, using the random sample consensus (RANSAC) method (Fischler and Bolles, 1981), points are identified belonging to the different side and base edges of the "truncated pyramid" and then fitted linearly to determine

the straight lines corresponding to the FOV edges (section **Determination of the edges of the pyramid**).

- From the intersection of these lines the apex of the pyramid (point O in Fig. 1a) can be approximately determined (section **Determination of the apex of the pyramid**).

Determination of the vertices of the FOV

For each US image a mask was created binarizing the image using zero as brightness threshold level, meaning that the zero level is characteristic only for pixels outside the US scanned volume. In case the zero level is associated also to pixels inside the US volume, some artifacts might be generated, especially on the mask boundaries. These can be easily reduced, though, by applying a morphological closing operation (Svalbe and Jones, 1992). The closing filter operation smoothes boundaries, reduces small inward bumps, joins narrow breaks and fills small holes caused by noise, without generating, in general, any degradation of the image.

The relevant vertices are then extracted for each mask using a scale invariant vertex detector that is a slightly modified version of the Difference-of-Gaussian (DoG) operator (Lowe, 2004). In its original version, this operator convolves multiple times the source image I(x,y) with a Gaussian kernel G(s), where s is the scale parameter and denotes the standard deviation of the Gaussian (s=σ). With this procedure a series of images I[s](x,y) or, equivalently, a multiscale representation of the original image I(x,y,s), is obtained. The operator response, that is a first order approximation of a multiscale Laplacian L(x,y,s), is obtained by taking for each s the difference of each couple of images at adjacent scales:

$$L(x,y,s) \equiv L[s](x,y) = I[s](x,y) - I[s-1](x,y) \qquad (6.1)$$

where s is such that $\sigma_{i+1} = k\sigma_i$, with k = 1.2, σ_0 = 1.7 and i = 0, 1, … , 7.

(Lowe, 2004) reports that no impact on the stability of extrema detection or localization has been found for k values ranging from 1 to 1.4, even for significant scale differences. The choice of σ_0 value depends on the resolution of the US images. Our choice was based on a trial-and-error procedure on images resampled on CT scan resolution. It is thus a generally acceptable value for most of the US-gRT applications were this condition always holds. An accurate analysis of these parameters has been performed and will be reported in section 3, confirming a posteriori the choice made.

As this operator is scale invariant, to obtain at the same time the position and the scale of relevant vertices or edges, it is only required to find the local extrema in a 3D neighborhood of the multiscale (sampled) representation of the operator L(x,y,s); this means that each sample point (x_P,y_P,s_P) is compared to its eight neighbours in the image L[s_P] and nine neighbours in the images at scales s_{P+1} and s_{P-1}. To complete the vertex detection, edge responses must be excluded. As vertices have at least two

directions with a substantial difference, while edges have only one such direction, we can simply consider, among the found local extrema points, only those whose eigenvalues of their Hessian matrix H have comparable magnitudes (Lowe, 2004). This multiscale approach was used to select with the highest possible accuracy, among all the vertices that a detector could find, only those that were large enough to be relevant for our purposes; thus the smallest ones, which could emerge from noise of small artifacts along the mask boundary, were excluded. To this end, in our implementation of the selection step of the DoG detector, we did not search for the maxima over a 3D neighborhood (we did not want to select the scale of maximum response), but only over the spatial 2D neighborhood for each scale. This way, the set of vertices found comprises multiple instances of each relevant vertex at different scales, as well as other instances that represent smaller vertices. This collection was reordered by scale and partitioned by location; thus the relevant vertices, which are present at greater values for the scale parameter, were mapped at their small-scale instances, which have a more accurate spatial localization. At the same time, the vertices associated to noise or artifacts, that have only small scales values without a large-scale counterpart, are rejected. Only the points with a minimum number of reference instances for different scales are considered. The best results were empirically found by setting the threshold to the value of 5. To minimize the noise a limit was set to the total number of vertices accepted for each image, which was set to 6 to account for possible cut vertices. To be accepted, all the points must be inner points of the original mask. The slice vertices for an example US volume are shown in Fig. 2a.

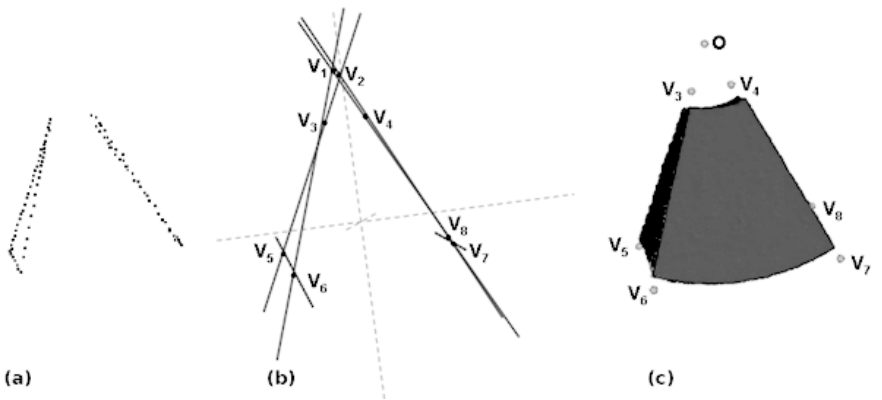

Fig. 2: (a) Collection of vertices determined for all the US slices. **(b)** Straight lines corresponding to the FOV edges, V_1-V_4 points corresponding to the FOV vertices. **(c)** Comparison of the calculated vertices (V_3 – V_8) and the mask of the real FOV of the US scan as obtained by the binarization process.

Determination of the edges of the pyramid

As the vertices of the collection define different edges (sides and bases) of the pyramid, the RANSAC method was used to associate each of them to the correct edge. The RANSAC is an algorithm for robust fitting of models in the presence of many data outliers (noisy or erroneous data). It is an iterative procedure that seeks the maximum number of inliers (accurate data) by leaving out as many outliers as possible. The model used was a straight line: the purpose was to reconstruct the LOVs, not the real shape of the image, which has a curved base as depicted in Fig. 2(c). The tolerance to check for inliers was set to a distance of 10 mm on the normal direction.

This procedure was applied to identify the different sets of points defining the edges of the pyramid. To avoid incorrect edge reconstruction we discarded sets with a number of points below a given threshold; this was calculated as the total number of planes of the US scan divided by 8, an empirical value which has produced the best results and at the same time reduced the loss of edges characterized by few points.

The influence of this parameter on the results of the algorithm was analyzed and the results will be reported in the **Results** section.

For each set of points a linear fit was performed to determine the straight lines corresponding to the FOV edges (solid dark gray lines in Fig. 2b).

Also the bottom base edges can be approximated with straight segments (Fig. 2b), and thus reconstructed with the fitting procedure. The "truncated pyramid" has also a top base, whose edges are characterized by too few points and discarded by the fitting procedure (therefore not depicted in Fig. 2a).

Determination of the apex of the pyramid

The FOV points (V_1-V_8 in figure 2b) were obtained as intersections of all the possible couples of straight lines plotted following the procedure described in the section **Determination of the edges of the pyramid**. In a 3D space lines might not intersect; therefore, for each straight lines couple, both the point of closest approach (point that minimizes the total summed distance of two lines) and the minimum distance value between the lines were determined. Among all the points found, only those with a minimum distance below a specific threshold (set to 10 mm) were selected; this value is a good compromise between the sensitivity to reconstruction uncertainties and intersection of lines that are not related to pyramid vertices. A detailed analysis of this parameter is reported in the **Results** section.

To distinguish between the two different sets of points (V1-V4) and (V5-V8), the distance between the points and the US FOV main symmetry axis was used (dashed vertical line in Fig. 2b). As shown in Fig. 2c, the mean position of the two points V1 and V2 can be assumed as the hypothetic apex of the pyramid, while V3 and V4 approximate the positions of the more external transducer crystals of the array. To distinguish

between these two different sets of points (V1, V2 and V3, V4), the distance between the points and the US volume was used.

According to the distance of these points to the US volume, five different cases were considered:

i. the vertices V1, V2, V3 and V4 are identified and V1-V2 are separated from V3-V4. In this case the origin is given by the mean position of V1 and V2, but also an origin averaged between V3 and V4 can be used.
ii. Only the vertices V1 and V2 are identified. In this case the origin is given by the mean position of V1 and V2.
iii. Only the vertices V3 and V4 are identified. In this case an origin averaged between V3 and V4 can be used.
iv. In all the other cases (for example 5 vertices found, only one vertex found, or other combinations) the origin is given by the mean position of all the vertexes found.
v. No vertex is found.

For sake of simplicity, it is assumed from this point on that the origin was given by the mean position of V1 and V2, but also the other cases were properly addressed in the algorithm.

SOS correction procedure

In the second part of the process the correct US matrix volume was reconstructed. Taking into account the real SOS in each voxel of the traversed tissues along the US scan lines, the correct path length travelled by the US waves was calculated; then the correct source location for the brightness value to be assigned to each voxel of the new US matrix volume was determined.

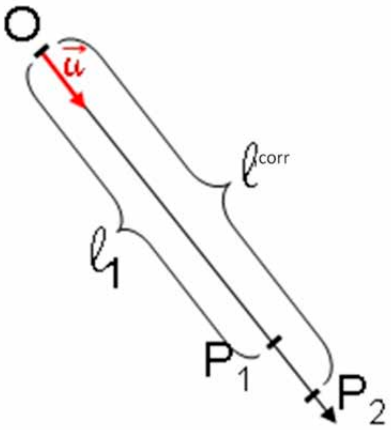

Fig. 3: Representation of the SOS aberration correction along a reconstructed US scan line: starting from the calculated origin position O, along the direction given by the unit vector **u,** the position P_1 at a depth l_1 is remapped to P_2 at depth l^{corr}.

In a general case, given a point P_1 along the US scan line of a reconstructed US volume, we are interested in determining the real position P_2 (Fig. 3): this corresponds to the apparent position that P_1 has if the real SOS of tissues traversed were considered. A representation of a US scan line is shown in Fig. 3, where O is the origin of the scan line (apex of the pyramid, Fig 2c), l_1 is the reported path length between points O and P_1 and **u** is the unit vector defining the US scan line direction. The true position of point P_2 is obtained by the relation: $P_2 = O + l^{corr}\mathbf{u}$. The correct path length l^{corr} is given by the following integral:

$$l^{corr} = \frac{1}{SOS_{ref}} \int_0^{l_1} SOS(l)dl \tag{6.2}$$

where SOS_{ref} is the SOS value used for the US images reconstruction (SOS_{ref} = 1540 m/s) and SOS(*l*) is the SOS value of the tissues crossed by the US wave along the scan line at position *l*.

In the range of density values of human soft tissues, an increase in physical density corresponds to an increase in SOS, and the relationship can be approximated by a linear dependence (Mast, 2000). For the soft tissues considered in this work we used the following linear regression (Fontanarosa *et al.*, 2011), based on values for different human soft tissues at 37 °C published by (Mast, 2000), to create a SOS map from the CT scan co-registered to the US scan:

$$SOS = (1.09 \cdot \rho + 0.419) \cdot 10^3 \frac{m}{s} \pm 3.5 \frac{m}{s} \tag{6.3}$$

As the scanned volume is discretized into voxels, the line integrals (Eq. 6.2) can be as well discretized into weighted sums. We used the lines connecting the center of each US matrix voxel to the apex of the pyramid O as US scan lines. Hence the line integral from the apex O to a voxel centered in P_2 (d), over the discretized volume, can be written as the following weighted sum:

$$d = \frac{1}{SOS_{ref}} \sum_{(i,j,k)} l(i,j,k) \cdot SOS(i,j,k) \tag{6.4}$$

where SOS(i,j,k) is the SOS value of voxel (i,j,k) that is obtained from the SOS map previously calculated, and l(i,j,k) is the exact path length of the US scan line into voxel (i,j,k), calculated using an algorithm developed by Siddon (Siddon, 1985) and implemented by Christiaens (Christiaens *et al.*, 1999). These algorithms were developed to calculate the exact radiological paths through a pixel or voxel space for the reconstruction of medical images.

A reverse mapping approach was then used: for each voxel of the US matrix volume the correct source location for the brightness value to be associated to the

considered voxel was determined. The localization procedure was performed as follows:

1. For voxel (i,j,k) centered in P_2 (as shown in figure 4c), the line of view connecting the origin O with point P_2 was defined.
2. In the SOS matrix all the intersections between the scan line and the voxel sides were determined, obtaining an array of increasing distances from the origin O (d_{n-3}, d_{n-2}, d_{n-1}, d_n in Fig. 4a).
3. From the SOS matrix the SOS values of each traversed voxel (SOS(i-2,j-1,k), SOS(i-1,j-1,k), SOS(i-1,j,k) in Fig. 4a) were determined.
4. The value of the path length into each SOS voxel is given by the difference of two adjacent distance values of the array, for example in figure 4a: l(i-2, j-1,k) = d_{n-2} - d_{n-3}.
5. Using Eq. 6.4 the contributions of all the voxels encountered along the scan line are summed, until the point P_2 is reached:

$$\sum_{g=0}^{n-1} l_g^{corr} < d \tag{6.5}$$

Where

$$l_g^{corr} = d_g^{corr} - d_{g-1}^{corr} \tag{6.6}$$

and

$$d_g^{corr} = \frac{1}{SOS_{ref}} \sum_{v=0}^{g} l_v \cdot SOS_v \tag{6.7}$$

6. As the condition in Eq. 6.5 becomes false, the process is stopped and the distance ($d^{corr}{}_n$) at the next iteration step is determined with Eq. 6.7;
7. The exact position of point P_1 (shown in figure 4b) corresponding to P_2 in the US volume can be calculated exploiting the proportion between the distances d and $d^{corr}{}_n$ from $d^{corr}{}_{n-1}$. The position of P_1 can then be calculated with the following expression:

$$P_1 = O + \hat{u} \cdot d_{n-1} + \hat{u} \cdot (d_n - d_{n-1}) \cdot \left(\frac{d - d_{n-1}^{corr}}{d_n^{corr} - d_{n-1}^{corr}} \right) \tag{6.8}$$

8. The brightness value to be associated to point P_2 was then calculated starting from point P_1, as a weighted interpolation of the brightness values of all its eight neighboring voxels.

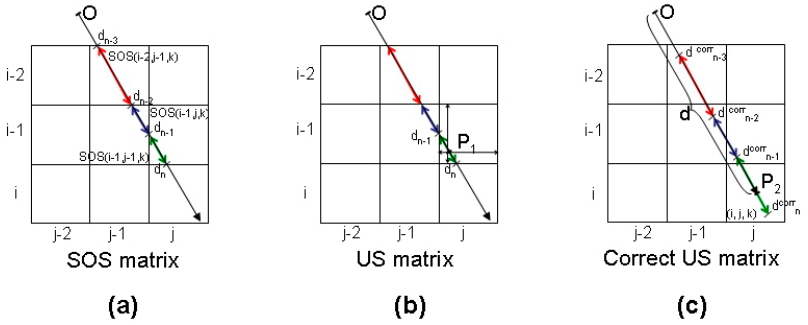

Fig. 4: a) The SOS matrix, shown in a 2D representation. The path lengths in the SOS matrix (colored segments) are calculated from the intersection points d_i of the LOV with the voxel edges. **b)** The beam path in the US matrix, with the point P_1 plotted where the correction is going to be calculated. **c)** The US matrix with the corrected beam path, where the point P_1 is repositioned to P_2.

Measurements

The algorithm was written in the C language and the tests were performed in a Windows 7 64-bit environment on a laptop equipped with a 8-core 2.3 GHz Intel processor with 16 GB RAM. For the execution time estimate, two separate steps can be considered: the time necessary for the determination of the FOV and of its origin; and the time required for the SOS correction procedure. The time required for the first step depends on the morphological procedures applied and on the number of planes analyzed for each US scan. For the cases considered in the article it ranges from about 8 s, in case of no morphological procedures applied and about 35 analyzed planes; to about 40 s, in case of morphological procedures applied and about 60 planes analyzed. The second step is strongly dependent on the number of voxels to correct; the correction can be applied on 130000 voxels/s, with our hardware and software configuration. On average about 10 seconds were necessary for this second step. It has to be noted that the execution time can be significantly further reduced, since the algorithm is still in a prototype version and not completely optimized yet. Our goal would be, during the evolution of the prototype, to make the whole process last less than a second, for applications in real time imaging. This could be achieved carefully selecting the hardware in order to enhance parallelization as much as possible; and, above all, finding alternative ways to identify the position of the origin, which is the most time consuming, extracting it for example from the localization system of the probe.

The algorithm was tested on a set of 3D US and co-registered CT images scanned on a pelvic multi-modality phantom with anthropomorphic inserts with a constant SOS of 1540 m/s at 22°C. The SOS increase in the phantom is about 2.0-2.5 m/s for every degree C increase (information provided by phantom manufacturer). Since the meas-

ured room temperature during the acquisitions was 24 °C, the phantom SOS value was estimated to be 1545 m/s.

To introduce an aberration, a layer with a different SOS value was created placing a plastic container on top of the phantom (see Fig. 5), filled with either pure water (SOS of 1494 m/s (Grosso and Mader, 1972)), sunflower oil (SOS of 1465 m/s (Wang *et al.*, 2004)), or 17% saline solution. Different sources report different SOS values for this solution: from 1600 m/s (OndaCorp, 2003) to 1665 m/s (Al-Nassar *et al.*, 2006) and 1684 m/s (Kleis and Sanchez, 1990). We used a SOS value of 1665 m/s, in accordance to our own experimental measurements performed at MAASTRO Clinic and at Azienda Ospedaliera "Maggiore della Carità", comparing the distances measured on US images of phantoms filled with 17% saline solution with the same distances measured on the co-registered CT scan. The values are reported at a temperature of 24 °C and the thickness of the liquid layer seen by the probe was about 40 mm to obtain a measurable shift in the distances.

The curvilinear transducer was kept at a fixed height by a support, allowing a rocking motion around the contact point (Fig. 5a). The liquids were poured into the container until the transducer surface was completely covered, ensuring that no air was trapped underneath; this way shadow zones were avoided in the FOV. The distance between the central part of the probe and the phantom surface was 37 mm, measured with the probe in the vertical position. The rotation axis was not at the transducer surface but at the contact points between the probe and the support device, located on both sides of the probe surface at a distance of about 2.8 cm from the center of the transducers array; thus the distance between the transducer and the phantom was measured and then used for the correction for every slice used to check the results of the algorithm. Moreover, due to its curvilinear shape, the actual liquid thickness between the transducer and the phantom surface changes; this issue was disregarded in the calculations because it gives rise to variations of the second order with respect to the main correction. The measurements were performed holding the probe in the vertical position then rocking it around the contact points with the support until the whole prostate was imaged through the bladder. The scan procedure was similar to the clinical scan procedure (Fig. 5b).

Both the correction and the registration of the US and the CT images were performed in 3D. The registration was a rigid image translation, based on the information provided by the whole image set. The delineated regions of interest (ROI) corresponding to prostate and bladder were used as a reference. When visible in the US scan, the urethra was also used. Rotation and deformation were not applied: the introduced SOS aberration was generated only in the container on top of the phantom and then propagated inside with a constant value, since the material of which the phantom is made has a uniform SOS value of 1545 m/s (at 24°C), which is very close to 1540 m/s (value assumed by the US system) and so creates negligible aberrations. Therefore, no deformation or shift should happen while the beam traverses the phantom.

Finally, the correction algorithm was applied to fifteen clinical prostate cancer cases, provided by three different hospitals to prove its general use and independence from scanning protocols and equipment.

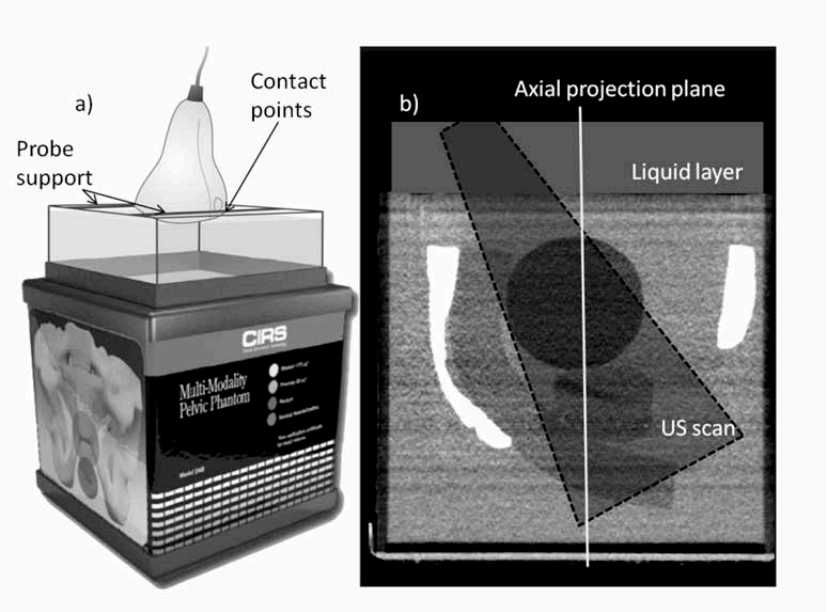

Fig. 5: a) The CIRS male pelvic phantom with on top the liquid-holding container, the probe and its support. The contact points (the left one is indicated by the arrow) are two notches on the sides of the probe. **b)** Superposition of the CT scan of the phantom with the liquid container on top and a graphic representation of the US FOV in a sagittal projection. The white line shows the axial plane along which the manual registration was performed.

6.3 Results

SOS correction

The comparisons between the CT and US scans of the phantom with the added liquid container (Fig. 5) are shown on axial projections of the volumes and show a difference in the position of the organs in all the analyzed configurations (Fig. 6).

Figures 6a1-6c1 show in a split image the original US and CT scans for the different liquids. Figures 6a2-6c2 show the comparisons between the US scan after the application of the algorithm and the CT scan for the three cases. After the correction the images show an excellent matching of the bladder-prostate region along all lines of view, with differences smaller than the intrinsic resolution of the CT scan (around 0.7 mm in the axial plane).

In this work, 'shift' indicates the translation needed to restore the correct match between images to compensate for SOS aberration. In Table 1 the "Measured shift" column reports for the three different liquids the measured shift of phantom structures, projected in the axial plane visualized, applied to register the US and the CT scans. The estimated uncertainties are around half the linear dimension of a pixel in the axial projection (square with a 0.7 mm side), because this is the accuracy with which the registration could be evaluated manually. In the "Calculated shift" column, the shift value calculated by the correction algorithm in the centroid of the prostate for the three configurations is reported.

Table 1 shows an excellent agreement between measured and calculated shifts. The measured shifts are the shifts necessary to fuse the original US scan with the coregistered CT scan, to compensate the effect of SOS aberration generated by the presence of the container filled with liquids with SOS values different than 1540 m/s; the calculated shifts are the shifts reported by the SOS correction algorithm. On the phantom the SOS aberration was introduced on purpose and isolated from other aberrations; here the algorithm produces a correction which is identical, within the accepted errors, to what would be manually done by an operator to restore the spatial registration between the imaging modalities.

Table 1: In the second column the values of SOS at 24 °C for the three liquids used in the measurements to test the algorithm. In the 3rd column are reported the measured shifts to register the original US scan and the CT scan. In the "Calculated shift" column are the values of the cumulative shift calculated and applied by the algorithm to the prostate centroid. All the shifts are in the anterior-posterior direction (A-P), with positive sign when the shift is anterior and vice versa.

Liquid [24°C]	SOS (m/s)	Measured shift (mm)	Calculated shift (mm)
Water	**1494**	**1.4±0.4**	**1.1**
Sunflower oil	**1460**	**2.0±0.4**	**2.0**
17% saline solution	**1665**	**-3.2±0.4**	**-3.4**

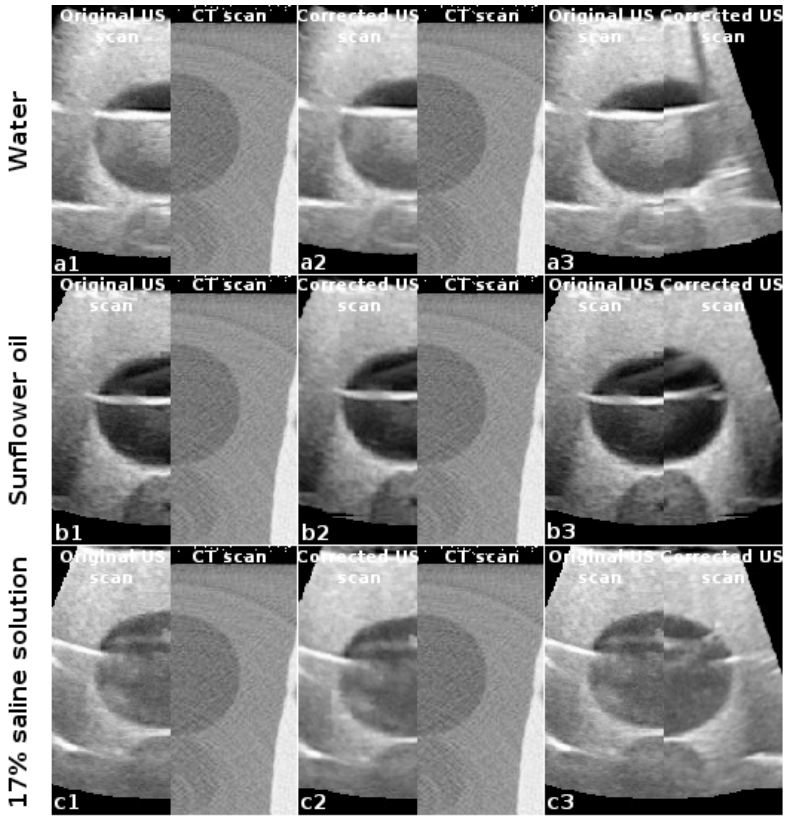

Fig. 6: Comparisons between the CT and the US images of the pelvic phantom, before **(1:** left column) and after **(2:** middle column) the application of the SOS aberration algorithm, and comparison between the US scan before and after the algorithm **(3)**, in the case of water **(a)**, sunflower oil **(b)** and 17% saline solution **(c)**. Left to right parts of the phantom are matched.

The SOS aberration correction algorithm was applied to fifteen clinical prostate cancer cases, for which CT and US co-registered scans were available. The scans were imported and analyzed as 3D volumes in an in-house made visualization module (DataMind Srl, Udine, Italy). An example of superposition of CT and US scans before and after application of the correction is shown in Fig. 7a and Fig. 7b respectively, in axial projection. The comparison of the US scan before and after the correction is shown in Fig. 7c. A map of the distribution of voxel shifts after the application of the SOS aberration correction is also plotted (Fig. 7d). After the correction, the center of the prostate shows an upward shift of 3.4 mm in this case. The position of the center of the prostate was measured as the average of the proximal and distal wall positions at prostate maximum diameter on the line connecting the apex of the FOV of the US image and the voxels measured (Fig. 7e), along the LOV of the US system.

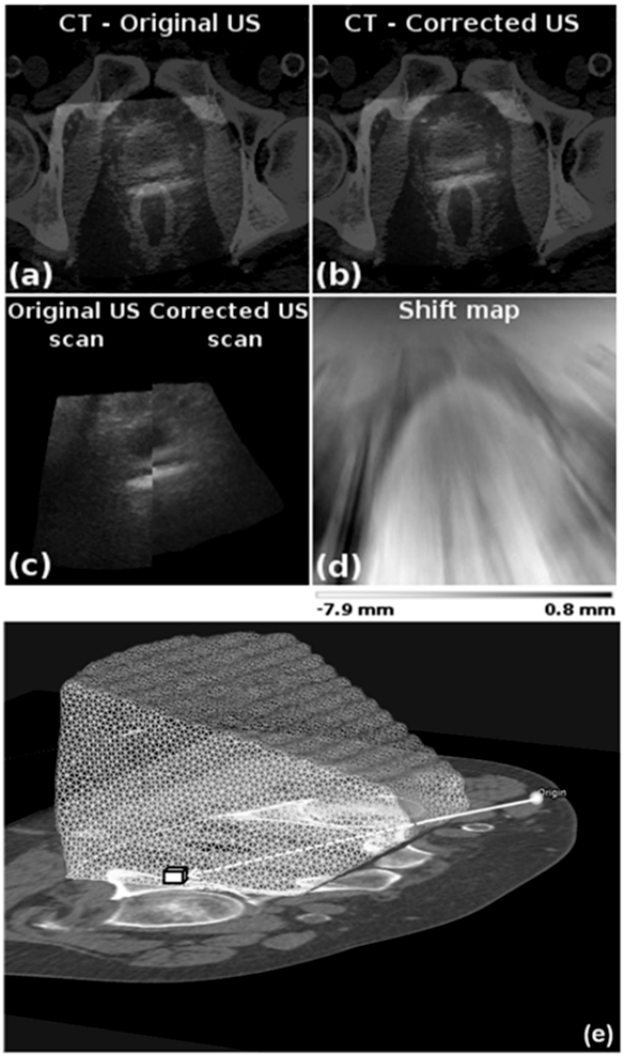

Fig. 7: An example of a prostate clinical case: Superposition in an axial projection of the CT scan with the US scan before **(a)** and after **(b)** application of the SOS aberration correction. **(c)** Comparison of the split US scans before and after the correction. **(d)** Map of the distribution of voxel shifts after application of the SOS aberration correction. **(e)** 3D visualization of US volume superimposed on the axial CT slice of the patient; in white, the LOV connecting the origin to the voxel where the correction has to be applied.

The same procedure was applied to the other clinical cases (Table 2), obtaining an average shift of 3.1±0.9 mm.

Table 2: Shifts of the prostate center obtained as average of the proximal and distal wall positions at prostate maximum diameter along the LOV of the US system, for fifteen clinical cases.

Patient	Prostate shift (mm)
1	2.7
2	3.9
3	1.3
4	3.4
5	2.9
6	3.6
7	2.1
7	2.1
9	4.3
10	3.2
11	4.9
12	2.4
13	4.1
14	2.4
15	2.8
Average	3.1
Standard deviation	0.9

Initially we assumed that approximating the US scan volume with a truncated pyramid and the origin of the US scan lines with the apex of the pyramid would not lead to large systematic errors. These considerations were supported by the fact that the origin is only used to determine the direction on which the correction is performed. The magnitude of the correction is only given by the deviation of SOS values from SOS_{ref} on the LOV itself. To test these assumptions and evaluate the influence of the sensitivity of the results to the accuracy of the origin position we moved the pyramid apex, assuming a worst case scenario value of 10 mm, in the x, y and z directions from the calculated position, for all 15 clinical cases; then we evaluated the shift values of the center of the prostate (Table 3) for the different possible origin positions. The mean values for the different positions are reported in Table 3 (Row 11) for each clinical case. The difference between the mean values and the shift values obtained considering no displacement in the pyramid apex are of the order of 0.2 mm (Table 3, Row 12); this is an order of magnitude smaller than the SOS aberration correction and below the CT physical resolution.

ΔX	ΔY	ΔZ	Prostate Shift (mm)													
	(mm)		Pat 1	Pat 2	Pat 3	Pat 4	Pat 5	Pat 6	Pat 7	Pat 8	Pat 9	Pat 10	Pat 11	Pat 12	Pat 13	Pat 14	Pat 15
0	*0*	*0*	2.7	3.9	1.3	3.4	2.9	3.6	2.1	2.5	4.3	3.2	4.9	2.4	4.1	2.4	2.8
10	*0*	*0*	3.4	4.1	2.9	3.5	3.1	3.0	1.6	2.5	4.2	2.6	4.7	2.1	4.0	2.7	2.7
0	*10*	*0*	2.8	4.0	1.4	3.5	2.4	3.5	2.5	3.0	4.1	3.2	5.1	2.6	4.1	2.4	2.6
0	*0*	*10*	3.2	4.1	0.6	3.9	2.9	4.1	2.6	3.4	4.8	3.3	5.3	2.8	3.7	2.5	3.3
-10	*0*	*0*	3.2	4.2	0.5	3.2	3.3	3.7	1.5	2.3	4.3	3.2	4.2	2.4	4.1	2.3	3.6
0	*-10*	*0*	2.8	4.0	0.3	3.2	2.6	3.4	1.7	2.2	3.9	2.6	4.6	2.4	4.1	2.1	2.9
0	*0*	*-10*	2.7	4.0	1.0	3.2	2.3	2.9	1.7	2.1	3.7	2.9	4.2	2.4	3.2	2.0	2.6
10	*10*	*10*	3.1	4.8	0.9	3.3	2.5	3.4	3.0	3.8	4.0	2.8	5.1	2.6	3.7	3.8	2.5
-10	*-10*	*-10*	3.0	3.8	1.0	3.2	2.2	2.9	1.3	1.9	3.4	3.2	3.9	2.5	3.2	1.9	3.3
Mean (mm)			3.0	4.1	1.1	3.4	2.7	3.4	2.0	2.6	4.1	3.0	4.7	2.5	3.8	2.5	2.9
Discrepancy between mean and unshifted values (mm)			0.3	0.2	0.2	0.0	0.2	0.2	0.1	0.1	0.2	0.2	0.2	0.1	0.3	0.1	0.1
Standard Deviation (mm)			0.3	0.3	0.8	0.2	0.4	0.4	0.6	0.6	0.4	0.3	0.5	0.2	0.4	0.6	0.4

Table 3: Displacement from the calculated position of the pyramid apex for the different considered origin positions for the 15 clinical cases; mean value; difference between the mean values and the shift values obtained considering no displacement in the pyramid apex and standard deviation.

Sensitivity analysis of the empirical parameters

A detailed sensitivity analysis of the influence of the main empirical parameters used in the algorithm for the determination of the apex of the pyramid was also performed. For five different datasets, the following parameters were analyzed: the coefficient used to calculate the minimum number of points required for the determination of the pyramid's edges (named from now on "par0"); σ_0 and k in [EQ. 6.1] (named "par1" and "par2", respectively); and the minimum accepted distance value between the lines used for the determination of the vertices of the pyramid ("par3"). The values used are reported in Table 4.

Table 4: Values of the parameters considered in the analysis: par0 = coefficient for the determination of minimum points per line; par1 = **σ0**; par2 = k; par3 = minimum distance between points of closest approach [mm].

Parameter	Values
par0	**5, 6, 7, 8**
par1	**1.2, 1.3, 1.4, 1.5, 1.6, 1.7, 1.8, 1.9, 2.0, 2.1**
par2	**1.10, 1.15, 1.20, 1.25, 1.30**
par3	**4, 5, 6, 7, 8, 9, 10, 11, 12, 13, 14, 15**

Analyzing the distributions of the position of the apex for each dataset and for each combination of parameters, a clear clustering of the points is evident. A fuzzy version of the ISODATA k-means algorithm, as proposed in (Dunn, 1974), was used to identify the clusters. In Fig. 8 the clusters, for the dataset for patient number 9, are shown. Then, for each dataset, only the cluster closer to the real apex of the pyramid (determined by visually inspecting a 3D volume rendering of the dataset) was selected. The parameter combinations of the points belonging to this cluster were determined. An intersection among all the sets corresponding to the parameter combinations producing points in the chosen cluster for the five patients was then performed.

The final parameter combinations resulting from this selection are reported in Fig. 9, in the parameter space. Varying par0, keeping the other parameters fixed in different configurations, did not show any influence on this study, so it was not reported.

The first important observation is that the parameter values initially selected for our implementation are among the valid combinations for a correct determination of the pyramid's apex. It is also interesting to notice that the algorithm is robust with respect to the choice of these parameters: in Table 5 the average statistical values referred to the selected clusters are reported, showing that the size of these clusters is one order of magnitude smaller than the shifts tested in Table 3. This means that every variation of the parameters generating the points within the cluster will produce a final shift in the position of the target much smaller than what already found acceptable previously.

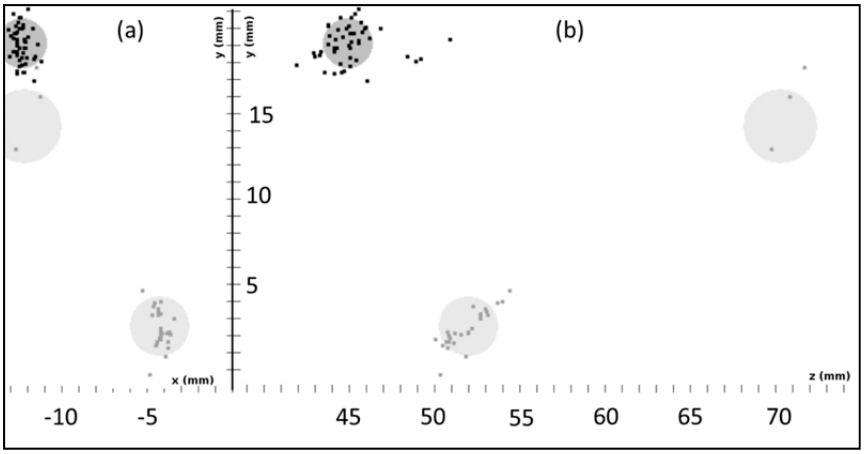

Fig. 8: Geometrical distribution of the pyramid's apex position for patient 9 dataset and for each combination of parameters (Table 4); in (a) projection on the axial plane, in (b) along the sagittal plane. Three clusters were recognized for this patient using the algorithm prosed by (Dunn, 1974); the dimension of the cluster chosen as closer to the actual pyramid's apex are very small with a radius slightly larger than 1 mm.

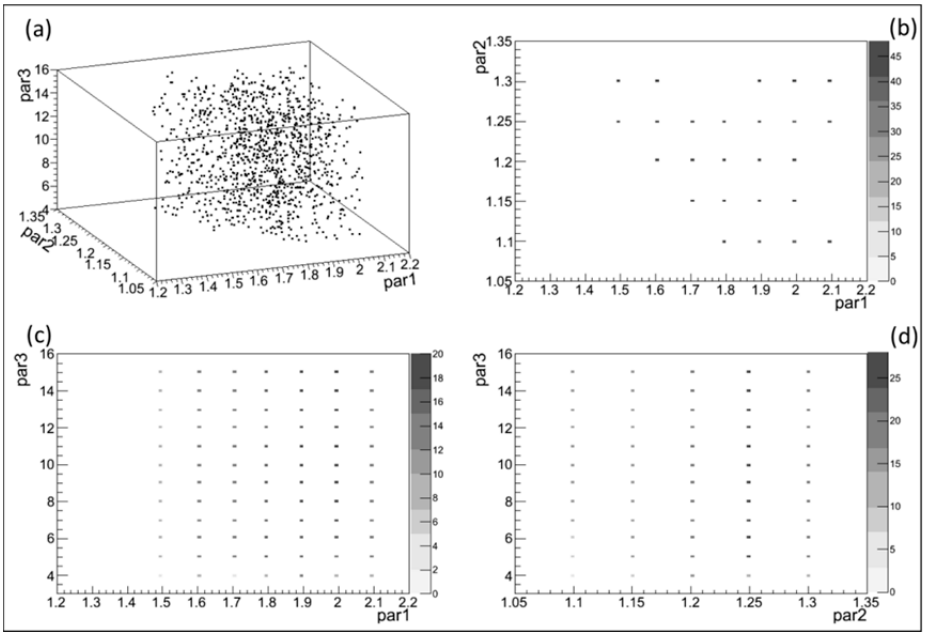

Fig. 9: Distribution in the parameters' space of the points related to the combinations reported in Table 4, belonging to the chosen cluster for all the 5 analyzed datasets. In (a) the 3D plot; in (b)-(d) the three projections on the paired parameter planes. The values initially used, after trial-and-error investigation, for σ_0 and k (par1 and par2, respectively) were 1.7 and 1.2: this pair is among the valid ones (upper right plot). It is also proven to be robust: it is in fact surrounded by other valid values, so also small variations in the picked values would still give reliable results.

Table 5: Mean distance from the chosen cluster center of the apex position distribution; root mean square (RMS); maximum distance from the cluster center; and distance of the apex positions used in Table 2 from the cluster center position.

Patient N	Mean distance [mm]	RMS [mm]	Maximum distance [mm]	Distance of apex position from the average position [mm]
5	2.2	2.6	6.9	1.8
7	1.0	1.2	2.6	1.9
9	1.0	1.1	2.0	1.1
11	1.1	1.2	2.3	1.6
14	1.1	1.4	4.3	1.7

6.4 Discussion

The average shift shown in Table 2 matches to a good extent the discrepancies reported by (Johnston *et al.*, 2008), Table X, between US imaging and other verification imaging modalities. These discrepancies can possibly be explained by the SOS aberration, in good agreement with recent findings of our group (see, for example, (Fontanarosa *et al.*, 2012a)). The differences in shift values are almost entirely due to the relative importance of the amount of fat [1450 m/s (Mast, 2000)] tissue and urine content in the bladder [1520 m/s (Verma *et al.*, 2005)] with respect to muscle tissue [1580 m/s (Mast, 2000)] overlying the prostate. Thus, it is not a linear function of the depth of the target (along the US transducer line of view), despite it being a cumulative effect, because of the possible compensations occurring between these tissues with very high and very low SOS values. Probe pressure is not known for being a significant reason for shifts change, mainly as the prostate scanning protocols in RT are very strict and require as little pressure and as little tissue displacement as possible.

It is important to highlight that the LOVs reconstruction presented in this work does not recreate the physical LOVs used by the 3DUS system to produce the US volume. These are almost impossible to derive from the final US volume as the construction algorithm used by manufacturers is generally proprietary. Strictly speaking, the LOVs reconstructed in this work are the ones that would generate the given US volume if the information contribution received by the transducer, while receiving along a specific direction, only originated from that direction, and not from the entire FOV. US systems assume that, even though information from other directions is present, the entire signal received derives from the direction along which it is received. This assumption creates some small errors and aberrations which affect the final accuracy of the image reconstruction; it is evident though that, despite this issue, the US images can be considered geometrically sufficiently reliable. Thus, since the geometric reconstruction of internal structures is reliable and since the SOS aberration

correction must be applied along the LOVs, it is most convenient to work with these virtual LOVs. Moreover, our previous work shows clearly that the SOS aberration correction is robust with respect to small variations in tissue thicknesses and substitutions (Fontanarosa et al., 2012b), as the ones generated by this issue.

The sensitivity analysis of the algorithm to variations of the empirical parameters used proved its robustness. Within the ranges determined in this article, their change does not significantly affect the position of the origin of the pyramid. The variations induced in the latter are always an order of magnitude smaller than those induced in the study reported in Table 3.

Differently from other fields, in radiotherapy US systems are used quantitatively to measure the absolute position of structures to ensure correct alignment with radiation beams. It is thus important to correct for SOS aberrations, which could be a source of systematic errors, limiting the accuracy of the measurements.

The availability of a co-registered CT scan in some 3D US systems for radiotherapy positioning applications allows for the creation of a SOS map from the density distribution of the imaged materials through an empirical relationship. This map can be used to correct SOS aberrations using a 3D algorithm that was presented in this work. Issues related to the applicability of a CT scan at the simulation stage at later times to derive SOS corrections are fully discussed in another article (Fontanarosa *et al.*, 2012b) and play no role in the work presented here.

6.5 Conclusions

The SOS algorithm presented is a 3D extension to convex transducers of a 2D version previously developed for linear transducers by (Fontanarosa *et al.*, 2011). The algorithm was tested on a set of 3D US and co-registered CT images scanned on a pelvic multi-modality phantom, with three different liquids on top; the correction restores a match between the CT and the US scans identical to what would be obtained through a manual registration.

The test on clinical cases of prostate cancer patients shows an average shift of the prostate center position of 3.1±0.9 mm, which is in excellent agreement with published work ((Johnston *et al.*, 2008) and (Fontanarosa *et al.*, 2012a)). In particular, our results confirm that the reported discrepancies between US and other IGRT methods, both in direction and magnitude, (see for example (Johnston *et al.*, 2008)) can be largely explained by SOS aberration.

Acknowledgments

The authors wish to thank all staff involved in collecting the 3D US datasets at MAASTRO Clinic, at Azienda Ospedaliera "Maggiore della Carità" and at CRO Oncologic

Referral Center. Resonant Medical (Elekta) is thanked for support and discussion, in particular Dr Martin Lachaine.

6.6 References

Al-Nassar Y N, Al-Jalal A M, Khan M A and Al-Kaabi S A 2006 Functional Dependence of Ultrasonic Speed in Water on Salinity and Temperature. (NDT.net)

Brascho D J 1977 Tumor localization and treatment planning with ultrasound *Cancer* **39** 697-705

Carson P L 1978 Biomedical ultrasonics. By P.N.T. Wells, Ph.D., Academic Press, Inc. London, Copyright 1977. 635 pages. $46.90 *Journal of Clinical Ultrasound* **6** 126-7

Christiaens M, Sutter B D, Bosschere K D, Campenhout J and Lemahieu I 1999 A fast, cache-aware algorithm for the calculation of radiological paths exploiting subword parallelism *Journal of Systems Architecture* **45** 781-90

Dunn J C 1973 A Fuzzy Relative of the ISODATA Process and Its Use in Detecting Compact Well Separated Clusters *Cybernetics and Systems* **3** 3,32-57

Fischler M A and Bolles R C 1981 Random sample consensus: a paradigm for model fitting with applications to image analysis and automated cartography *Commun. ACM* **24** 381-95

Fontanarosa D, van der Meer S, Harris E and Verhaegen F 2011 A CT based correction method for speed of sound aberration for ultrasound based image guided radiotherapy *Med Phys* **38** 2665-73

Fontanarosa D, van der Meer S and Verhaegen F 2012a Magnitude of speed of sound aberration corrections for ultrasound image guided radiotherapy for prostate and other anatomical sites. *Med Phys* **In press**

Fontanarosa D, van der Meer S and Verhaegen F 2012b On the significance of density-induced speed of sound variations on US-guided radiotherapy. *Medical Physics* **Under review**

Freeman T 2011 Ultrasound tackles radiotherapy guidance. http://medicalphysicsweb.org/cws/article/-opinion/47249) pp Medical Physics Web - Available online

Grosso V A D and Mader C W 1972 Speed of Sound in Pure Water *The Journal of the Acoustical Society of America* **52** 1442-6

Johnston H, Hilts M, Beckham W and Berthelet E 2008 3D ultrasound for prostate localization in radiation therapy: a comparison with implanted fiducial markers *Med Phys* **35** 2403-13

Kim H, Edward B, Saiful H M and Sushil B 2011 Ultrasound Imaging - Medical Applications. In: *Clinical Application of Ultrasound Imaging in Radiation Therapy,* ed P O Minin: (InTech)

Kleis S J and Sanchez L A 1990 Dependence of speed of sound on salinity and temperature in concentrated NaCl solutions *Solar Energy* **45** 201-6

Ling C C, Yorke E and Fuks Z 2006 From IMRT to IGRT: frontierland or neverland? *Radiother Oncol* **78** 119-22

Lowe D G 2004 Distinctive Image Features from Scale-Invariant Keypoints *Int. J. Comput. Vision* **60** 91-110

Mast T D 2000 Empirical relationships between acoustic parameters in human soft tissues *Acoustics Research Letters Online* **1** 37-42

OndaCorp 2003 Acoustic Properties of Liquids. Onda Corporation (http://www.ondacorp.com/images/Liquids.pdf)

Siddon R L 1985 Fast calculation of the exact radiological path for a three-dimensional CT array *Medical Physics* **12** 252-5

Svalbe I and Jones R 1992 The design of morphological filters using multiple structuring elements, Part I: openings and closings *Pattern Recognition Letters* **13** 123-9

Verma P K, Humphrey V F, and Duck F A 2005 Broadband measurements of the frequency dependence of attenuation coefficient and velocity in amniotic fluid, urine and human serum albumin solutions *Ultrasound in Medicine and Biology* **31** 1375–1381

Wang L, McCarthy K L and McCarthy M J 2004 Effect of temperature gradient on ultrasonic Doppler velocimetry measurement during pipe flow *Food Research International* **37** 633-42

Webb S and McQuaid D 2009 Some considerations concerning volume-modulated arc therapy: a stepping stone towards a general theory *Physics in Medicine and Biology* **54** 4345

Wild J J 1950 The use of ultrasonic pulses for the measurement of biological tissues and the detection of tissue density changes *Surgery* **27** 183-99

Xing L, Thorndyke B, Schreibmann E, Yang Y, Li T F, Kim G Y, Luxton G and Koong A 2006 Overview of image-guided radiation therapy *Med Dosim* **31** 91-112

Quantitative ultrasound imaging applied to segmentation

Chapter 7

Automated CT-US cross-modality 3D contouring algorithm for prostate

Denis Ermacora
Silvia Pesente
Francesco Pascoli
Sebastian Raducci
Roberto Mauro
Imad Abu Rumeileh
Frank Verhaegen
Davide Fontanarosa

Submitted to Physics in Medicine and Biology

Abstract

Segmentation of targets and organs at risk (OAR) in patient images used in radiotherapy (RT) is a very delicate task as errors in this phase propagate systematically through the whole treatment course. Moreover, it is becoming more and more time demanding since advanced treatment techniques, such as intensity modulated radiation therapy (IMRT), were introduced. To improve workflow efficiency, semi-automated contouring techniques were implemented in treatment planning systems, based on computed tomography (CT) imaging datasets. But information from this imaging modality is not always sufficient to provide the necessary accuracy, even for manual contouring. This led to the need of using multiple imaging modalities in this process. Until now, no real automated multi-modality segmentation algorithm was available. In this work we introduce a three dimensional (3D) cross-modality automated image segmentation algorithm based on CT and ultrasound (US) images. The algorithm can be trained and optimized on the characteristics of specific patient samples, becoming increasingly accurate with the size of the sample. We cross-trained and cross-tested the algorithm on sixteen prostate patients. The conformity between the automatically segmented prostate contours and the contours manually outlined by an expert physician on the CT-US fusion was assessed using the Mean Distance to Conformity (MDC). When only the CT scans were used the average MDC value was 4.5 (±1.7) mm; when also the US scans were considered, both the average and the standard deviation were reduced to 3.9 (±0.7) mm. In four cases, the MDC was above 5 mm for the segmentation on CT alone (up to 9 mm). In all of these cases the addition of US information reduced the MDC to 4.1 mm or less. The fully automated cross-modality algorithm provided therefore contours that always matched the manually outlined references.

7.1 Introduction

Cancer Research UK (http://www.cancerresearchuk.org) estimated that about 900,000 men worldwide were diagnosed with prostate cancer in 2008, accounting for almost one in seven (14%) cancers diagnosed in men. Radiotherapy (RT) is one of the primary treatment modalities for prostate cancer patients. An essential step in RT treatment planning process is the definition of the regions to be treated and of the organs at risk (OAR) to be spared. Segmentation (or contouring) of structures (regions of interest, ROI), in medical images is used to prepare radiation treatment plans, and to position the patient correctly in the radiation beams in image guided radiation therapy (IGRT) [1], [2]. Integration of imaging information from different modalities may help to segment structures that otherwise could not be detected on a single modality. In particular, for prostate, manual segmentation is a tedious task, prone to inter and intra observer variability. Automatic segmentation of anatomical structures from different imaging modalities could help reduce this variability and contouring time.

Recently, two-dimensional (2D) and three-dimensional (3D) prostate segmentation state of the art methodologies were reviewed [3]. In this work, the most common methods were classified into the following categories: contour- and shape-based methods; region-based methods; supervised and un-supervised classification methods; and hybrid methods. For prostate segmentation based on US scans, most of the algorithms previously developed only segment structures in 2D [4-6]. For 3D image datasets, contours are created on each slice separately. This leads to a partial use of the information provided by the whole volume and is likely to produce errors. In fact, even when the boundary curve obtained as the result of a single slice 2D segmentation is used as the starting configuration to propagate and adapt to nearby slices (e.g. [7]), the error introduced at each step could propagate to the following steps and compromise the entire result.

CT imaging is the most widely used modality for segmentation in RT because it is required for dose calculation and therefore always available prior to treatment planning. Several automatic segmentation algorithms [2,8-11] have been implemented for CT images. They typically show low contrast between soft tissues and e.g. for prostate this means that the borders between bladder, prostate and seminal vesicles are often very difficult to distinguish. This leads in most cases to an intrinsic limitation in the features that can be used for a correct automated segmentation procedure.

The aim of the algorithm here presented is to make simultaneous use of the whole 3D information available from each of the imaging techniques considered, CT and US; and, at the same time, to retrieve as much information as possible from the combination of the two imaging modalities to use in the segmentation process.

7.2 Materials & Methods

7.2.1. Datasets and instrumentation

Sixteen clinical prostate cancer cases were provided by three different hospitals: one from MAASTRO Clinic (Maastricht, the Netherlands), four from Azienda Ospedaliera "Maggiore della Carità" (Novara, Italy) and eleven from CRO Oncologic Referral Center (Aviano (PN), Italy). For all of them, co-registered CT and 3DUS image datasets were available. All the patients were scanned with Clarity™ 3DUS Systems (Elekta, Stockholm, Sweden). These systems contain US stations equipped with optically tracked US probes: reflective markers are attached to the probes to track their 3D position and orientation during scanning, using an infrared camera. The position tracking components are used to reconstruct a 3DUS image, relative to the coordinate system of the room. The scanning devices used convex transducers (type C5-2/60, center frequency 3.5MHz, Sonix Series, Ultrasonix Medical Corporation, Richmond, BC, Canada). Various CT scanners were used (GE Medical System - LightSpeed Plus; GE Medical Systems - ProSpeed Plus; Siemens - Sensation Open). For each patient the prostate was manually segmented by an expert qualified clinician of the CRO hospital using both the CT and the US images. It is important to highlight that segmentation on US of deep seated organs such as the prostate, scanned trans-abdominally, can be considered quantitatively accurate in this study because, prior to outlining the contours, a speed of sound (SOS) aberration correction was applied. It was previously showed [31,32] that important errors (up to 4 mm or more) can occur, and that the implemented correction restores a correct distance measurement [12,33].

7.2.2. Data representation

7.2.2.1. Input data

Co-registered CT and US images were exported from the Clarity system via the DICOM protocol. The Clarity software provides clinical US volumes re-sliced and re-sampled along the CT scan axial planes. The proposed segmentation algorithm works on 3D volumes while the exported data are organized in axial slices. A procedure previously developed by us [12] was therefore used to obtain a 3D volume (Volume) from the original planes.

A convenient syntax to represent patient imaging data is:

$$Patient^{NM} = \{Volume_m,\ 0 < m \leq NM\} \tag{7.1}$$

with NM the number of imaging modalities.

The p-th testing/training case for target segmentation can thus be described as:

$$TPatient_p^{NM} = \{Patient_p^{NM}, Reference_p\} \tag{7.2}$$

where $Reference_p$ is a manually segmented contour for the target.

It must be noted that, similar to the volume data, also the reference contour data should be preprocessed converting them from the original representation (a DICOM RT contour sequence [13]) to the data structure used by the segmentation algorithm (defined in section 7.2.2.2.). In the remaining sections $Reference_p$ refers to the latter representation.

A testing or training set can then be expressed as:

$$TDataSet_{NP}^{NM} = \{TPatient_{p}^{NM},\ 0 < p \leq NP\} \tag{7.3}$$

with NP number of cases within the set.

According to the previous definitions, the set of volumes used in this work can be expressed as $TDataSet^{2}_{16}$ with:

$$Patient^{2} = \{Volume_{CT}, Volume_{US}\} \tag{7.4}$$

7.2.2.2 Polar Defined Convex Volume

To properly describe the 3D region suitable to represent the treatment target, a data structure was introduced with the following characteristic: it should show surface concavities only along the radial direction in a spherical coordinate system, with the origin in the center of mass (COM) of the region (as in the left panel of Figure 1).

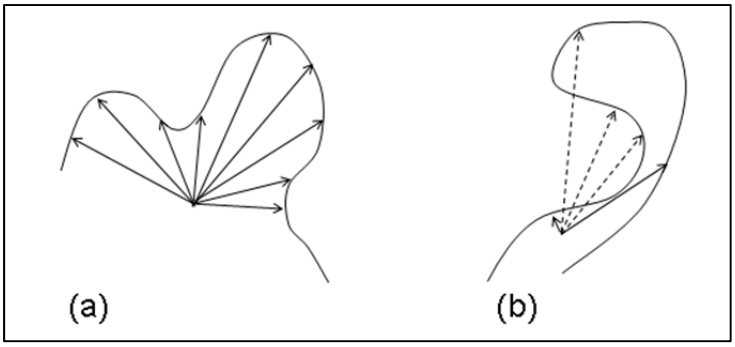

Figure 1: Two examples in 2D projections on planes containing the centers of mass of segmented regions.In a spherical coordinate system with the origin located in the centre of mass of the region, in (a) every possible segment along the radial direction crosses only one time the surface; and in (b) multiple crossings happen. The data structures used in this work must be of the (a) type, in 3D, meaning the property must hold true for every possible plane containing the COM.

In this representation the region to contour is identified by a collection of points on its surface. These points are identified by vectors with origin in the centre of mass of the region and length defined by the distance from the origin to the surface. These vectors should be spaced with a uniform angular sampling. This constraint avoids the loss of

descriptive accuracy of different surface areas of the target during the segmentation process.

This data structure will be referred to as Polar Defined Convex Volume (PDCV) and consists of the following sub-structures (see Figure 2):

- A reference coordinate system S with origin **o**(x,y,z), positioned in a point which satisfies the characteristics described previously, in particular a convex description of the surface.
- A fixed base of unit vectors (versors) $\mathbf{v}_i$(x,y,z) evenly distributed on the surface of a unit sphere (the procedure for the generation of these versors is described in Appendix A1).
- A list of positive real scalar coefficients c_i, associated with the versors $\mathbf{v}_i$, that determine the distance between the origin and the surface points of the region, along each direction.

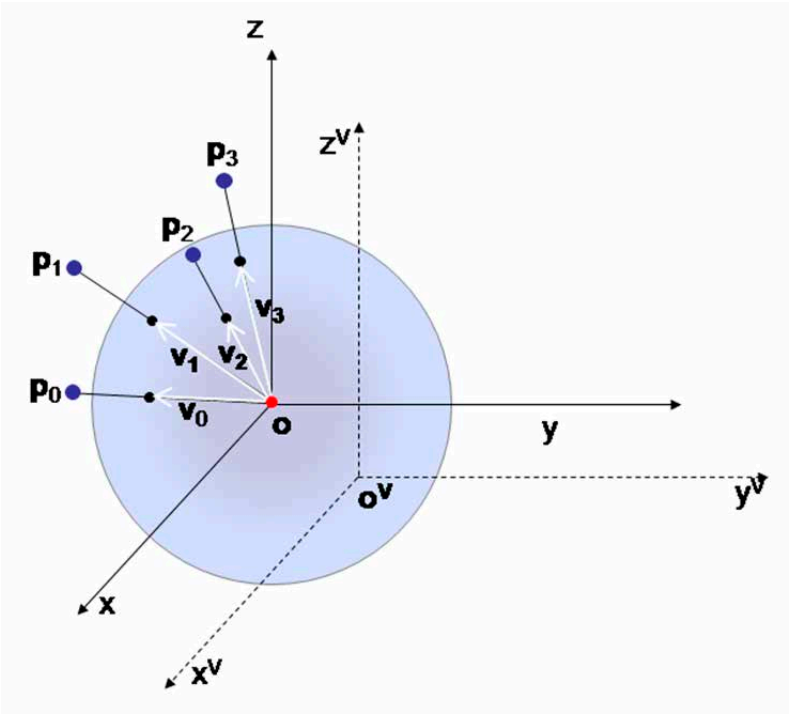

Figure 2: Representation of the surface of the region to contour as a set of vectors (p_i). These vectors have origin in o(x,y,z) and length defined by their intersection with the surface. Their number can vary (see Appendix A1) according to the accuracy with which the surface must be determined, and their directions are uniformly distributed along the solid angle around the origin. In the figure, the origin of the data structure is shown with respect to the origin of the original imported DICOM image datasets o^v(x,y,z), and some versors uniformly spaced are shown.

The PDCV is therefore defined by the collection of the vectors:

$$\mathbf{p}_i = c_i \mathbf{v}_i \tag{7.4}$$

which locate the points on the surface of the region along the versor $\mathbf{v}_i$, in the reference system S.

In the original reference system S^v, defined by the imported DICOM dataset volume (dashed lines, Figure 2), the vectors are defined as:

$$\mathbf{p}_i^v = \mathbf{o} + c_i \mathbf{v}_i \tag{7.5}$$

To define the shape of the PDCV it is therefore only required to change the scalar coefficients c_i, while its global repositioning requires only the update of the origin **o** with respect to $\mathbf{o}^v$.

The PDCV structure supports also important types of derived Look-Up Tables (LUT) such as the calculation of the normal direction to the surface.These were pre computed during the initialization phase to increase the process speed (for a detailed description, see Appendices A2 and A3).

7.2.3. Workflow

The algorithm is composed of a first initialization phase followed by an iterative phase aimed at producing a PDCV as similar as possible to the features recognized as the border of the target. All the phases are completely automated.

7.2.3.1. Initialization

During the initialization a PDCV with a spherical shape (hereafter indicated as PDCVinit) is automatically positioned near the area of interest. In the case of US co-registered on CT, the main bone structures are automatically found beforehand using the CT scan information by means of the Maximally Stable Volumes (MSV) algorithm [14].Then the spherical PDCVinit is positioned between the femoral heads. The radius is determined by an expansion procedure limited by the same bone structures.

7.2.3.2. Iteration

In the iterative phase, at each step the shape of the PDCV (through the c_i parameters, Eq. 5) and the center (**o**, Eq. 6) are changed; so at the n^{th} iterative step the PDCV origin is updated as follows:

$$\mathbf{o}[n+1] = \mathbf{o}^{transl}[n] \tag{7.7}$$

where:

$$\mathbf{o}^{transl} = (1-\delta)\mathbf{o} + \delta \underline{\mathbf{o}}^{transl} \tag{7.8}$$

and $\underline{\mathbf{o}}^{transl}$ is the estimate for the new COM after the translation following the change in shape of the PDVC (as described in detail in the following sections).
For the coefficients:

$$c_i[n+1] = c_i^{shape}[n] \tag{7.9}$$

where:

$$c_i^{shape} = (1-\gamma)c_i^{smooth} + \gamma \underline{c}_i^{shape} \tag{7.10}$$

$$c_i^{smooth} = (1-\beta)c_i^{feat} + \beta \underline{c}_i^{smooth} \tag{7.11}$$

$$c_i^{feat} = (1-\alpha)c_i + \alpha \underline{c}_i^{feat} \tag{7.12}$$

and $\underline{c}_i^{feat}$, $\underline{c}_i^{smooth}$, and $\underline{c}_i^{shape}$ are the estimates for the new values of the coefficients after the search and adaptation to the image features, after smoothing and after conforming to the statistical shape derived from the manually contoured dataset, respectively.α, β, γ, $\delta \in$ [0,1] are weight parameters normalizing the iterative equation; α, β, γ, δ may vary at different time points of the global segmentation process: we will therefore call α^0, β^0, γ^0, δ^0 the initial values, and α^d, β^d, γ^d, δ^d the values of their relative changes, that contribute to modify the current values of parameters at each iterative step,as follows:

$$\alpha^{n+1} = \alpha^n * \alpha^d, \beta^{n+1} = \beta^n * \beta^d, \delta^{n+1} = \delta^n * \delta^d, \gamma^{n+1} = \gamma^n * \gamma^d. \tag{7.13}$$

Therefore the configuration of the iterative phase of the algorithm can be defined as the set:

$$Config := \left\langle \alpha^0, \beta^0, \gamma^0, \delta^0, \alpha^d, \beta^d, \gamma^d, \delta^d \right\rangle \tag{7.14}$$

that univocally identifies the forces that contribute to the change of PDCV in all the iterative steps.

The whole procedure is described in detail in the following sections and a flowchart of the proposed segmentation method is shown in Figure 3.

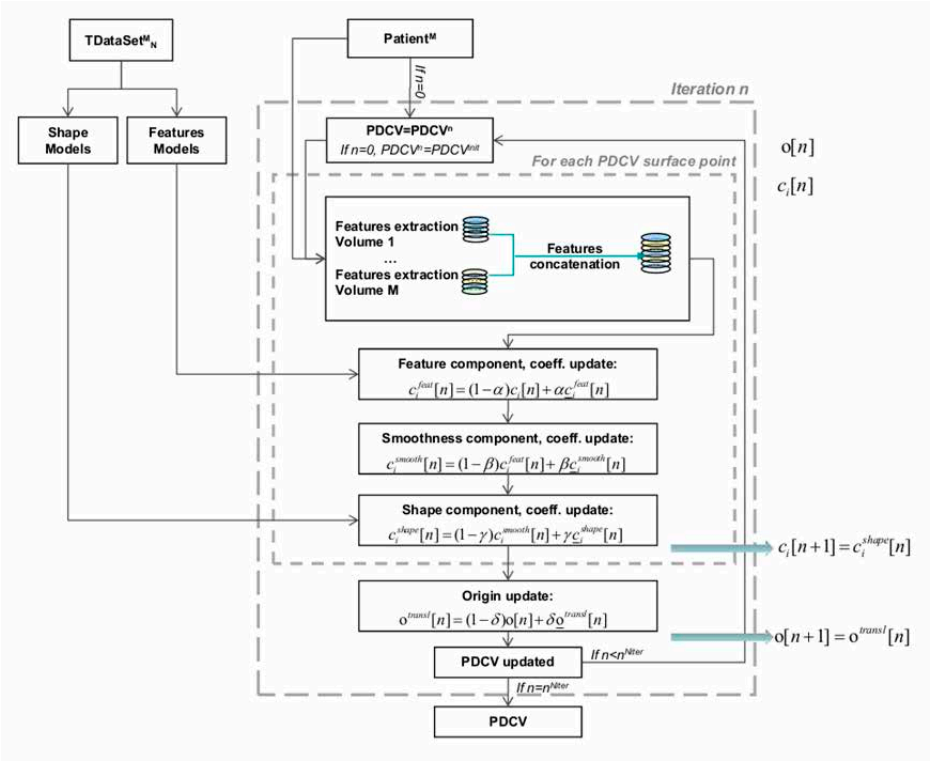

Figure 3: Flowchart of the two phases (initalization phase and iterative phase) of the proposed segmentation method.

7.2.3.3. Features

The first iteration component uses the data available from the NM volumes associated with the case ($Patient^{NM}_{p}$) under analysis, to update the coefficients c_i so that surface points $\mathbf{p}_i^v$ and the areas adjacent to them show characteristics as close as possible to the target border.

The reference model describing the features of the target border can be generated automatically by any training set whose elements $TPatient^{NM}_{p}$ have a $Reference_p$ expressed in PDCV form.

7.2.3.3.1. Features Extraction

There are two major demands that the feature extraction mechanism must meet:

- direct use of 3D data,
- multimodality approach

In order to meet these, two different transformations are applied:

- geometrical mapping from 3D to 2D,
- transformation from data to features space.

7.2.3.3.1.1. Geometrical Mapping from 3D to 2D

The idea is to give a 2D description of the 3D problem. The approach currently used in the Clarity system (based on [15]) searches the 2D axial projections of the US volumes for the features corresponding to the prostate borders. Then it extrapolates to 3D reconstructions.This procedure reduces the accuracy of the procedure, as real 3D gradients are not considered. In this work, the whole 3D data are used. To explain the procedure, the 2D case is first considered: in the CT and US images in Figure 4 (Figure (a) and Figure (d)), from an initial structure (in this case the circle in light gray) the directions normal to the surface are identified (the small segments irradiating from the structures) and along each of those directions the gray levels are sampled and recorded. The amount of samples toward the internal and the external direction from the initial structure can be customized depending on the accuracy required. Then these levels are reported along columns maintaining the order in which they were recorded, from left to right. The final figure created is a stripe as the ones plotted in Figure 4(b) and Figure 4(e) for US and CT scans respectively. At the end, normalization is also performed to obtain an active background with the invariance properties necessary for a proper use of the algorithm (see Appendix C for details).

This transformation was adapted to the 3D case using the 3D directions normal to the surface for each point on the PDCV; since no natural order is now provided, as opposed to the 2D case, specific NLUTs are used to create the neighborhood schemes (see Appendix A2 and Appendix C for more detailed description of the procedure).

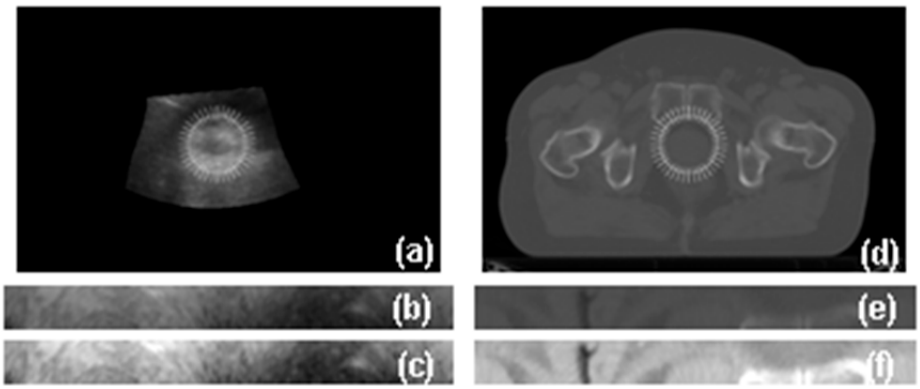

Figure 4: (a), (d) US and CT Volumes; **(b)**, **(e)** the stripes extracted and **(c)**, **(f)** results of global normalization applied to them (Appendix C). The current PDCV border section is shown as a solid circular line. The extension of the stripe extracted is represented by the normal segments.

7.2.3.3.1.2. Transformation from Data to Features Space

The active background, produced as described in the previous section, is then used for the search of locations that appear as similar as possible to those on the target border. The information is still separately extracted from the two modalities and thus cannot be used directly in this estimate. The fundamental step in solving this issue is the reduction of this compound information to a common space of features. The features extracted must be generic enough to be meaningful for each modality and, at the same time, as much distinctive as possible to characterize structures that could be present on or around the border of the target. To this end we have chosen, similarly to what introduced for example in [5,16], the Gabor features [17], that were proven to be good descriptors for both edges and blobs. Edges are defined as points in a digital image at which the image brightness changes sharply. Blobs instead are the points which show some similarities with respect to surrounding areas. Specifically we used a monodimensional (computed along the surface normal direction of the PDCV) multiscale Gabor Detector. To further characterize every point of the active background with features that represent not only structures present on its location, but also in locations close to it along the normal to the PDCV, we introduced the concept of topological multiplicity: this associates to each point **u** (**$u=u_0$** in 5) of the active background also features extracted from points at fixed distances to it.

Figure 5: For every point $u=u_0$ in a stripe, the concept of topological multiplicity implies that also points at fixed distance (u_{-2}, u_{-1},u_{+1}, u_{+2}) are considered for features extraction.

The adaptation to multimodality is implemented by concatenating features extracted for each point not only on the specific modality where the point belongs (e.g. CT). Features are extracted also from the correspondent points (in space) on the other modalities available (in our case, e.g., US). The characteristic vector for the point **u** of the active background, defined feature vector **fv**,can therefore represent different sized edges and blobs present not only over **u** but also in its vicinity from all the modalities, and inter-relate them. The set of these vectors forms the space of the features {$\mathbf{fv}_i$} (see Appendix D1 for more formal specification and further details).

7.2.3.3.2. Model and Training

In the training phase, for each case $TPatient^{NM}_{p}$ the target boundary points are identified from the corresponding contour dataset $Reference_p$, represented in PDCV form. The **fv** are extracted for these points and inserted in the training space of the features $\{\mathbf{fv}_i\}$. From this set, since the Gabor filter is scale invariant, a direct comparison between the different $\mathbf{fv}_i$ is possible and an average vector $\mathbf{fv}^{avg}$ can be calculated. A metric can then be derived (as described in Appendix D2) with the Mahalonobis Distance [18] $Dist^{model}$ which measures the deviation of a generic **fv** from $\mathbf{fv}^{avg}$, taking into account variances and covariances of vector components in the training set. The trained model is composed by $\mathbf{fv}^{avg}$and the metric. If a larger and more complex training dataset is available the simple linear training/prediction method used in this work can be easily replaced with the use of the well-known Support Vector Machine (SVM) methodology, which can describe the true positives clusters in the training set more accurately. A suitable implementation is described in [19].

7.2.3.3.3. Prediction and Update

During the iterative phase, an estimation is provided of the shift that must be applied to each point of the surface of the current PDCV, moving it to the location of maximum conformity with the trained model. In the first step, the features are extracted from each point **u** of the active background using the current PDCV. Then for each of these points the prediction function $Dist^{model}(\mathbf{fv})$ is applied to the **fv** associated with **u**. The resulting values are used to fill a mask of conformity PI^{mask} that has the same dimensions as the stripes of the active background. The PI^{mask} provides a concise representation of how much the data appear similar to what is expected for the border of the target, according to the trained model. As each column u of PI^{mask} corresponds to a specific location $\mathbf{p}_u = c_u\mathbf{v}_u$, on the surface of the current PDCV and each row v reflects the normal displacement from the boundary, for each column the vertical coordinate $v_{min}(u)$ was selected such that the value PI^{mask} ($\mathbf{u} = (u,v)$) was a minimum over the column. Using the reverse mapping of coordinate v from the stripe space to the normal displacement v' in the original 3D space (see Appendix C), the estimated increment for the coefficient c_u associated with point $\mathbf{p}_u$ was calculated as the projection of the vector $v_{min}'(u)\mathbf{l}_u$ positioned along the normal $\mathbf{l}_u$ to the surface in $\mathbf{p}_u$ along the radial direction $\mathbf{v}_u$ (see Figure 6):

$$\Delta c_u = v_{\min}'(u)\mathbf{l}_u \cdot \mathbf{v}_u \tag{7.15}$$

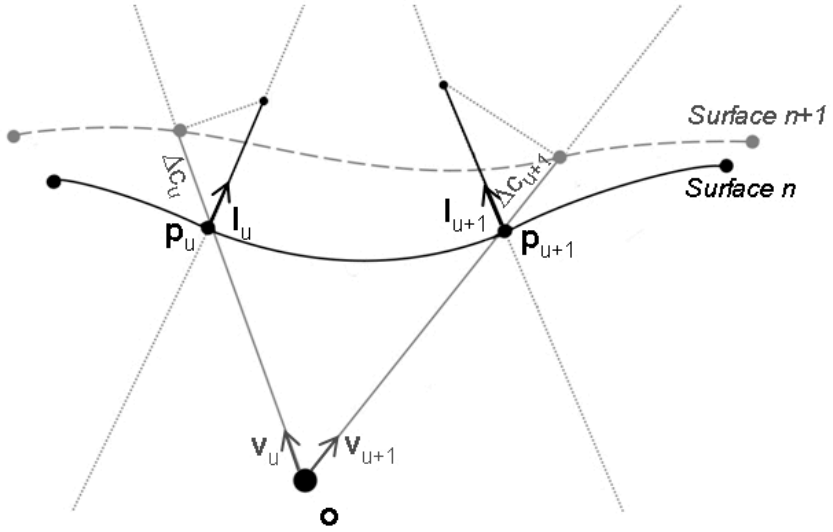

Figure 6: Estimated increment Δc_u for the coefficient c_u calculated as the projection of the vector $v_{min}'(u)l_u$ positioned along the normal l_u to the surface in p_u along the radial direction v_u.

Replacing the index u with i, which refers to the unit vector base of PDCV, we obtained the update estimate $\underline{c}_i^{feat}$ of each coefficient c_i:

$$\underline{c}_i^{feat} = c_i + \Delta c_i \tag{7.16}$$

And, consequently, the coefficient values of the PDCV were updated as in Eq. 7.12 and the following iteration can start.

7.2.3.3.4. Classes specialization

Particular attention should be paid to the fact that, due to the PDCV formulation, points on its surface may exhibit different characteristics depending on the border area they belong to; this can result in a feature vectors set $\{fv_i\}$ composed of significantly different elements, possibly clustering. The solution we adopted is to subdivide the surface of the PDCV in classes or zone-based areas as described in Appendix B and develop a different training/prediction model for each of these classes separately. This extension can then adjust to and differentiate for different surface areas according to the different characterizations of the target border. More details on the implementation of this feature are given in Appendix E.

7.2.3.4. Smoothness

If the target border is visible in the stripe in a specific iteration, the PDCV points will converge to it. But if, especially in the first iterations, it is not yet included, they will

converge independently to local minima, possibly far from each other, resulting in an irregular description of the region surface. Moreover, there might be pairs of surface points in the PDCV structure that, although close together, belong to different surface classes. Even if the features extracted along the normal to the two points are likely to be similar, due to the different models used in the evaluation, it is not granted that for each of these pairs the positions of their minimum in the estimation of conformance to the respective model are close to each other, possibly producing too steep edges on the surface of the final PDCV or, in the worst case scenario, discontinuities.

A solution that handles these two phenomena simultaneously, thus gaining a surface form less irregular and without the presence of false edges, consists in the introduction of an iterative smoothing component operating on the PDCV right after the features component (Eq. 7.11). This component adds a weighted contribution in each point $\mathbf{p}_i^v$ of the surrounding features, where the weight is proportional to the distance from the point relative to the feature component. See Appendix F for the technical details of the implementation.

7.2.3.5. Shape

The smooth iterative component cannot guarantee a sufficient PDCV smoothness without eventually inducing its shape to a spherical configuration. An iterative component that influences the PDCV shape to change toward more appropriate configurations is required.

The shape of the target can be statistically deductible from the manually segmented training set ($\{Reference_p\}$) already adopted for the development of feature models and a reference shape model from the training set can be generated. Details of the implementation are in Appendix G. The shape iterative component acts once more only on the PDCV scalar coefficients c_i^{smooth} resulting from the previous components. The estimate $\underline{c}_i^{shape}$ for each coefficientis the value that should have the i^{th} coefficient to match the same degree of local convexity as the corresponding item in the model calculated from the training set.

7.2.3.6 Origin Update

All the updates to the structure of the PDCV involved only the c_i scalar factors, and therefore the shape and extent of the region represented. But the placement of the region as a whole, described by the origin **o** of the reference system, was not explicitly involved. Moreover, the same origin **o**, as a result of the changes made to the surface points $\mathbf{p}_i$ (induced by c_i coefficients changes), is no longer the COM of the PDCV surface.

It is useful to define the point:

$$\mathbf{COM}^{shape} = \frac{\sum_{PDCV} \mathbf{p}_i^{shape}}{\sum_{PDCV} 1} \tag{7.17}$$

as the COM for the surface points:

$$\mathbf{p}_i^{shape} = \mathbf{o} + \mathbf{v}_i * c_i^{shape} \tag{7.18}$$

calculated after the changes made during the previous iterative components.The deviation vector $\boldsymbol{\mu}$, between the origin and the COM at this stage of the iterative step,can be defined as:

$$\boldsymbol{\mu} := \mathbf{COM}^{shape} - \mathbf{o} = \frac{\sum_{PDCV} \mathbf{v}_i * c_i^{shape}}{\sum_{PDCV} 1} \tag{7.19}$$

That is, as shown in Figure 7, a synthetic representation of the global translational motion of the PDCV toward the target area. The translation of the PDCV was then implemented as the normalized iterative minimization of $\boldsymbol{\mu}$. The consistency of the PDCV structure and the positioning of surface points in local minima are therefore not mandatory during the individual iterations, but only at convergence.
To this end, we defined the estimate of maximum variation allowed to the origin during an iterative step as:

$$\underline{\mathbf{o}}^{transl} = \mathbf{COM}^{shape} \tag{7.20}$$

where $\mathbf{COM}^{shape}$ is computed as in Eq. 16. The center **o** of PDCV was then updated by this component accordingly with Eq. 8; in this case, each step in the update is the corresponding step in the iterative minimization of $\boldsymbol{\mu}$, with δ as weight parameter.

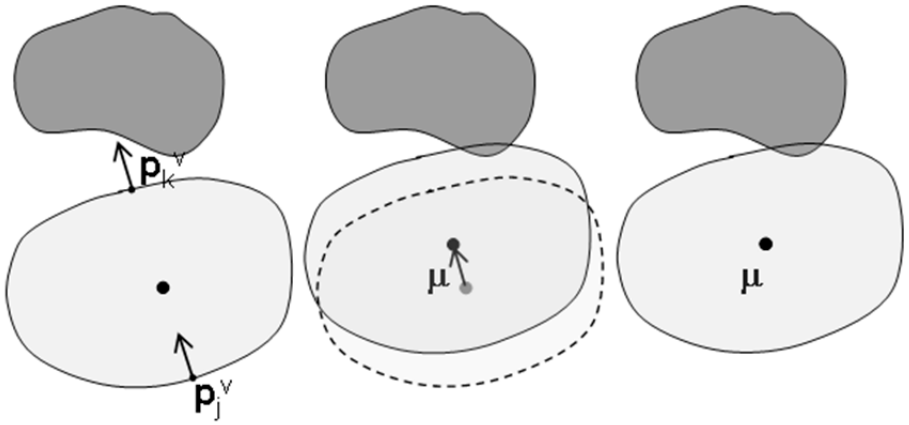

Figure 7: Deviation vector μ between the origin o and the COM at one stage of the iterative step. At this iteration, the PDCV (light grey) shape is changed to conform to the target (dark grey) features and, after that, the origin position is moved accordingly, based on the change of the COM of the structure.

7.2.4. Optimization and Testing

In order to take advantage of all the patient cases available, we used a cross validation approach: given the test case $TPatient^{NM}_{p}$, the set on which the features and shape components were trained was formed by all the remaining patient cases in the testing set:

$$\{ TPatient^{NM}_{t}, 0 < t \leq 16, t \neq p \}. \quad (7.21)$$

7.2.4.1. Metrics

The simplest metric that can be used in assessing the results is the Conformity Index (CI), whose value for each training case $TPatient^{NM}_{p}$ and each configuration takes into account the percentage of overlap between $Reference_p$ and the resulting produced contour (Res_p). A more sophisticated and meaningful metric that takes into account also the conformity between the shapes described by $Reference_p$ and Res_p, is the Mean Distance to Conformity (MDC) [20]. The latter metric was used to estimate the accuracy of the segmentation obtained by the iterative algorithm.

7.2.4.2. Configuration optimization

The first step to optimize the iterative process is the estimation of the best configuration for the iterative parameters $<\alpha^0, \beta^0, \gamma^0, \delta^0, \alpha^d, \beta^d, \gamma^d, \delta^d>$ on the available testing set. Given a basic configuration consisting of a specific selection of the eight parameters:

$$Conf_{base} = \left\langle \alpha^0_{base}, \beta^0_{base}, \gamma^0_{base}, \delta^0_{base}, \alpha^d_{base}, \beta^d_{base}, \gamma^d_{base}, \delta^d_{base} \right\rangle \tag{7.22}$$

a search collection of 3^8 configurations is built: this collection is created considering for each single parameter a search interval Δpar and the derived set of three possible values {par_{base} - Δpar, par_{base}, par_{base} + Δpar}. The optimization process consists in running the iterative algorithm on all the test cases for each configuration in the search collection; this way the segmentation results are obtained with the associated compliance indices MDC. Therefore for each possible configuration in the search collection a numerical value of global compliance can be computed by summing the compliance of each test case for the given specific configuration. In conclusion the best configuration is estimated simply by finding the minimum value among all the MDC computed this way over the search collection of configurations under analysis.

The resulting configuration is:

$$\begin{aligned} &Conf_{opt} = \left\langle \alpha^0_{opt}, \beta^0_{opt}, \gamma^0_{opt}, \delta^0_{opt}, \alpha^d_{opt}, \beta^d_{opt}, \gamma^d_{opt}, \delta^d_{opt} \right\rangle = \\ &\min_{\left\langle \alpha^0, \beta^0, \gamma^0, \delta^0, \alpha^d, \beta^d, \gamma^d, \delta^d \right\rangle} \{MDC\left\langle \alpha^0, \beta^0, \gamma^0, \delta^0, \alpha^d, \beta^d, \gamma^d, \delta^d \right\rangle\} \end{aligned} \tag{7.23}$$

A progressive refinement of this procedure involves its re-application with $Conf_{opt}$replacing $Conf_{base}$ and possibly narrowing the search intervals $\Delta\alpha^0$, $\Delta\beta^0$, …

7.2.4.3. Testing

In the testing phase, the algorithm was run with the optimized parameter configuration (Eq. 21) on all the cases of the testing set $TDataSet^2_{16}$ using the cross validation approach previously described. Then MDC indices were calculated for each case. For sake of completeness, also the CI values were calculated and reported. This procedure was repeated using either a single modality (with CT scan as unique input volume) or multiple modalities (using both US and CT).

This way it was possible to compare the results obtained, checking under what conditions and to what extent the use of multi-modality segmentation can be considered advantageous.

The algorithm was written in the C language and the tests were performed in a Windows 7 64-bit environment on a laptop equipped with a parallelized 8-core 2.3 GHz Intel processor with 16 GB RAM.

7.3 Results

7.3.1. Configuration optimization results

The coefficients obtained by applying the optimization process described in Section 7.2.4.2 on the testing set are shown in Table 1.

Table 1: Coefficent values obtained by applying the optimization process on the available testing set.

α^0_{opt}	β^0_{opt}	γ^0_{opt}	δ^0_{opt}	α^d_{opt}	β^d_{opt}	γ^d_{opt}	δ^d_{opt}
0.40	**0.30**	**0.21**	**0.40**	**0.96**	**0.985**	**1.01**	**0.985**

These results confirm what was previously qualitatively hypothesized, in particular:

- In the initial phase a high degree of freedom in the translation of the COM (δ^0_{opt} = 0.40) as well as a large impact of the features-dependent component (α^0_{opt} = 0.40) if compared with shape normalization (γ^0_{opt} = 0.21) and smoothing (β^0_{opt} = 0.30) is expected. This means that in the early iterations PDCV moves fast toward the target area mainly driven by the features extracted from scanning volumes but not taking too much into account the surface regularity and conformity of the surface shape with the model (iterations from 0 (Figure 8 (a)) to 8 (Figure 8 (b))).
- In a central stage, while maintaining a medium degree of freedom of motion of the COM, the influence of features is increasingly mediated by the constraint on surface regularity (α^d_{opt}= 0.96 vs β^d_{opt} = 0.985) and especially on its shape conformity to the model (α^d_{opt}= 0.96 vs γ^d_{opt} = 1.01). At this stage however, the effect of surface regularity is still greater than the shape conformity because of the starting values of their coefficients β^0_{opt}= 0.30 e γ^0_{opt} = 0.21. This can be interpreted as the need to extend compatibility between the PDCV (which has been translated at least partially on the target area) and the structural characteristics of the target, looking for other areas where relevant features are detected to ensure a good prediction also for those surface points belonging to classes not yet identified (iterations from 8 (Figure 8 (b)) to 32 (Figure 8 (c)) and from 32 to 56 (Figure 8(d))).

In the final stage the freedom of movement of the COM is very low as well as the impact of the smoothing component. The shape conformity component becomes the most important (β^d_{opt}, δ^d_{opt} = 0.985 vs γ^d_{opt} = 1.01). The first observation is justified considering that at this stage the PDCV should have achieved the right placement and does not require further global movement. The second is justified considering that, if during early iterations a rough shape of a spherical type was sufficient for the purposes of global positioning, this phase requires a greater refinement and shapes more compatible with the structural constraints of the target itself. In addition, the shape component provides implicitly a certain degree of surface regularity that is sufficient to counterbalance the local effect of features without the smoothing component (iterations from 56 (Figure 8 (d)) to 104 (Figure 8 (e))).

Finally, in Figure 9, the result obtained is shown (white contour) compared to the manually contoured reference (black contour) along the three main projections for the CT and US images of one patient. The position, extent and shape of the automatic segmentation correspond very well to the manually contoured target, with the only

exception the polar regions (z-axis) that are described by a curved profile in the segmentation result instead of the flat cut present in the manual outline. This is probably only due to the latter having been created slice by slice:therefore discontinuitiesin 3D visualization not pertaining to the real target can be expected.

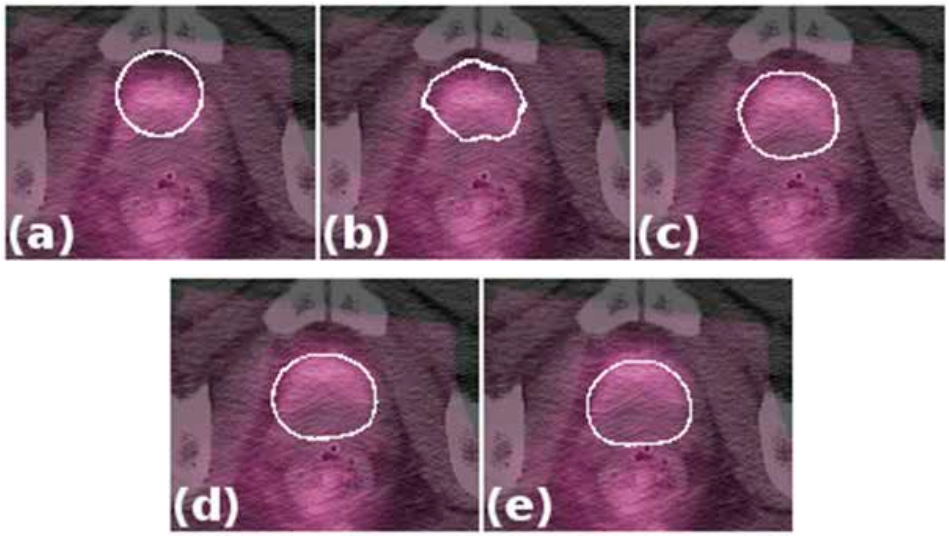

Figure 8: Superposition in an axial projection of the CT scan with the US scan and with the results of the iterative segmentation process at iterations (a) 0, (b) 8, (c) 32, (d) 56 and (e) 104 in the case of optimized configuration.

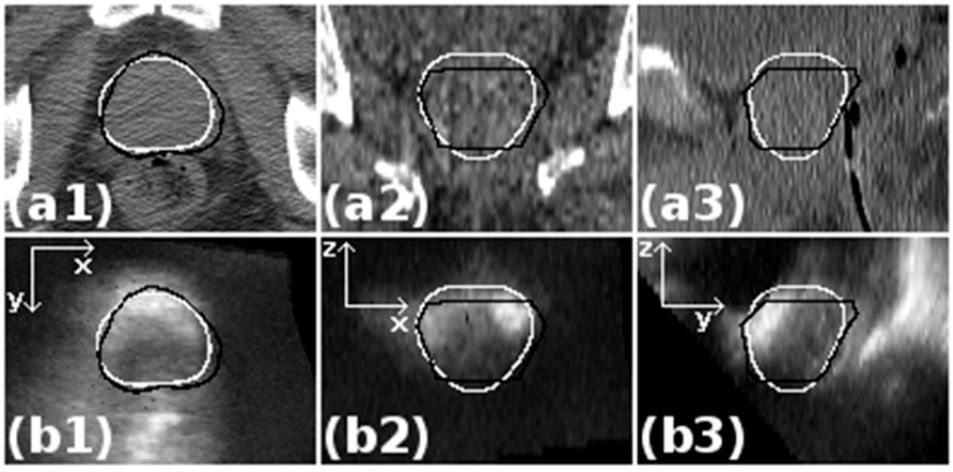

Figure 9: Co-registered (a1)-(a3) CT and (b1)-(b3) 3D US images in (a1), (b1) an axial, (a2), (b2) coronal and (a3), (b3) sagittal projections with superposed the manual segmentation (black contour) and the automated segmentation (white contour) obtained in the case of cross modality imaging (CT and US).

7.3.2. Testing phase results

The average execution time was 8.6 seconds in the multimodality approach (4.9 seconds for single modality). The number of iterations until convergence is about 150 for an average time per iteration of 0.057 seconds. The results obtained in terms of MDC andCIforthe 16 cases of the testing set are compared in Table 2. The MDC and CI indices are reported both for the single modality (CT) and for the multimodality approach (CT+US).

Table 2: For each patient , MDC values were calculated for CT only (second column) and for the combination CT and US (third column). Improvement is defined in the fourth column as $MDC_{CT} – MDC_{CT+US}$. In the remaining columns the CI values are reported with the Improvement defined as CI_{CT+US} - CI_{CT}.

Patient	MDC_{CT} (mm)	MDC_{CT+US} (mm)	Improvement (mm)	CI_{CT}	CI_{CT+US}	Improvement
1	**4.7**	**4.1**	**0.6**	**0.46**	**0.54**	**0.08**
2	**4.7**	**4.2**	**0.5**	**0.51**	**0.60**	**0.09**
3	**2.8**	**3.5**	**-0.7**	**0.82**	**0.64**	**-0.18**
4	**9.0**	**3.9**	**5.1**	**0.30**	**0.68**	**0.38**
5	**4.3**	**4.5**	**-0.2**	**0.59**	**0.51**	**-0.08**
6	**4.0**	**4.4**	**-0.4**	**0.65**	**0.59**	**-0.06**
7	**3.5**	**5.5**	**-2.0**	**0.64**	**0.42**	**-0.21**
8	**4.2**	**3.2**	**1.0**	**0.71**	**0.74**	**0.03**
9	**4.8**	**4.4**	**0.4**	**0.70**	**0.67**	**-0.03**
10	**2.0**	**3.3**	**-1.3**	**0.85**	**0.59**	**-0.26**
11	**4.4**	**3.7**	**0.7**	**0.49**	**0.57**	**0.08**
12	**5.8**	**3.0**	**2.8**	**0.47**	**0.71**	**0.27**
13	**5.7**	**4.1**	**1.6**	**0.42**	**0.66**	**0.24**
14	**3.3**	**3.5**	**-0.2**	**0.68**	**0.70**	**0.03**
15	**6.6**	**4.1**	**2.5**	**0.33**	**0.55**	**0.22**
16	**2.4**	**2.6**	**-0.2**	**0.72**	**0.69**	**-0.03**
Average	**4.5**	**3.9**	**0.6**	**0.58**	**0.62**	**0.04**
Standard deviation	**1.7**	**0.7**	**1**	**0.16**	**0.09**	

From a statistical point of view we can observe that:

- The MDC mean value obtained for cross modality ($\langle MDC \rangle_{CT+US}$ = 3.9mm) is lower than the one obtained using only CT scans ($\langle MDC \rangle_{CT}$ = 4.5mm).
- The MDC standard deviation for cross modality ($\sigma(MDC)_{CT+US}$ = 0.7mm) is considerably lower than the one computed from the results obtained using only CT scans ($\sigma(MDC)_{CT}$ = 1.7mm). This means that the contribution of US compensates the lack

of information that in some cases in CT scans is manifested, making the segmentation process more stable and the whole algorithm more reliable.

A more thorough analysis of the results shows how multimodality improvement is not uniformly distributed among all test cases: it is larger when the segmentation based only on CT is unsatisfactory (see Figure 10). This is due to the complementarity of the data coming from US with respect to data coming from CT. In fact when the segmentation based only on CT gave already good results the additional ultrasound scan does not result in an appreciable change; but when data from the CT are insufficient and segmentation converges far from the right target border, US data provide missing information allowing the algorithm to significantly improve the final result (see Figure 4).

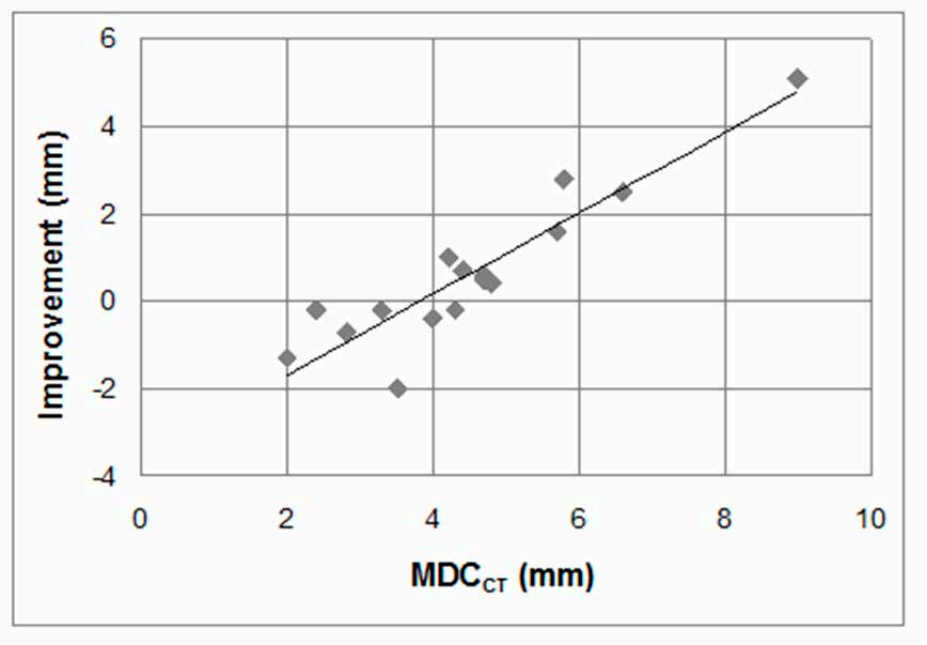

Figure 10: Improvement of MDC value, when both US and CT volumes are used for segmentation, as a function of the MDC values obtained using only the CT volume.

To give a more exhaustive explanation of the possible causes for this behavior the following sections describe in more detail the results obtained in two specific cases that correspond to the worst and the best segmentations based only on CT.

7.3.2.1. Patient n.4

In this particular worst case, the CT-based segmentation produced the largest MDC. Here, the information provided by the US scan provides the best improvement in MDC, from a value of 9.0 mm to 3.9 mm.

The reason can be inferred from Figure 4 that shows the results (white contours) obtained considering only the CT (Figure 4(a1)-(a3)) or both US and CT (Figure 4(b1)-(c3)), individually compared to manual segmentation (black contours), and superimposed to the projections of the CT and US scans along the x, y and z axes. From Figure 4(a1)-(a3) it can be noticed how the CT-based segmentation fails in determining the correct position along the z-axis. Information extracted from the CT scan does not show relevant features along this direction. But the additional data retrieved from the US scan provided the missing information: as it can be seen in Figure 4(c1)-(c3), the bottom surface of the target is clearly visible; the Gabor filters detect the edge features from the US scan and the iterative process produces a correct segmentation identifying the correct location of the inferior surface of the PDCV.

7.3.2.2. Patient n.10

In this case the CT-based segmentation produces the best MDC of the cohort and the addition of US-based information produces a small worsening in MDC, from a value of 2.0 mm to 3.3 mm. Again, the reason can be inferred visually (Figure 5). Here, as opposed to the previous case, the projection along the z-axis is more clear. In this situation the segmentation based on CT is almost perfect (Figure 5(a1)-(a3)). The additional use of US (Figure 5(b1)-(c3)) does not modify considerably the position of the superior and lateral borders of the resulting PDCV, but pulls upwards its inferior side. However this is not due to structural defects of the proposed algorithm, but rather due to the target being too close to the border of the US scan. In fact, the features used by the trained estimator come not only from locations on the surface of the current PDCV but also (due to the multiplicity concept, introduced in section 7.2.3.3.1.2) from several locations along the normal to the surface. So the no-significance area outside the valid US scan has a negative influence on the overall result by keeping the PDCV away from it. The maximum error introduced in this situation cannot exceed the extent of the multiplicity offset (section 7.2.3.3.1.2) that is directly dependent on the feature detector characteristics. In this case the worsening in the inferior target border delineation is just over one millimeter, on average.

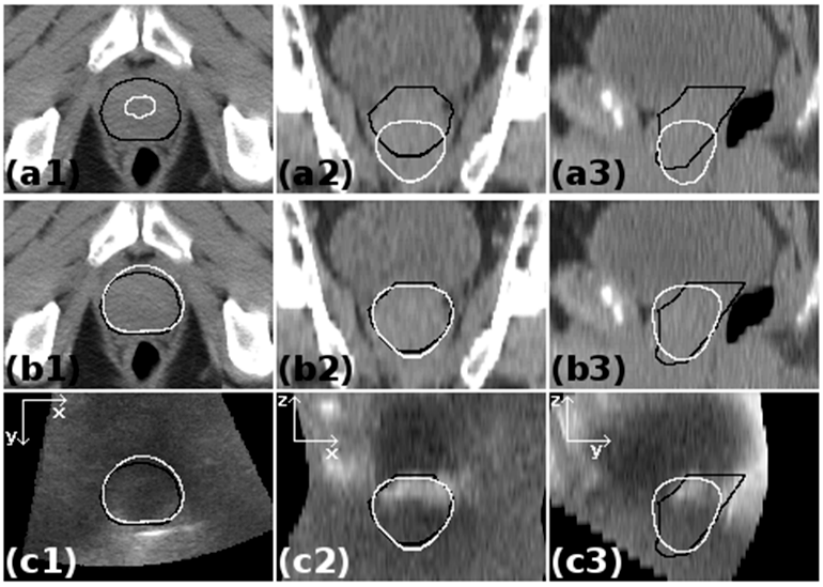

Figure 41: Co-registered CT and 3D US images for the worst case in **(a1)**, **(b1)**, **(c1)** axial, **(a2)**, **(b2)**, **(c2)** coronal and **(a3)**, **(b3)**, **c(3)** sagittal projections with superposed the manual segmentation (black contour) and the automated segmentation (white contour) obtained in the case of **(a1)-(a3)** single modality (CT) and **(b1)-(c3)** cross modality (CT and US) for Patient n.4.

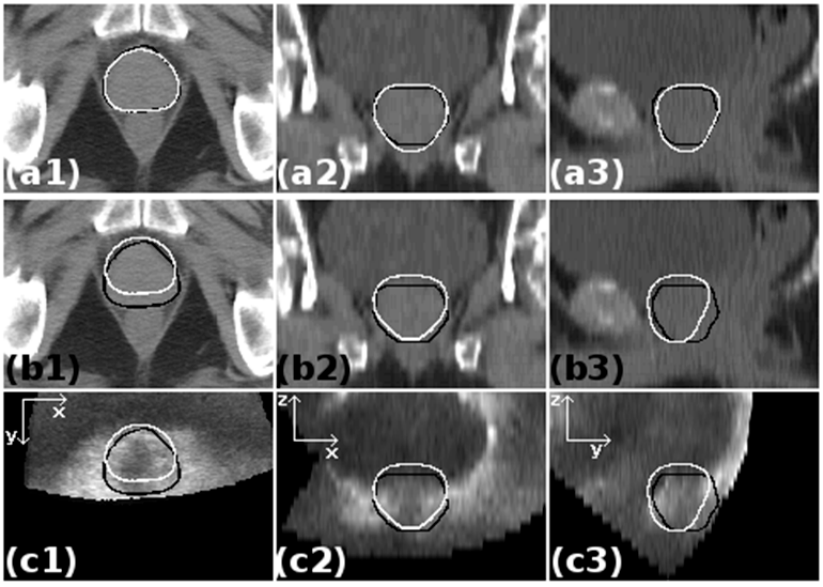

Figure 52: Co-registered CT and 3D US images for the best case in **(a1)**, **(b1)**, **(c1)** axial, **(a2)**, **(b2)**, **(c2)** coronal and **(a3)**, **(b3)**, **c(3)** sagittal projections with superposed the manual segmentation (black contour) and the automated segmentation (white contour) obtained in the case of **(a1)-(a3)** single modality (CT) and **(b1)-(c3)** cross modality (CT and US) for Patient n.10.

7.4 Discussion

Segmentation is increasingly becoming a crucial step of the RT workflow. It is involved not only at the planning stage, where reliable contours can make the difference between a positive or a negative treatment outcome; but also during treatment and post-treatment. There it is fundamental to have accurate comparisons to enable important decisions like adapting the treatment; or to evaluate the outcome, based on target contours before and after the treatment. The number of ROIs required in a modern IMRT or dynamic arc treatment can be very high, up to 40 or more [21]. This can be very time-demanding; so to combine the required accuracy with an efficient workflow, semi-automated and automated segmentation strategies were introduced (e.g.[22]). These techniques are until now all based on a single modality, CT imaging. Many are the known limitations of basing the contour outlining on CT scans alone, and this is why most hospitals now contour on multimodality datasets (CT/PET/MRI etc.). But no multimodality automated segmentation algorithms are yet available. We strongly believe this is the path to follow in the future, as complementary information is the key to enhanced reliability. Some attempts are ongoing in (semi)automated segmentation based on the combination PET-CT; but the information provided by US scans can be anatomical and/or functional and molecular, as opposed to PET scans where the anatomical information is limited (if not absent altogether, for non FDG-based PET applications). In fact, US technologies such as contrast imaging, with contrast agents loaded with biological tracers, could potentially provide the highest imaging quality combined with biological information, customized on the target of the tracer. Many more advanced imaging techniques are already available to the US community which could add a valuable contribution both on the anatomical and functional sides, like contrast diffusion [23], harmonic imaging [24], vibro-acoustography [25], elastography [26], tissue typing [27] etc. Evidence is already emerging that US can provide information similar to MRI [28], and that can provide information on patterns of relapse [29].

Ideally, an automated segmentation algorithm should be able to independently make the best use possible of the information provided by all the different modalities available. We believe that the correct approach to achieve this final goal is the use of “intelligent” systems which can learn from experience as it is an extremely effective way to improve accuracy. Especially in a possible future scenario where learning can be distributed and, without the need to share actual data (among other reasons, for privacy), the algorithms can be “sent” to hospitals around the world and trained in situ using a potentially unlimited samples variability; therefore also obtaining the highest accuracy possible, being it dependent on the training sample size [30].

The quantitative conformity indices used in the study allowed: direct comparisons between the results obtained in each single test case from both execution modes; a statistical analysis of results obtained from the whole testing set for each execution

mode; and a comparison between global statistical results obtained from the two execution modes. This was used to demonstrate that our method is useful in those cases where the US images complement CT. In fact, for the patients where a CT scan alone was sufficient to achieve a good conformity, the use of US was not needed or even slightly undesirable. But, while a failing CT scan alone leads to an unacceptable result, the slight decrease in conformity introduced in some patients by the concomitant use of US is always within acceptable thresholds. This indicates that, since in normal applications conformity comparisons cannot be performed (as there are no reference contours), the cross modality approach is always preferable.

The presented example of prostate is straightforward; but we can imagine the same level of advantage for liver, gynecological or kidney tumors, where significant contrast enhancements in US with respect to CT are present. Relatively simple techniques (as the Gabor filters) were used in this work, but with larger datasets more sophisticated approaches can be attempted. Nevertheless, we were able to avoid the need for user intervention, creating a true automated method, where no initial seed or input is required, in contrast to the other methods available (which therefore should all be referred to as semi-automated). This was achieved as another result of the multimodality concept. These results fit in the RT workflow, where a CT scan is always necessary, as source of the density information for dose calculation. Other promising strategies, as for example those based on speckle patterns [31], could be integrated to enhance the outcome quality of the contours.

Our approach is natively 3D, simultaneously using information from all the voxels in the 3D CT and US volumes to create the contours. The algorithm has a more general formulation than strictly necessary for this study to make it seamlessly applicable to more than two modalities.

7.5 Conclusions

An algorithm for automated segmentation of the prostate in cross modality imaging with CT and US co-registered datasets was presented. The algorithm is fully automated, and uses an intelligent approach based on training. When the CT is sufficient for proper segmentation, meaning the distance between the manually contoured reference contour and the automatically generated is below a reasonable threshold, the US images don’t add accuracy to the segmentation process. But in all cases where the CT imaging was not sufficient, the US images complement and systematically reduce the distance.

Acknowledgments

The authors wish to thank Dott.Guido Catolla for his continuous support and inspiration and all staff involved in collecting the 3D US datasets at MAASTRO Clinic, at Azienda Ospedaliera "Maggiore della Carità" and at CRO Oncologic Referral Center.

References

1. Xing L, Thorndyke B, Schreibmann E, et al. Overview of image-guided radiation therapy. Med Dosim 2006;31:91-112.
2. Davis BC, Foskey M, Rosenman J, Goyal L, Chang S Joshi S. Automatic segmentation of intra-treatment CT images for adaptive radiation therapy of the prostate. Med Image Comput Comput Assist Interv 2005;8:442-450.
3. Ghose S, Oliver A, Marti R, et al. A survey of prostate segmentation methodologies in ultrasound, magnetic resonance and computed tomography images. Comput Methods Programs Biomed 2012;108:262-287.
4. Betrouni N, Vermandel M, Pasquier D, Maouche S Rousseau J. Segmentation of abdominal ultrasound images of the prostate using a priori information and an adapted noise filter. Comput Med Imaging Graph 2005;29:43-51.
5. Shen D, Zhan Y Davatzikos C. Segmentation of prostate boundaries from ultrasound images using statistical shape model. IEEE Trans Med Imaging 2003;22:539-551.
6. Jendoubi A, Jianchao Z Chouikha MF. Top-down approach to segmentation of prostate boundaries in ultrasound images. Information Theory, 2004. ISIT 2004. Proceedings. International Symposium on. 2004145-149.
7. Ding M, Chiu B, Gyacskov I, et al. Fast prostate segmentation in 3D TRUS images based on continuity constraint using an autoregressive model. Med Phys 2007;34:4109-4125.
8. Tang X, Jeong Y, Radke RJ Chen GTY. Geometric-model-based segmentation of the prostate and surrounding structures for image-guided radiotherapy 2004:168-176.
9. Costa MJ, Delingette H, Novellas S Ayache N. Automatic segmentation of bladder and prostate using coupled 3D deformable models. Med Image Comput Comput Assist Interv 2007;10:252-260.
10. Siqi C Radke RJ. Level set segmentation with both shape and intensity priors. Computer Vision, 2009 IEEE 12th International Conference on. 2009763-770.
11. Lu C, Chelikani S, Papademetris X, et al. An integrated approach to segmentation and nonrigid registration for application in image-guided pelvic radiotherapy. Med Image Anal 2011;15:772-785.
12. Fontanarosa D, Pesente S, Pascoli F, Ermacora D, Rumeileh IA Verhaegen F. A speed of sound aberration correction algorithm for curvilinear ultrasound transducers in ultrasound-based image-guided radiotherapy. Phys Med Biol 2013;58:1341-1360.
13. Digital Imaging and Communications in Medicine (DICOM), Supplement 11, Radiotherapy Objects, 4 June 1997, ftp://medical.nema.org/medical/dicom/final/sup11_ft.pdf.
14. Matas J, Chum O, Urban M Pajdla T. Robust wide-baseline stereo from maximally stable extremal regions. Image and Vision Computing 2004;22:761-767.
15. S. Koptenko, M. Lachaine, X. Huang and T. Falco, "Methods and systems for segmentation using boundary reparameterization", United States Patent Application Publication, No. US 2008/0008369, 2008.
16. W.M. Chen, "Diagnostic System for 3D Ultrasonography Based on Gabor Filter", Journal of Multimedia, 5, 6, 613-621 (2010).
17. Gabor, D., "Theory of Communication", Journal of Institute of Electrical Engineers, 93, 429-457 (1946).
18. P.C. Mahalonobis, "On the generalized distance in Statistics", Proceedings National Institute of Science, India, 2, 1, 49-55, (1936).
19. C.C. Chang and C.J. Lin., “LIBSVM: a library for support vector machines”, ACM Transactions on Intelligent Systems and Technology, 2, 3, (2011).
20. Jena R, Kirkby NF, Burton KE, Hoole AC, Tan LT Burnet NG. A novel algorithm for the morphometric assessment of radiotherapy treatment planning volumes. Br J Radiol 2010;83:44-51.
21. Vorwerk H Hess CF. Guidelines for delineation of lymphatic clinical target volumes for high conformal radiotherapy: head and neck region. Radiat Oncol 2011;6:97.

22. Pekar V, McNutt TR Kaus MR. Automated model-based organ delineation for radiotherapy planning in prostatic region. Int J Radiat Oncol Biol Phys 2004;60:973-980.
23. Kuenen MP, Mischi M Wijkstra H. Contrast-ultrasound diffusion imaging for localization of prostate cancer. IEEE Trans Med Imaging 2011;30:1493-1502.
24. Choudhry S, Gorman B, Charboneau JW, et al. Comparison of tissue harmonic imaging with conventional US in abdominal disease. Radiographics 2000;20:1127-1135.
25. Alizad A, Whaley DH, Urban MW, et al. Breast vibro-acoustography: initial results show promise. Breast Cancer Res 2012;14:R128.
26. Sayed A, Layne G, Abraham J Mukdadi O. Nonlinear characterization of breast cancer using multi-compression 3D ultrasound elastography in vivo. Ultrasonics 2013.
27. Feleppa EJ. Ultrasonic tissue-type imaging of the prostate: implications for biopsy and treatment guidance. Cancer Biomark 2008;4:201-212.
28. Ito H, Kamoi K, Yokoyama K, Yamada K Nishimura T. Visualization of prostate cancer using dynamic contrast-enhanced MRI: comparison with transrectal power Doppler ultrasound. Br J Radiol 2003;76:617-624.
29. Cellini N, Morganti AG, Mattiucci GC, et al. Analysis of intraprostatic failures in patients treated with hormonal therapy and radiotherapy: implications for conformal therapy planning. Int J Radiat Oncol Biol Phys 2002;53:595-599.
30. Roelofs E, Persoon L, Nijsten S, Wiessler W, Dekker A Lambin P. Benefits of a clinical data warehouse with data mining tools to collect data for a radiotherapy trial. Radiother Oncol 2013.
31. Davignon F, Deprez JF Basset O. A parametric imaging approach for the segmentation of ultrasound data. Ultrasonics 2005;43:789-801.

Appendices

Appendix A

Appendix A1. Generation of a base of unit vectors

The generation of the unit vectors of the base used in the procedure is given by a recursive normalized polyhedral subdivision process (following the procedure described in [14]) which starts from six versors arranged along the fundamental axes {i, -i, j, -j, k, -k} and connected to form a triangular mesh. Any further subdivision adds a number of new unit vectors equal to the number of connections between vertices in the current distribution and a number of connections equal to 3 times the number of triangles in the current mesh. Therefore, the vector systems obtained at the 1st, 2nd, 3rd, 4th . . . subdivision will have 18, 66, 258, 1026, . . . vertices respectively (Figure A1). In the proposed implementation we have chosen the 3rd subdivision with 258 vertices.

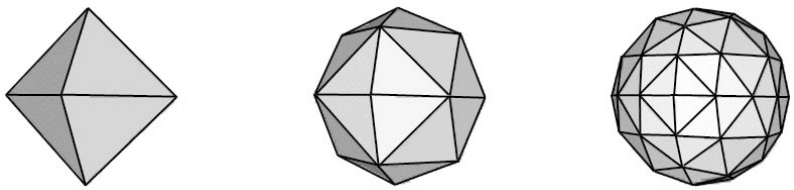

Figure A1: Two iterations of the subdivision procedure applied to a normalized octahedron for the generation of the unit vectors.

Appendix A2. Neighboorhood LUTs Definition

Given a PDCV with a base formed by the unit vectors $\mathbf{v}_i$ (x,y,z) and a positive integer k, for each i, we can define:

$$N_i = \{\mathbf{n}_{ij} = \mathbf{v}_j, 0 \leq j < k\} \tag{7.A.1}$$

as the set of k-nearest (using Euclidean distance) neighbors of $\mathbf{v}_i$ within the base.
Following this definition, we can define M_i^v as the set of surface points whose associated unit vectors belong to N_i

$$M_i^v = \{\mathbf{m}_{ij}^v := \mathbf{o} + c_j \mathbf{n}_{ij}, 0 \leq j < k\} \tag{7.A.2}$$

M_i^v consists of the k-nearest neighbors of the surface point $\mathbf{p}_i^v$ within the set of all surface points, using the angular distance relative to the center of the reference system associated with the PDCV.

This formulation is convenient for many reasons:

The number of neighbors for each unit vector $\mathbf{v}_i$ or point $\mathbf{p}_i^v$ is not fixed or constrained by structural aspects in the definition of PDCV, but can be chosen depending on custom needs.

N_i and M_i^v sets need not to be explicitly generated. It is possible to use for each i a Look-Up Table (LUT), named $NLUT_i$, of the positions j of unit vectors $\mathbf{v}_j$ within the base that belongs to N_i; or, equivalently, such that $\mathbf{p}_j^v$ belongs to M_i^v.

Given a PDCV, you can define more than one neighborhood scheme associated with it: more than one NLUT instance can be created at the same time and associated with the same PDCV but with different values for k.

Appendix A3. Computation of the Normal directions.

Pre-computing a mapping $NLut_{normal}$ with $k = k_{normal}$ for each surface point $\mathbf{p}_i^v$, an association to the set $M_i^v{}_{normal}$ of its k_{normal} surface neighbors is induced according to the previously described procedure. The unit vector $\mathbf{l}_i^v$ normal to the surface (Figure A2) is then calculated as the normalized eigenvector associated with the smallest eigenvalue of the covariance matrix of x, y, z coordinates of the points that belong to the collection $M_i^v{}_{normal}$: in fact, the orthogonal basis of eigenvectors of this matrix is arranged such that the directions associated with two largest eigenvalues are those of maximum spatial variance. If the angular sampling of PDCV is sufficiently fine, these directions are arranged along the tangent plane to the surface at the point $\mathbf{p}_i^v$; then, for the orthogonality of the base, the remaining eigenvector is positioned along the normal.

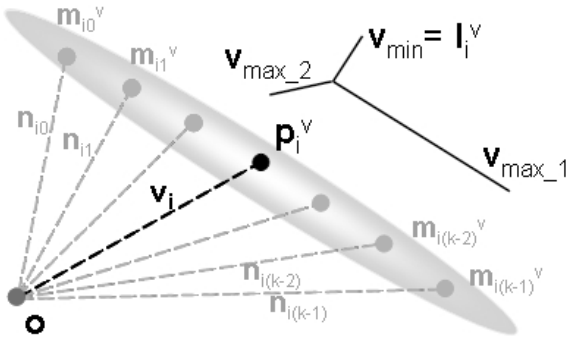

Figure A2: Example of a set of neighbors ($M_i^v{}_{normal}$) of p_i^v. The unit vector l_i^v is calculated as the normalized eigenvector associated with the smallest eigenvalue of the covariance matrix of the points that belong to the collection $M_i^v{}_{normal}$.

Appendix B

Classes Definition

Another important concept related to the structure of the PDCV are the classes or membership areas for surface points: the segmentation might give more accurate results if the target is characterized differently according to the different sub-regions of the surface considered. The size and position of these areas are intrinsic features of the object to be segmented and are not related to the angular sampling used for the PDCV base of unit vectors which is, on the contrary, associated to the accuracy of the surface description.

To this end, alongside the fundamental base of unit vectors, it is possible to associate to a PDCV one or more additional bases obtained with the same procedure used for the set of $\mathbf{v}_i$ (polyhedral subdivision), but with a lower number of reiterations.

The unit vectors $\mathbf{v}_j^l$ of this base are a subset of unit vectors $\mathbf{v}_i$ and will induce a latter partition of the fundamental base into classes:

$$C_j = \{v_i \ \textit{such that} \ \left\|\mathbf{v}_i - \mathbf{v}_j^l\right\| \le \left\|\mathbf{v}_i - \mathbf{v}_k^l\right\| \\ \textit{for every other} \ \mathbf{v}_k^l \ \textit{within the classes base}\} \qquad (7.B.\ 1)$$

A mapping CLUT of the unit vectors of the fundamental base in these classes can be pre calculated as in the case of NLUTs, with the further simplification that only one map of indexes on the whole PDCV is sufficient this time.

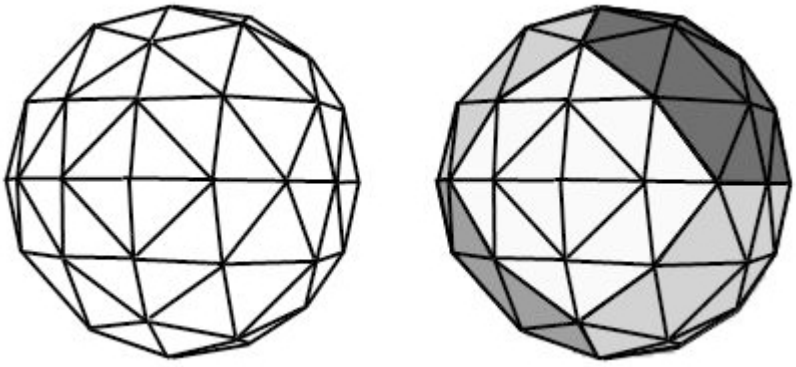

Figure B1: Partition of the fundamental base into classes, representing different sub-regions of the surface.

Appendix C

Geometrical Mapping from 3D to 2D

We have adapted the original idea described in [1], where it was formulated in 2D to a more general 3D case; the segmented area contour could be described by any data structure (i.e. spline, levelset, . . .) that represent a two-dimensional closed curve:

$$\mathbf{Curv}(u') \tag{7.C. 1}$$

with u' the curvilinear coordinate.

For any curvilinear coordinate u', it is possible to determine the direction **n**(u') normal to the **Curv** in u'; moreover for every real value v' it is possible to locate the point on the normal **n**(u') whose distance from **Curv**(u') is v' (Figure C1(a)).

Thus:

dividing **Curv**(u') in U intervals of constant curvilinear length $\Delta u'$, we can take an integer u in {0, 1,. . . . , (U-1)} such that the points u' = u $\Delta u'$ define a sampling of the whole curve,

assigning a fixed range [-V_0 * $\Delta v'$, V_1 * $\Delta v'$] for v' in which $\Delta v'$ is a constant interval, we can choose v in {0,. . . . ,V_0,. . . . ,(V_0+V_1)} such that the values v' = (v - V_0) $\Delta v'$ define a sampling along the normal direction, where V_0 is the number of samples taken internally to the curve, while V_1 is the number of samples taken externally.

It is now possible to project the values of a stripe extracted around the curve from the slice, in a projection image (PI) of size [U; (V_1-V_0)] (Figure C1(b)) using the function:

$$PI(u,v) := Interp2(Slice, \mathbf{Curv}(u'(u)) + \mathbf{n}(u'(u)) * v'(v)) \tag{7.C. 2}$$

with

$$Interp2(Image, Point) \tag{7.C. 3}$$

being a function that performs a bilinear interpolation of the values from the reference image (Image) in the given point (Point).

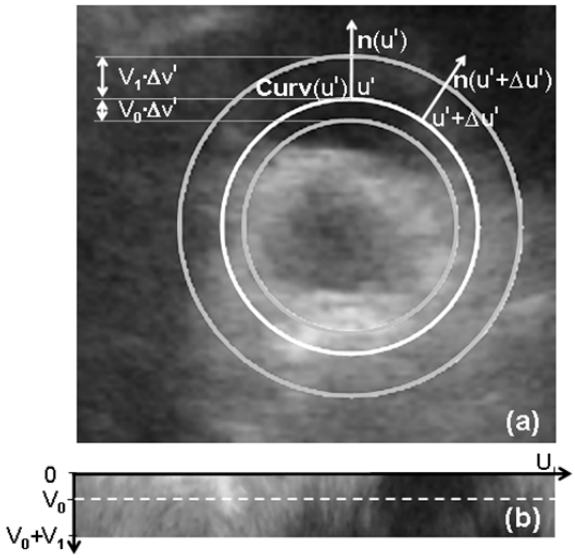

Figure C1: (a) Two-dimensional closed curve **Curv**(u') with u' curvilinear coordinate describing the segmented area contour; **(b)** Projection of the values of a stripe extracted around the curve from the US slice, in an image of size [U; (V_1-V_0)].

In order to adapt this transformation to the 3D case, we can simply use the characteristics of the support structures described in the previous section.

In particular, the extraction of a stripe around the border of the current PDCV is performed taking the values from the reference volume $Volume_m$ using a trilinear interpolation function:

$$Interp3(Volume, Point) \tag{7.C. 4}$$

in the point:

$$\mathbf{p}_u^v + \mathbf{I}_u * v \tag{7.C. 5}$$

with $\mathbf{p}_u^v$ surface point and l_u normal to the surface in $\mathbf{p}_u^v$ and inserting them in the relative points inside the projection image through:

$$PI(u,v) := Interp3(Volume, \mathbf{p}_u^v + \mathbf{l}_u * v'(v)) \tag{7.C. 6}$$

Some points need to be clarified about this type of extension:

- Since the u-coordinate indexes the unit vector base of the PDCV, it identifies points distributed on the surface of the structure with a constant solid angle, implicitly sampling based on the structure itself, and not, as in the two-dimensional case, by an arbitrary amount Δu'. Similarly, the cardinality of the base will implicit-

ly determine the U value concerning the extension [0, U] on which this coordinate could range.

- On the series of samples extracted for u in {0, 1, … , U-1} no inherently spatial ordering is defined as it happens in the 2D case; therefore no concept of neighborhood is given by default; however this gap can be easily overcome through the use of a specific NLUT (see section 7.2.2.2.).
- The v-coordinate has the same characterization as in the 2D case, except that the normal two-dimensional unit vector **n**(u') is replaced by the normal 3D unit vector $\mathbf{l}_u$ computed using the procedure described in the previous section.

The PI so generated represents the source volume region that the current PDCV 'sees' and will provide the background for the extraction of features in the current iterative step. Its parameters have therefore the following meaning:

- $\Delta v'$ normal resolution.
- $V_0 * \Delta v'$ inner extension of the stripe. It represents the spatial sensitivity of a single iterative step inside the PDCV region.
- $V_1 * \Delta v'$ external extension of the stripe. It represents the spatial sensitivity of a single iterative step outside the PDCV region.

This procedure is applied to all NM modalities generating the sequence of projection images:

$$PI^{NM} = \{PI_m,\ 0 \le m < NM\} \tag{7.C. 7}$$

As in the original formulation, the PI_m are treated with a normalization procedure that involves two distinct components:

- Global Normalization $N^{gl}(PI_m)$: PI_m is normalized as a whole. This component introduces a certain degree of invariance with respect to the contrast and to the overall average level of the area under analysis and it aims not only at properly managing the intra modal comparison between volumes scanned with the same sensor type; but also at re-balancing the significance of the information coming from different modalities.
- Local Normalization $N^{loc}(PI_m)$: PI_m columns are individually normalized. This component introduces a certain degree of invariance with respect to the strength of this signal in different surface areas of the analyzed region.

The transformation applied on PI_m can be expressed as:

$$PI_m = \Omega * N^{gl}(PI_m) + (1-\Omega) * N^{loc}(PI_m) \tag{7.C. 8}$$

Where:

$N^{gl}(PI_m)$ is the result of the global normalization,

$N^{loc}(PI_m)$ is the result of the local normalization and

Ω is the weight of the global with respect to the local normalization.

An example of results of global normalization applied to the PIs associated to an US and a CT Volumes are shown in Figure C2.

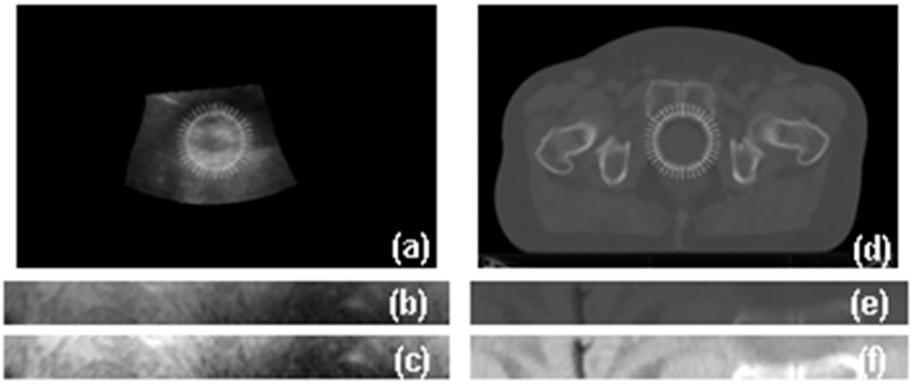

Figure C2: (a), **(d)** US and CT Volumes; **(b)**, **(e)** Projection Images (PI) and **(c)**, **(f)** results of global normalization applied to PI associated to US and CT Volumes.

Appendix D

Appendix D1. Transformation from Data to Features Space

We have chosen, (similarly to what has been done in [2,3]) the Gabor features [4], specifically customized.

The basic element of a Gabor filter applied to one point is the answer, expressed as a complex number, of the convolution of the data around the same point with a pair of sinusoidal functions in quadrature modulated by a Gaussian. From a signal analysis point of view, they correspond, respectively, to an edge and a blob detector.

The one-dimensional version can be expressed as:

$$Gabor(\mathbf{x};\sigma,\lambda)=e^{i2\pi\frac{x}{\lambda}}e^{-\frac{x^2}{2\sigma^2}} \tag{7.D. 1}$$

or, equivalently, with the couple:

$$Gabor_{\mathrm{Re}}(\mathbf{x};\sigma,\lambda)=\cos\left(2\pi\frac{x}{\lambda}\right)e^{-\frac{x^2}{2\sigma^2}} \tag{7.D. 2}$$

$$Gabor_{\mathrm{Im}}(\mathbf{x};\sigma,\lambda)=\sin\left(2\pi\frac{x}{\lambda}\right)e^{-\frac{x^2}{2\sigma^2}} \tag{7.D. 3}$$

In practice, the wavelength λ of both sinusoids is made dependent on the standard deviation σ of the Gaussian, in such a way that the modulation reduces significantly the signal at $x = \pm\lambda$; the resulting function is then only dependent from the parameter σ that represents the specific spatial scale to which the Gabor filter is sensitive.

The ability to select different values for this parameter allows the derivation of the more complex Gabor filters bank [5] with variable σ, that can be expressed as the multiple convolution operator:

$$\begin{aligned} G^S(f) := (&Gabor_{\mathrm{Re}}(.;\sigma_0)*f(.), Gabor_{\mathrm{Im}}(.;\sigma_0)*f(.),\ldots,\\ &Gabor_{\mathrm{Re}}(.;\sigma_{NS-1})*f(.), Gabor_{\mathrm{Im}}(.;\sigma_{NS-1})*f(.)) \end{aligned} \tag{7.D. 4}$$

with σ in ($\sigma_{0,\ldots,}\sigma_{NS-1}$) and NS number of scales used.

The detector obtained this way has a multi-scale expressiveness.

In the common formulation of multidimensional Gabor filters banks another parameterization can be done by changing the orientation of the sinusoidal components. Anyway, in the proposed solution, the Gabor filter bank used is one-dimensional and acts along the vertical direction of PI_m; or, which is the same, along the normal direction to the surface of the actual PDCV.

Therefore, for each modality, its application to the PI_m produces the function:

$$G_m^S = [0, u-1] \times [-V_0, V_1] \rightarrow \Re^{NT^S}$$

$$G_m^S(\mathbf{u}) := G^S(PI_m(\mathbf{u})) \qquad \text{(7.D. 5)}$$

that associates to each point in the domain of active background **u** = (u,v) a feature vector of size $NT^S = 2 * NS$.

To further characterize every point of the active background with features that represent not only structures present on its location, but also in locations close to it along the normal to the PDCV, we have introduced the concept of topological multiplicity.

From each point $\mathbf{u}_0 = (u_0, v_0)$ in the domain of PI_m the following series of points can be derived (Figure):

$$\mathbf{u}_i = \mathbf{u}_0 + i\,\Delta\mathbf{t} \qquad \text{(7.D. 6)}$$

where

$\Delta\mathbf{t} = (0, \Delta t_v)$ is the vertical spacing,

$i \in \{-T_0, \ldots, 0, \ldots, T_0\}$ is the index of topological multiplicity and

$NT = 2 * To + 1$ is its cardinality.

Figure D1: Series of points derived from a point $\mathbf{u}_0 = (u_0, v_0)$ of a PI_m.

The features extracted from each of the derived series points are concatenated into a single vector by defining, for each modality, the function:

$$G_m^t = [0, U-1] \times [-V_0, V_1] \rightarrow \Re^{NT^t}$$

$$G_m^t(\mathbf{u}) := (G^S(PI_m(\mathbf{u_0}), \ldots, G^S(PI_m(\mathbf{u_{NT\text{-}1}})) \qquad \text{(7.D. 7)}$$

that relates to each point **u**=(u,v) in the domain of the active background a feature vector of size:

$NT^t = NT^S * NT = 2 * NS * NT$.

To make the final descriptor actually multimodal, the NM feature vectors, resulting from each G^t_m, must be concatenated defining the unique function:

$$G^f : [0, U-1] \times [-V_0, V_1] \rightarrow \Re^{NF}$$

$$G^f(u) := (G_0^t(\mathbf{u}), ..., G_{NM-1}^t(\mathbf{u})) \qquad \text{(7.D. 8)}$$

that associates to each point **u**=(u,v) in the domain of the active background a feature vector of size:

NF = NM * NT^t = 2 * NS * NT * NM.

Appendix D2. Model and Training

The model characterizing the points on the surface of the target makes use of the Mahalonobis Distance [19], in the features space computed on the training set to estimate the conformity to the target border.

The following quantities are computed from the set { $\mathbf{fv}_i$ } obtained in the training phase:

- the average feature vector $\mathbf{fv}^{avg}$,
- the set of deviations from the mean vector {d$\mathbf{fv}_i$} = { $\mathbf{fv}_i$ - $\mathbf{fv}^{avg}$ },
- the covariance matrix $\mathbf{m}^{cov}$ on the latter set,
- the pseudo-inverse matrix $\mathbf{m}^{inv}$ of $\mathbf{m}^{cov}$.

From the matrix $\mathbf{m}^{inv}$ a metric can be derived on the space of features with a distance given by:

$$Dist^{model} : [0 \times NF] \rightarrow \Re$$

$$Dist^{model}(fv) = \| fv \|^2 = (fv - \mathbf{fv}^{avg}) \mathbf{m}^{inv} (fv - \mathbf{fv}^{avg})^T \qquad \text{(7.D. 9)}$$

which measures the deviation of the fv feature vector from the statistical average $\mathbf{fv}^{avg}$ taking into account variances and co variances of vector components in the training set.

Thus the model is formed by the couple:

$$Model = \{\mathbf{fv}^{avg}, \mathbf{m}^{inv}\} \qquad \text{(7.D. 10)}$$

needed to implement the prediction function $Dist^{model}$.

It must be noted that the simple linear training/prediction method used in this work can be easily replaced if a larger and more complex training dataset is available. A suggested choice is the use of the well-known Support Vector Machine (SVM) paradigm: a suitable implementation is described in [20]. This paradigm is able to handle non-linear complex functions in the feature space describing the true positives clusters in the training set more accurately.

Appendix D3. Feature Volume Space.

From a developmental point of view, the features retrieved the modality stripes can be represented as a volume (see Figure) describing the features space:

$$VF : [0, U-1] \times [-V_0, V_1] \times [0, NF-1] \rightarrow \Re$$

$$VF(u, v, f) := (G^f(u, v))_f \qquad \text{(7.D. 11)}$$

with $(G^f(u, v))_f$ f-th component of $G^f(u, v)$ and f feature index in the range [0,NF-1].

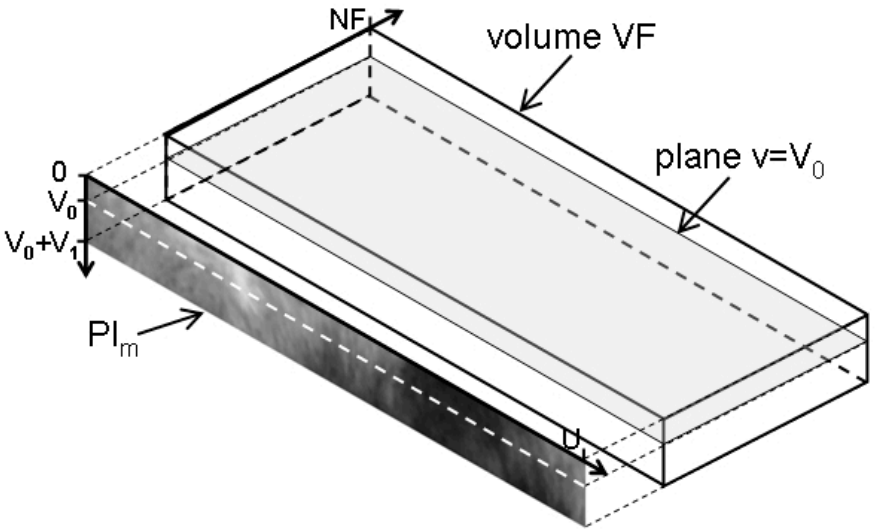

Figure D2: Volume describing the features space (VF). Sections along u and v axes correspond to the projected Images PI_m. Sections along u and t axes, for $v = V_0$, represent the features extracted from points on the PDCV border.

This representation is computationally very convenient to avoid the overhead that the topological multiplicity concept introduced during the extraction phase: in fact once computed and stored inside the volume VF the features directly extracted from each point $\mathbf{u}_0 = (u_0, v_0)$, no further Gabor filtering is required for the points of the series in (7.D.6), but only a data copy from appropriate locations.

During the training phase clearly only the features on the $Reference_p$ PDCV border are needed so that only the plane $v = V_0$ in VF is filled; the feature vectors corresponding to every different coordinate u = [0, U-1] are inserted into the set $\{fv_i\}$ used for training.

During the prediction phase, estimating each point conformity with the target border can be than simply implemented by means the function $Dist^{model}(fv)$ previously

trained, that can be viewed as a reverse function that fills the conformity mask PI^{mask} with the same dimensions of the PIs from the Feature Volume data (Figure D3):

$$PI^{mask}(u,v) := Dist^{model}(fv(u,v)). \quad (7.D.\ 12)$$

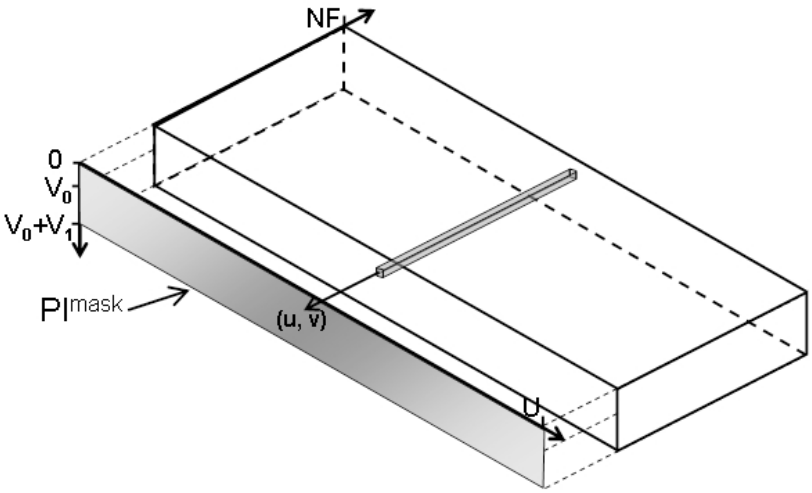

Figure D3: PI^{mask} built from the features volume VF and from the prediction function $Dist^{model}$.

Appendix E

Classes Model Specialization

Once a fixed partition of PDCV elements in a set of classes {C_j , with $0 \le j < nC$}, with nC number of classes, has been pre-computed using the mapping CLUT, the following changes should be applied:

- The single features model (7.D.10) is replaced by nC separate models

$$Model_j = \{\mathbf{fv}_j^{avg}, \mathbf{m}_j^{inv}\}, \quad 0 \le j < nC \tag{7.E. 1}$$

characterizing different areas on the target surface.

- During the training phase, feature vectors extracted from the u coordinate in the $v=V_0$ plane of the VF feature volume (7.D.11) are inserted in the set of training feature vectors associated with the model $Model_{CLUT\,(u)}$, so they contribute only to the model associated with the class the surface point $\mathbf{p}_u$ belongs to.
- Similarly during the prediction phase feature vectors extracted from the point determined by coordinates (u,v) in the feature volume VF will be evaluated by the model $Model_{CLUT\,(u)}$ referring to the class the surface point $\mathbf{p}_u$ belongs to.

The mask of conformity is then filled with:

$$PI^{mask}(u,v) = Dist^{model}_{CLUT\,(u)}(fv) \tag{7.E. 2}$$

where :

$$Dist^{model}_{CLUT\,(u)} \tag{7.E. 3}$$

is the predictive function associated with $Model_{CLUT\ (u)}$, while CLUT(u) identifies the class of the point $\mathbf{p}_u$ according to its index u.

With these tools at hand, the formulation of the iterative update component of coefficients c_i dependent on the features remains formally unchanged; but it is now able to adjust to and differentiate for different surface areas, inter alia, removing the problem of clustering management caused by the different characterizations of the border of the target.

Appendix F

Smoothness

A neighborhood mapping different than the one used for the calculation of the normals is defined on the PDCV as follows:

$NLut_{smooth}$ with $k = k_{smooth}$ and $k_{smooth} \neq k_{normal}$,

inducing for every unit vector $\mathbf{v}_i$ the set $N_{i\ smooth}$ of its neighbours within the base of the PDCV and, for each $\mathbf{p}_i^v$, a set of its surface neighbours in the solid angle.

This mapping, as in the case of the neighborhood used for the calculation of the normal, is pre calculated and do not require any update during the iterative process (see Appendix A2).

Thus, the smoothing component provides, for each c_i^{feat} coefficient, the estimation of:

$$\underline{c}_i^{smooth} = \frac{\sum_{v_j \in N_i^v} c_j^{feat} * W(i,j)}{\sum_{v_j \in N_i^v} W(i,j)} \qquad (7.F.1)$$

weighted and normalized average of c_j^{feat} coefficients of the unit vectors $\mathbf{v}_j$ in the neighborhood of $\mathbf{v}_i$, with *W(i,j)* a weighting function dependent on the distance between $\mathbf{v}_i$ and $\mathbf{v}_j$.

The PDCV coefficients in this component were updated according to (7.11).

It should be noted that the β parameter (defined in Section 7.2.3.2.) allows to obtain a compromise between a result with an overall shape completely free of constraints, but with high local irregularities; and a result with a pseudo spherical global shape that is locally highly regular: the more β approaches 1 the closer to a sphere the overall shape will be, since the coefficients c_i^{smooth} will be driven to the same values as their neighbours, especially when other iterative components have reached a state of equilibrium (see Figure F1).

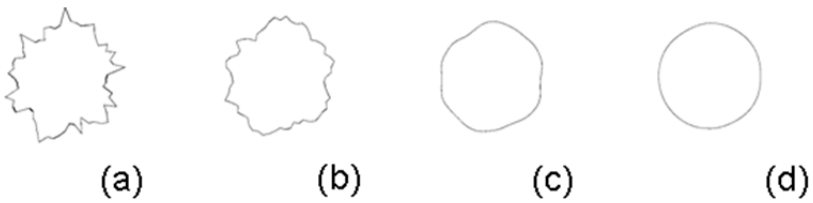

Figure F1: Example of smoothing update procedure with β = 1, at iteration (a) 0, (b) 1, (c) 5, (d) 20.

Appendix G.

Shape

The shape model can be calculated using only the { $Reference_p$ } set, and for this reason is very flexible and general.

An approximate shape representation associated with a specific instance of PDCV can be defined as the histogram Sh with a number of bins equal to the number of unit vectors in its base, whose entries are given by:

$$Sh[i] = \frac{c_i}{\frac{\sum_{j \in NLUT_{smooth\ i}} c_j}{k_{smooth}}} \tag{7.G.1}$$

where the i^{th} bin is the ratio between the c_i coefficient associated with vector $\mathbf{p}_i$ and the average of coefficients c_i associated with the vectors $\mathbf{p}_j$ that are neighbors of $\mathbf{p}_i$ via the same $NLUT_{smooth}$ mapping used for smoothing.

As these coefficients represent the length of their associated surface vector within the PDCV system of reference, the Sh[i] value is an index of local convexity of the surface in the surface point $\mathbf{p}_i$.

Figure G1 shows three cases where Sh[i] is higher, lower or equal to 1, respectively.

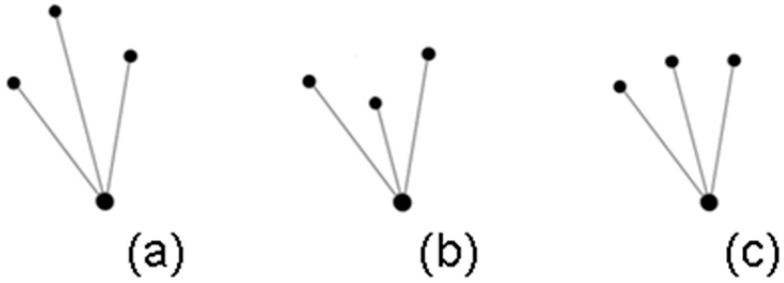

Figure G1: Three cases where Sh[i] value, which is an index of local convexity of the surface in the surface point, is (a) higher, (b) lower or (c) equal to 1.

A reference shape model from the training set can be generated by computing the histogram Sh^{avg}, whose entries are given by the average of the corresponding entries in the shape patterns Sh_p extracted from each $Reference_p$ of the training set:

$$Sh^{avg}[i] = \frac{\sum_{p=0}^{NP} Sh_p[i]}{NP} \tag{7.G.2}$$

The shape iterative component acts once more only on the PDCV scalar coefficients c_i^{smooth} resulting from the previous components; starting from them, the shape pattern Sh is computed. The estimate $\underline{c}_i^{shape}$ for each coefficient is then evaluated as:

$$\underline{c}_i^{shape} = c_i^{smooth} * \frac{Sh^{avg}[i]}{Sh[i]} \qquad (7.G.3)$$

which is the value that should have the i^{th} coefficient to match the same degree of local convexity as the corresponding item in the model calculated from the training set. Then, the PDCV coefficients in this component were updated according to (7.10).
As for the equation of the smoothing component, a higher value of γ (defined in Section 7.2.3.2) produces a higher tendency for the PDCV to adapt its shape to the model (Figure G2).

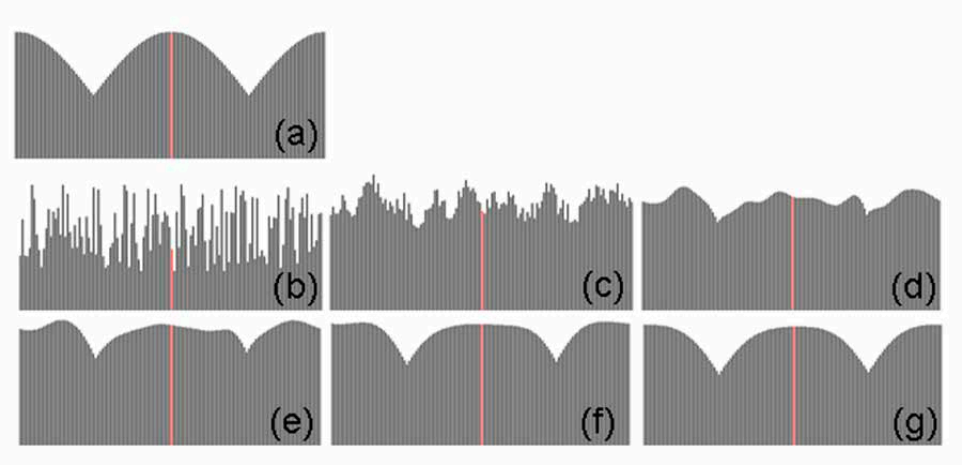

Figure G2: (a) Reference shape model; (b)-(g) Sh histograms at iterations n. 0, 1, 5, 10, 20, 100, starting from a random shape without the influence of all the other iterative factors and $\gamma = 1$.

References

1. S. Koptenko, M. Lachaine, X. Huang and T. Falco, "Methods and systems for segmentation using boundary reparameterization", United States Patent Application Publication, No. US 2008/0008369, 2008.
2. Shen D, Zhan Y Davatzikos C. Segmentation of prostate boundaries from ultrasound images using statistical shape model. IEEE Trans Med Imaging 2003;22:539-551.
3. W.M. Chen, "Diagnostic System for 3D Ultrasonography Based on Gabor Filter", Journal of Multimedia, 5, 6, 613-621 (2010).
4. Gabor, D., "Theory of Communication", Journal of Institute of Electrical Engineers, 93, 429-457 (1946).
5. A. Olowoyeye , M. Tuceryan and S. Fang, "Medical Volume Segmentation using Bank of Gabor Filters", Proceeding of the 2009 ACM symposium on Applied Computing, 826-829 (2009).

Discussion

Chapter 8

General discussion and future perspectives

Speed of sound (SOS) aberration in ultrasound (US) imaging is a problem which an important fraction of the US community has to face. In particular, whenever quantitative spatial applications of US are involved, if the scanned structure is sufficiently deep, likely its position and/or shape will be significantly affected by this aberration. What does "sufficiently deep" mean? Unfortunately, it is not possible to predict after which depth the aberration becomes important. In fact, thick surface fat layers can produce SOS displacements after just a few cm. After 5 cm, the aberration due to SOS in fat is already 3 mm. A 3 mm misplacement of a target structure is sufficient to trigger some action in most of clinical radiotherapy (RT) treatments. In other applications, outside RT, even shorter distances can be significant. An interesting example is a very recent project for cardiac arrhythmia treatment. The project, named CyberHeart (http://www.cyberheartinc.com/), aims at non-invasive radiosurgical ablation using the CyberKnife Robotic Radiosurgery Sytem (Accuray Inc., Sunnyvale, CA, USA) to effect electrical conduction block at the left pulmonary vein [1]. To localize precisely the ablation spot on the rear wall of the heart, the researchers use US imaging. At 15 cm depth, through the chest and the heart, a SOS aberration up to 1 cm can be produced. The accuracy they would need to create a scar on the wall should be one order of magnitude smaller.

The problem is reported extensively in the literature (e.g. [2]), but not many solutions were proposed. Probably, until quantitative applications became explored, this issue was not perceived as excessively limiting. The solutions available generally looked for an (automated) method to better approximate the assumed SOS value in a specific body region (e.g. [3]). Other corrections relied on complex multiple beams arrangements which are clinically impractical [4]. But no voxel-by-voxel solution taking into account all the SOS variations in the scanned volume was ever attempted. The major reason is that from the US scan alone it is difficult (if even possible) to understand which tissue types are being scanned. And even if the structures or organ disposition can be inferred (e.g. from anatomy knowledge) this information can hardly be used for a correction. The same organs can have quite wide ranges of possible SOS values, depending on the tissue composition. As an example, let's consider the SOS value associated with breast tissue. According to [5], if the scanned person was premenopausal, the range of values would be (1450-1570) m/s, with an average of 1510 m/s. If she was postmenopausal, instead, the range would be lower, (1430-1520) m/s, with an average of 1468 m/s. If she was lactating, the value would be 1550 m/s. If cancer is present, the values change again: carcinoma produces a mean SOS value of 1465 m/s, fibroadenosis 1529 m/s, fibrocystic disease 1514 m/s, etc. Other authors saw completely different values. Frucht et al. e.g. report for breast with carcinoma a SOS value of 1573 m/s [6]. Moreover, the balance between fat content and glandular tissue can move the SOS value from 1470 m/s (high fat content) to 1550 m/s (mostly

glandular tissue). If the pectoral muscle is (partially) included, the value changes to 1545 m/s [5]. Of course the temperature of the analyzed sample is also important, the age of the patient, the type of measurement (time of flight, acoustic interferometry, pulse transmission/overlap, etc.) and the preparation (in vivo, on excised fresh/refrigerated/formalin fixed etc.). The complete range of reported values due to these variables is from 1413 m/s to 1573 m/s. And this holds true for most of the organs (for a comprehensive list of values, see [7]).

It should be clear at this point that in some cases (like RT for liver cancer, as shown in Chapter 4) a correction for SOS should be adopted. And that some more fundamental properties of the materials traversed by the US wave than the organ type must be used for a reliable correction.

SOS depends essentially on three properties of the material traversed: physical density, compressibility and resistance to shear stress. The second factor, represented by the bulk modulus K, is dominant. In fact, if we imagine that we can vary the density without affecting compressibility, the SOS should be inversely proportional to density (to its square root, more precisely). What happens instead, at least for human tissues, is that there is a direct proportionality, roughly linear. This is the observation which guided the whole work reported here. The density information is retrieved from the co-registered simulation CT scan and used to correct the US scans taken prior to the treatments. Shear stress, represented by the Young modulus G, has generally a very limited impact on SOS and is therefore neglected. But G is what is typically mapped by elastographic US systems. The most recent ones use a technology based on shear waves [8]. When the shear wavefronts traverse areas with different shear propagation speeds (Shear Wave Speed, SWS) they are distorted. In particular, when the tissues have a higher SWS value, the wave will propagate faster. And vice versa. The calculation of front displacements with time allows for mapping of SWS. It actually allows the estimation of group and phase velocities, as a function of frequency. Then from SWS it is possible to calculate G and, from this, stiffness of the tissue. Noteworthy, shear waves are not compressional waves and SWS is not SOS. Compressional waves travel much faster than shear waves, about 1000 times faster. This is actually the reason why we can image them using US devices. Another interesting property of G is that its value can vary by more than a factor 105 for human soft tissues. K instead varies around 12% [8]. This means that G is more sensitive to variations in mechanical properties of tissues than K. It is unlikely that the mechanical changes producing a contrast in K will leave G unaffected. Our group is working on determining this relationship which would allow a tissue mapping in K. From this distribution it would be possible to perform a direct calculation of SOS, using e.g. the empirical relationship between compressibility and density variations published by [9]. As opposed to simulation CT density-based method, this method would not require any other imaging modality dataset. This opens an entirely new scenario: applications where co-registered CT scans are not available, would become possible. Examples are: (1) radiology, where US have a

widespread adoption; (2) the previously cited CyberHeart project; and (3) gynecological brachytherapy applications for sites like cervix, where transabdominal US scans are performed in the vast majority of cases without any co-registered CT scan available. Moreover, the correction would be based on information retrieved immediately prior to the scan, which would eliminate the (second order) discrepancies due to changes over time occurring between simulation and treatment stages (described in Chapter 5). Despite the potential advantages, in RT elastography is not yet an established technology, though, whereas co-registered CT scans from the simulation stage are frequently available. This is why we worked on this option first. But the implementation of elastography would not involve any changes in the treatment workflow, just a different probe, in principle. Besides its use for SOS aberration correction, elastography would allow a more extensive use of US in RT. Not only would US allow patient positioning, but also e.g. treatment response monitoring, as tissue elasticity has been found to have a relationship with tumor nature of the tissue [10,11]. It must be noted, though, that more complex US imaging may partially offset its low current cost.

Why should a correction based on a relationship derived from SOS measurements on organs be trusted? As mentioned before, SOS variability is very high. It is clear, especially considering the results reported in Chapter 5, that relatively minor variations with respect to the assumed value of 1540 m/s are not important for a reliable correction. What in the end is really important, according to our experience, is the amount of fat and muscle along the line of view. Therefore, it is important have a method to quantify this. Fortunately, the average physical densities of fat and muscle are very different, and so are their SOS values. Recognizing the organs along the lines of view is not as important as establishing how much is the relative content of fat and muscle, which is rather easy to understand based on density. And it's their SOS which, being significantly different from 1540 m/s, makes the difference in the final correction. An example for fat are the liver cases reported in Chapter 4. Another example is muscle in the CyberHeart project. Interestingly, not all of the fat/muscle content must be precisely identified. A estimated 75% or 80% in our experience is sufficient to produce a reliable correction. The reason is that, for clinical applications on human tissues, only errors larger than about 2 mm can be appreciated. This is because to assess the discrepancy a CT scan is compared to the US scan and the two modalities cannot strictly speaking be directly compared as they image different properties of tissues; e.g. prostate or seroma size estimates are consistently different between the two modalities. Therefore, also a correction based on elastographic information would probably benefit enough already from a segmentation of muscle and fat along the line of view.

The clinical part of the work addresses an issue reported extensively in the literature: US imaging in some situations seems to show wrong positions for internal structures compared to other imaging modalities [12-14]. Some researchers trying to face this problem have hypothesized that probe pressure [15], difference in contour visualization [16], initial isocenter definition [16] or SOS [2] could be the reason for that. But

there was no clear understanding of what the respective impact was or, above all, which conditions exactly produced important errors. We do not believe that we have answered completely these questions. But we have shown that all the reported discrepancies in literature (especially for prostate, the most frequent application) can be largely explained with SOS aberration. Recent scanning protocols in RT, especially for prostate and breast cancer, require as little pressure and as little tissue displacement as possible. So we are confident that probe pressure is not a valid reason to explain the reported discrepancies in our work. We have identified and described the factors which influence the importance of the error: the presence of tissues with SOS values higher or lower than the value assumed by US systems (typically 1540 m/s) along the US beam line of view. This explains also why it was so difficult to understand in the past the clinical impact of this aberration: the error is cumulative but not monotonic. This means that while it is necessary that objects at large depths are imaged to see the aberration, it is not sufficient. In some situations compensation occurs and no error is evident even at 18 cm. The liver cases shown in Chapter 4 are a clear example. This also proves how difficult it is to consider a general systematic correction. For tissues that are homogeneous in SOS values, though, the aberration accumulates monotonically. Assumptions about the average SOS behavior can then be made and the assumed SOS value can be fine-tuned. This is the approach followed by some manufacturers which allow e.g. a lower SOS value for breast applications. Considering the range of possible values for breasts mentioned previously, this is a clear indication that for the reference patient fat content for breast is dominant, although we know from literature that this is a weak assumption [17]. If the tissues are heterogeneous, instead, the aberration does not accumulate monotonically. So even if an average optimal value is calculated, the error produced will not propagate linearly. Its magnitude and sign will depend on the point along the line of view where it is measured in an unpredictable way. More body regions should be accurately studied, from this perspective. For example, gynecological patients might show a higher SOS homogeneity than prostate cancer patients. Anatomically, the fat content along the lines of view of transabdominal US scans of cervix or uterus is typically dominant, resulting in a situation similar to breasts, but possibly with larger depths.

Another consequence of these observations is that structures at shallow depths will not be significantly affected by this aberration. The breast cases reported in Chapter 5 are an example. Fortunately for a broad range of US applications the distance between the transducer and the target is short. This is the case e.g. for all intracavitary probes (as for brachytherapy or cardiac applications). A brilliant example of application in RT where the aberration is minimized is Autoscan, the new 4D intrafraction system introduced by Elekta for prostate cancer. The scan is not performed trans-abdominally but trans-perineally, using a mechanically swiped 3D probe. This reduces the distance probe-prostate to less than one third with respect to the traditional technique. Recently, at the 2013 AAPM meeting, work was presented where for

the first time a direct simultaneous comparison between US trans-abdominal and trans-perineal localization of the prostate was performed [2]. Interestingly, after the setup shift performed using the Autoscan system, the residual corrections suggested by the BAT system, scanning transabdominally, are small, less than a mm, in all directions. This would suggest a minimal influence of SOS aberration on transabdominal scans, as opposed to what we have reported. The details of the research are not fully disclosed yet so, for example, it is not clear what contours were compared exactly. With Autoscan a full 3D automated segmentation algorithm can be used, while the BAT system only allows 2D segmentation, which typically produces significantly different results.

Finally, it is worth noting that all these arguments apply to a quantitative use of US. But SOS aberration is also a source of qualitative degradation of the image. E.g. distortion, blurring and lateral defocusing [3] decrease the quality of US scans. It would be very interesting to study in detail how these effects are modulated by the correction proposed in this work. We have mentioned in previous chapters how the contouring process might be affected. But for applications in radiology, where image quality is paramount, its impact could potentially also be significant.

In conclusion, more work needs to be done on this fascinating topic. SOS aberration is a peculiar source of errors. Unlike other aberrations it does not produce recognizable symmetries. Instead, it acts more as a set of lenses which continuously zoom the target in or out depending on the type of tissue traversed by the US beam. The type of problem presented is unique and needs specific solutions. Many researchers faced this challenge in the past but the ultimate correction strategy is still to be developed.

[2] http://amos3.aapm.org/abstracts/pdf/77-22604-310436-91856.pdf

References

1. Sharma A, Wong D, Weidlich G, et al. Noninvasive stereotactic radiosurgery (CyberHeart) for creation of ablation lesions in the atrium. Heart Rhythm 2010;7:802-810.
2. Salter BJ, Wang B, Szegedi MW, et al. Evaluation of alignment error due to a speed artifact in stereotactic ultrasound image guidance. Physics in Medicine and Biology 2008;53:N437-N445.
3. Napolitano D, Chou C-H, McLaughlin G, et al. Sound speed correction in ultrasound imaging. Ultrasonics 2006;44:e43-e46.
4. S. A. Johnson JFG, W. F. Samayoa, F. A. Duck, and J. D. Sjostrand. Reconstruction of three-dimensional velocity fields and other parameters by acoustic ray tracing. Proc. 1975 Ultrasonic Symposium. 197546-51.
5. Kossoff G, Fry EK Jellins J. Average velocity of ultrasound in the human female breast. J Acoust Soc Am 1973;53:1730-1736.
6. Frucht AH. Die Geschwindigkeit des Ultraschalles in menschlichen und tierischen Geweben. Naturwissenschaften 1952;39:491-492.
7. Goss SA, Johnston RL Dunn F. Comprehensive compilation of empirical ultrasonic properties of mammalian tissues. J Acoust Soc Am 1978;64:423-457.
8. Sarvazyan AP, Rudenko OV, Swanson SD, Fowlkes JB Emelianov SY. Shear wave elasticity imaging: a new ultrasonic technology of medical diagnostics. Ultrasound Med Biol 1998;24:1419-1435.
9. Mast TD. Empirical relationships between acoustic parameters in human soft tissues. Acoustics Research Letters Online 2000;1:37-42.
10. Veyrieres JB, Albarel F, Lombard JV, et al. A threshold value in Shear Wave elastography to rule out malignant thyroid nodules: a reality? Eur J Radiol 2012;81:3965-3972.
11. Evans A, Whelehan P, Thomson K, et al. Differentiating benign from malignant solid breast masses: value of shear wave elastography according to lesion stiffness combined with greyscale ultrasound according to BI-RADS classification. Br J Cancer 2012;107:224-229.
12. Van den Heuvel F, Powell T, Seppi E, et al. Independent verification of ultrasound based image-guided radiation treatment, using electronic portal imaging and implanted gold markers. Med Phys 2003;30:2878-2887.
13. Peng C, Kainz K, Lawton C Li XA. A Comparison of daily megavoltage CT and ultrasound image guided radiation therapy for prostate cancer. Medical Physics 2008;35:5619.
14. Scarbrough TJ, Golden NM, Ting JY, et al. Comparison of ultrasound and implanted seed marker prostate localization methods: Implications for image-guided radiotherapy. Int J Radiat Oncol Biol Phys 2006;65:378-387.
15. McGahan JP, Ryu J Fogata M. Ultrasound probe pressure as a source of error in prostate localization for external beam radiotherapy. Int J Radiat Oncol Biol Phys 2004;60:788-793.
16. Langen KM, Pouliot J, Anezinos C, et al. Evaluation of ultrasound-based prostate localization for image-guided radiotherapy. Int J Radiat Oncol Biol Phys 2003;57:635-644.
17. Yaffe MJ, Boone JM, Packard N, et al. The myth of the 50-50 breast. Med Phys 2009;36:5437-5443.

Summary

The aim of radiotherapy (RT) is to deliver a precisely controlled radiation dose to the target, while sparing the normal tissue and possible nearby organs at risk. To improve accuracy in delivery, ultrasound guidance (USgRT) can help patient positioning before each treatment session. Quantitative use of ultrasound (US) has historically been limited by aberrations, among which speed of sound (SOS) aberration is one of the most difficult to correct for. In this work we found a correction strategy which makes use of the coregistered computerized tomography (CT) scan as source for physical density information. This is then transformed into SOS map of the patient and used for the cumulative correction. A general introduction is given in **Chapter 1** on the background and importance of US applications in RT. A more detailed description of US technology is presented in **Chapter 2**. This is part of an invited review for Physics in Medicine and Biology. The aim is to make the reader more familiar with the concepts used in the rest of the thesis and to provide a convenient framing in the field of RT. With **Chapter 3** the idea based on the observation that in RT a CT scan is always available, which can be used as source for physical density, is introduced. The MATLAB algorithm created for the correction is described in detail. Validation on phantoms was performed and a first simplified application on a prostate and a breast cases showed. In **Chapter 4** a systematic study of the SOS aberration correction effect on different clinical scenarios is reported. Five prostate, five breast and five liver cancer cases were examined. On each of them, the correction was applied and the magnitudes of the shifts produced by the algorithm were considered indications of the impact of the aberration. The results show that for liver the aberration is unpredictable for the effects on both structures depth and shape. So, in our dataset, a correction was always necessary, since errors up to more than 7 mm in positions of the regions of interest (ROI) were measured. Also for the prostates, an average error of about 3 mm in the position of the centroids was sufficient to suggest a correction for SOS aberration. The magnitude and direction of these shifts were in good agreement with the discrepancies reported in literature, which made us hypothesize that SOS aberration might be an explanation for a large part of them. For breasts, small shifts were measured, typically around 1 mm. We did not exclude that the limited dataset with possibly small breasts might have biased these results. But from our experience, it does not seem that for these organs a correction is strictly required. In **Chapter 5** the sensitivity of the procedure to workflows and changes in the patients was examined. All the possible combinations of the clinical workflows and changes that can occur in the patient or to the scanning protocol were addressed. We extensively tested the robustness with extreme parameter variations in phantoms, even slightly outside clinical conditions. At the end, it was possible to claim that if no major changes happen, where by major we mean changes that would require re-planning of the treatment, the algorithm produces correct results. In particular, it produces better results than each of the workflows

considered, and always with discrepancies below the clinically detectable threshold. Once the algorithm was validated on phantoms, tested on patients and proven robust, we extended in **Chapter 6** its range of application. From the initial parallelepipedal volumes produced by linear probes, we re-coded it in C++ to a more general case of a generic 3D US volume produced by a curvilinear probe, which includes the previous shape but allows also any volume with non-parallel paired sides. The new algorithm was validated on a pelvic phantom. Then it was applied to 15 prostate cancer patients. The results confirmed the conclusions of Chapter 4, showing the same direction and average magnitude for the SOS aberration. **Chapter 7** is based on the observation that, as reported in literature, CT and US visualize the tissues differently. In particular, to some extent they provide complementary information, because US can image soft tissues with high contrast and resolution, typically on limited spatial volumes. CT instead produces larger images with well-defined bony structures, invisible to US. The segmentation algorithm presented makes for the first time a simultaneous use of the information from both modalities; for the first time it is natively in 3D space, and again for the first time it is completely automatic. It is intelligent, meaning that it can be trained on a specific dataset representing the characteristics of a patients' population. We asked an experienced physician to contour the prostates on the fusion of 16 co-registered CT and US scans. The algorithm was able to reproduce independently the contours to an excellent degree. In **Chapter 8** the results obtained are critically re-viewed in view of possible future developments.

Acknowledgments

I can still remember distinctly the day when my supervisor, Prof. Frank Verhaegen, told me: “Davide, I have a simple exercise to get you started with your work and become a little familiar with ultrasounds: you could find a correction for this well-known imaging error in ultrasound named speed of sound aberration. Then we can start with the serious stuff.” Four years and a PhD thesis later, I am now a bit worried to find what the serious stuff is going to be. This work was only possible because he believed that this Italian guy could make it, despite a certain amount of contrary indications. He never stopped supporting me, at the most incredible hours of day and night, even when it really seemed tough, more as a friend would do rather than a supervisor.

It is difficult to explain on how many levels this work and I personally owe to Dr. Guido Catolla. The first day I spoke to him about my intentions (was it Verona?) I was expecting some frozen or disappointed reactions. As usual he surprised me, he brilliantly found a way to get the best out of it for everyone, and he was the one suggesting we focus our work on ultrasound. Uncountable times he backed me up, I know he is always on my side and this (together with his ex-American football player body build) has always given me the confidence I needed to do my job at best.

I would like to thank my two paranimphs, Skadi and Wouter, for the efforts put in helping me organize this important step in my life. All the coauthors of my papers: Emma, Esther, Gabriela, Silvia, Francesco, Denis, Imad, Sebastian who, in these years, have shared with me the tension of waiting for reviews. All the staff at MAASTRO, the colleagues in the researchers’ room, and the Resonant Medical (now Elekta …) group, who constantly provided me with data, suggestions and valuable expertise.

I want to thank the members of the evaluation committee, Prof. Philippe Lambin, Prof. Jeffrey Bamber, Dr. Walter Backes, Prof. Klaas Nicolay and Prof. Hessel Wijkstra for the time and efforts devoted to reviewing my thesis and for the comments, some of which were enlightening.

Alessia you have put light in my life, you keep me going. You are the only person I have met capable of changing my mood, you make me happy when life is good or when it is bad. Simple as that.

Mom, dad, grandma, grandpa: it is now a long time since I last could share my feelings and my emotions with you. With you words were never necessary, but my silences sound empty now. I hope I can feel again the warmth of that silence in these days.

Loriana, Alessandra and Vittoria: you are the only witnesses, from close or far, I have of my life. You were there. And I know you will be. I want to thank Carlo for showing me the existence of the most delicate deep friendship, I could not believe in such a thing today without him. To Francesco I can only say: zio, do you know who I really consider a brother? (Answer loud in a crowded place, please, and add points to the scoreboard).

Curriculum Vitae

Davide Fontanarosa was born on June 18th 1974 in Como, Italy. He graduated from a Classic Literature High School (Liceo Classico di Saronno), then he started his studies in Physics at the University of Insubria (Como). After a break due to family reasons, he received a Master's degree in Physics at the University of Trieste, with specialization "Nuclear and Subnuclear Astrophysics". He almost immediately changed his field of research into Medical Physics, and joined for two years the PhoNeS (Photo-Neutron Source) research group at the National Institute for Nuclear Physics (INFN) in Trieste. He then worked for Tomotherapy (Madison, WI, USA), with a more technical position as engineer, for one and a half years. He started after this experience a new privately funded research laboratory at the Scientific and Technological Area (PST) in Udine where he worked as manager of Research for more than four years. Meanwhile he was also Application and Physics specialist for the Philips Pinnacle treatment Planning System, and started his PhD project with Prof Verhaegen at Maastro Clinic (Maastricht). In 2011 he was hired by Philips Research as Research Scientist to work on the Airforce joint private-governmental project for the CTMM (Center for Translational Molecular Medicine) collaboration. He is currently still working for Philips Research on multiple projects in collaboration with Maastro Clinic (Maastricht).

Publications

Published articles

D. Fontanarosa, M. Witte, G. Meijer, G. Shakirin, J. Steenhuijsen, D. Schuring, M. van Herk, P. Lambin "Probabilistic evaluation of target dose deterioration in dose painting by numbers for stage II/III lung cancer." Submitted to Radiotherapy and Oncology (2013)

J. Spijkerman, **D. Fontanarosa**, M. Das, W. van Elmpt "Validation of non-rigid registration in pre-treatment and follow-up PET/CT scans for quantification of tumor residue in lung cancer patients ." Submitted to Medical Physics (2013)

D. Ermacora, S. Pesente, F. Pascoli, S. Raducci, R. Mauro, I. Abu Rumeileh, F. Verhaegen, **D. Fontanarosa** "Automated CT-US cross-modality 3D contouring algorithm for prostate." Submitted to Physics in Medicine and Biology (2013)

Fontanarosa D, van der Laan HP, Witte M, Shakirin G, Roelofs E, Langendijk JA, Lambin P, van Herk M. "An in silico comparison between margin-based and probabilistic target-planning approaches in head and neck cancer patients." Radiotherapy and Oncology 2013 Sep 14. doi:pii: S0167-8140(13)00382-4. 10.1016/j.radonc.2013.07.012. [Epub ahead of print]

S. van der Meer, E. Bloemen-van Gurp, J. Hermans, R. Voncken, D. Heuvelmans, C. Gubbels, **D. Fontanarosa**, P. Visser, L. Lutgens, F. van Gils, F. Verhaegen "Critical assessment of intramodality 3D ultrasound imaging for prostate IGRT compared to fiducial markers." Medical Physics 40(7): 071707 (2013).

D. Fontanarosa, S. Pesente, F. Pascoli, D. Ermacora, I.A. Rumeileh, F. Verhaegen "A speed of sound aberration correction algorithm for curvilinear ultrasound transducers in ultrasound-based image-guided radiotherapy." Physics in Medicine and Biology 58(5):1341-60 (2013).

E. Bloemen-van Gurp, S. van der Meer, J. Hendry, J. Buijsen, P. Visser, **D. Fontanarosa**, M. Lachaine, G. Lammering, F. Verhaegen "Active breathing control in combination with ultrasound imaging: a feasibility study of image guidance in stereotactic body radiation therapy of liver lesions." International Journal Radiation Oncology Biology Physics 85(4):1096-102 (2013)

D. Fontanarosa, S. van der Meer, F. Verhaegen "On the significance of density-induced speed of sound variations on US-guided radiotherapy." Medical Physics 39(10):6316-23 (2012).

D. Fontanarosa, S. van der Meer, E. Bloemen-van Gurp, G. Stroian, F. Verhaegen "Magnitude of speed of sound aberration corrections for ultrasound image guided radiotherapy for prostate and other anatomical sites." Medical Physics 39(8):5286-92 (2012).

D. Fontanarosa, S. van der Meer, E. Harris, F. Verhaegen "A CT based correction method for speed of sound aberration for ultrasound based image guided radiotherapy." Medical Physics 38(5):2665-73 (2011).

M.D. Falco, **D. Fontanarosa**, R. Miceli, A. Carosi, R. Santoni, M. D'Andrea "Preliminary studies for a cbct imaging protocol for offline organ motion analysis: registration software validation and ctdi measurements." Medical Dosimetry 36(1): 91-101 (2011)

D. Fontanarosa, L.C. Orlandini, I. Andriani, L. Bernardi "Commissioning Varian enhanced dynamic wedge in the PINNACLE treatment planning system using Gafchromic™ EBT film." Medical Physics 36(10): 4504-4510 (2009)

D. Fontanarosa, A. D'Assie, M. Calderan "Misure di fascio in Tomoterapia con Tomodose in una gestione del reparto di Oncologia Radioterapica via web." Rivista Medica 13(3): 57-61 (2007)

R. Bevilacqua, G. Giannini, F. Calligaris, **D. Fontanarosa** et al. "PhoNeS: a novel approach to BNCT with conventional radiotherapy accelerators." Nuclear Instruments and Methods in Physics Research Section A 572: 231-232 (2007)

R. Bevilacqua, G. Giannini, **D. Fontanarosa**, G. Scian, A. Zanini, O. Borla, A. Piermattei, A. Fidanzio. "Realizzazione di un convertitore fotoneutronico per e-LINAC ospedalieri finalizzato alla radioterapia con cattura di neutroni su boro (BNCT)." Radiazioni Ricerca e Applicazioni 10(1): 10-13 (2007)

M. Vidali, M. Bari, **D. Fontanarosa**, G. Giannini, A. Gregorio, A. Monfardini. "Development of a flexible MAPMT photon-counting read-out system." Nuclear Instruments and Methods in Physics Research Section A 545; 375-382 (2005)

Published abstracts

D. Fontanarosa, S. van der Meer, F. Verhaegen "Speed of sound aberration evaluation and correction in USgRT applications." AAPM 2013 conference, Indianapolis (USA).

D. Fontanarosa, M. Witte, G. Meijer, G. Shakirin, J. Steenhuijsen, D. Schuring, M. van Herk, P. Lambin "Dose painting by numbers for NSCLC: probabilistic evaluation of the

impact of uncertainties on target dose coverage." ESTRO 2013 conference, Geneva (Switzerland).

D. Fontanarosa, S. Pesente, F. Pascoli, D. Ermacora, I. Abu Rumeileh, F. Verhaegen "Speed of sound aberration correction for volumetric prostate imaging in ultrasound based image guided radiotherapy." ESTRO 2013 conference, Geneva (Switzerland).

J.M. Spijkerman, **D. Fontanarosa**, G. Shakirin and W. van Elmpt "Assessment of overlap between high FDG-uptake areas in deformed pre-treatment and post-treatment PET scans." ESTRO 2013 conference, Geneva (Switzerland).

J.M. Spijkerman, **D. Fontanarosa**, G. Shakirin W. van Elmpt "Assessment of accuracy of non-rigid registration algorithms for follow-up treatment NSCLC imaging." ESTRO 2013 conference, Geneva (Switzerland).

D. Ermacora, S. Pesente, F. Pascoli, S. Raducci, R. Mauro, I. Abu Rumeileh, F. Verhaegen, **D. Fontanarosa** "Automated cross-modal 3D contouring algorithm for prostate 3D ultrasound-CT co-registered images." ESTRO 2013 conference, Geneva (Switzerland).

V. Prokic, G. Meijer, D. Schuring, F. Röhner, M. Mix, **D. Fontanarosa**, G. Shakirin, M. Bal, U. Nestle "4D dose painting by numbers for lung cancer." ESTRO 2013 conference, Geneva (Switzerland).

D. Fontanarosa, S. van der Meer , F. Verhaegen "On the significance of density-induced speed of sound variations on US-guided radiotherapy." AAPM 2012 conference, Charlotte (USA).

S. van der Meer, J. Wong, E. Bloemen, **D. Fontanarosa**, M. Lachaine, F. Verhaegen "Towards real-time ultrasound image guided abdominal radiotherapy." AAPM 2012 conference, Charlotte (USA).

D. Fontanarosa, H.P. van der Laan, M. Witte, G. Shakirin, E. Roelofs, J.A. Langendijk, M. van Herk and P. Lambin "Possible advantages of probabilistic planning for head and neck cancer." ESTRO 2012 conference, Barcelona (Spain).

S. van der Meer, E. Bloemen-van Gurp, J. Hermans, R. Voncken, D. Heuvelmans, C. Gubbels, **D. Fontanarosa**, P. Visser, L. Lutgens, F. van Gils, F. Verhaegen "Prostate IGRT using quantitative 3D ultrasound imaging: intramodality US vs. MV imaging of implanted markers." ESTRO 2012 conference, Barcelona (Spain).

F. Verhaegen, S. van der Meer and **D. Fontanarosa "**On the significance of density-induced speed of sound variations on Ultrasound-guided radiotherapy." ESTRO 2012 conference, Barcelona (Spain).

D. Fontanarosa, S. van der Meer, E. Harris, F. Verhaegen "Speed of sound aberration correction in quantitative ultrasound-aided image guided radiotherapy." AAPM 2011 conference, Vancouver (Canada).

D. Fontanarosa, S. van der Meer, F. Verhaegen "Clinical evaluation of a speed of sound aberration correction algorithm in quantitative ultrasound-aided image guided radiotherapy." ESTRO 2011 conference, London (Great Britain).

D. Fontanarosa, F. Verhaegen "Measurements corrections in quantitative ultrasound-aided image guided radiotherapy: speed of sound aberration correction." ESTRO 2010 conference, Barcelona (Spain).

D. Fontanarosa, F. Verhaegen "Speed of sound aberration correction for US-aided patient registrations in quantitative Image Guided Radiotherapy techniques." EPI2kX conference, Leuven (Belgium).